



Design of a low drag universal frame for subsea data acquisition in high energy tidal sites

Final report for the 2016/17 Marine Alliance for Science and Technology for Scotland (MASTS)
Visiting Fellowship

Dr. Giuseppe Calise (MASTS Visiting Fellow)

PostDoc Researcher

Univ. of Naples Federico II - Naples

Naples, Campania 80125 IT

Arne Vögler (MASTS Visiting Fellow Host)

Principal Investigator Marine Energy

Marine Energy Research Department

University of the Islands and Highlands

Lews Castle College

Stornoway – Isle of Lewis, Scotland, HS2 0XR

Prof. Domenico Coiro (Visiting Fellow Contracts Manager)

Seapower Scrl, Univ. of Naples Federico II - Naples

Industrial Engineering Dept. – Aerospace Div.

Naples, Campania 80125 IT

01 February 2018

Table of contents

MASTS Fellowship Timeline (major events)	3
Acknowledgments	3
Project overview	4
CAD modelling of existing frames	4
Early CFD simulations on existing frames	6
Final CFD simulations results on existing frames (Frame_#0, Frame_#1)	13
Optimizing existing frame models	16
Preliminary design of the Frame_#2 specific	20
Optimizing Frame_#2 shape: the Frame_#3	27
Frame_#4: final configuration of the optimized frame	37
Manufacturing process of the Frame_#4	41
First successful deployment of the Frame_#4 in the Pentland Firth environment	59
Final remarks	62
References	64

This report should be cited as:

Calise, G. (2017), *“Design of a low drag universal frame for subsea data acquisition in high energy tidal sites”*, Report to MASTS (LCC Report No. 127) available from:

http://wpage.unina.it/giuseppe.calise/MASTS_LCC_Report_N127.pdf

MASTS Fellowship Timeline (major events)

- 15th August 2016 – Notification of successful MASTS application
- 15th September 2016 – Moving from Italy to Stornoway (Scotland) for starting activities at Lews Castle College UHI
- 19th September 2016 – Activities start date at Lews Castle College UHI
- 25th September 2016 – Preliminary 3D simulations on previously used frames
- 7th -9th November 2016 – Presentation of the ongoing work funded by MASTS at the UHI Research Conference, Inverness (Scotland)
- 15th November 2016 – Parametrical 2D simulations on optimization parameters
- 15th January 2017 – Definition of the optimized frame shape using 2D simulations data
- 31st January 2017 – Technical drawings for manufacturing of the new bottom frame shape
- 10th February 2017 – Manufacturing starting date of the new bottom frame shape
- 1st March 2017 – Final CFD simulations accounting also for sensor gimbal movements and water velocity profile (as boundary condition)
- March 2017 – Manufacturing of frame in Lews Castle College engineering facilities
- August/September 2017 – Successful deployment of the first frame prototype in the Pentland Firth for 4 weeks
- October 2017 – Presentation of results at MASTS ASM Conference in Glasgow

Acknowledgments

I would like to thank Marine Alliance Science and Technology for Scotland (MASTS) as principal funder of this research. I would further like to acknowledge my colleagues and all the staff from the UHI Lews Castle College, who made me feel very welcome for all the project time.

I would also like to show my gratitude to the Hebrides Marine Services Ltd (HMS), in the person of Arne Vögler, for sharing his experience for the purposes of this research, providing insight and expertise that greatly assisted the research.

My acknowledgments are also given to Seapower srl and University of Naples Federico II, in the person of Prof. Domenico Coiro, for supporting this research performing CFD simulations on their HPC facilities.

Finally I would like to acknowledge the UK EPSRC funded FloWTurb project (EP/N021487/1) for providing access to field data from previous ADCP deployments, which have greatly informed the design process. This MASTS funded Fellowship has been delivered in close co-operation with the FloWTurb WP2 'Quantification of turbulence in combined wave and current situations in energetic tidal channels through field data acquisition' with great mutual benefit.

Project overview

This work investigates the performance of different seabed frame shapes by means of Computational Fluid Dynamics (CFD) simulations. Being equipped with data sensors (i.e. ADCPs), they are usually deployed to measure currents and wave heights during the time of deployment. The aim of such research is to design an optimized bottom frame for easy deployment in high energy tidal sites. Indeed, as data acquisition in such development areas is often very challenging in terms of both success and data reliability, it is a matter of importance to design an improved sensor frame shape to improve the success and data quality of measurements.

Starting from a very standard bottom frame shape usually sold by NORTEK or others for sensor deployment purposes, the performance of this shape in terms of generated drag force, lift force and eddies over and around the sensor head have been investigated. Using extensive three-dimensional CFD simulations, several modifications of such standard frame has been compared. Those frames have been tested using steady high-speed flow condition. Then, CFD results have been used to set-up a ballast evaluation process which takes into account forces on the frame and different seabed friction coefficient: in this way, it has been possible to assess the deployment effort related to each bottom frame shape under test.

Using a parametrical CAD design and two-dimensional simulations, an optimization process has been carried out on several frame parameters: in this way, it has been possible to monitor how the lift-to-drag ratio (later called efficiency) is affected by each parameter modification and to obtain a final optimised shape. Even if the optimized shape has resulted interesting in terms of lift-to-drag ratio, some concerns arose about the manufacturability of such frame and, finally, a more conventional design has been chosen.

The final frame design is a square based shape, with a reduced height and a fixed side inclination. All the frame sides are closed, to protect the sensor from flow and seabed debris, whereas the sensor is installed inside a gimbal to be always oriented in the correct direction. The increased total weight of such frame and the improved aerodynamic performance allow an easier sensor deployment, as a very low amount of ballast is needed. To improve the measured data quality and increase the separation area over the sensor head, to push away eddies from the sensor head and, in turn, decrease sensor tilting, some vortex generators have been tested with some beneficial effects on lift-to-drag ratio as well.

CAD modelling of existing frames

The first task has been to model the existing frame in Figure 1 usually used for this purpose. Such frame is a standard commercial frame, in this case supplied by NORTEK AS, for Acoustic Doppler Current Profiler (ADCP) sensor deployment. The main objective was to obtain a sufficiently detailed shape to use in the CFD simulations. The CAD modelled frame is presented in Figure 2: as it can be seen from that picture, only the main frame features have been modelled, whereas other smaller components have been not considered in order to limit the required computational effort.



Figure 1 - Initial existing frame, later called Frame_#0

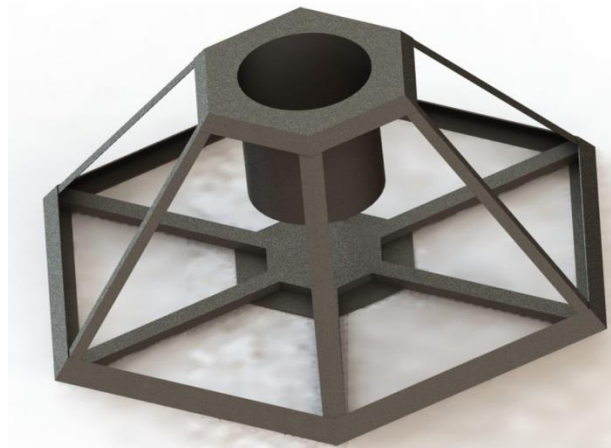


Figure 2 - Frame_#0 CAD model rendering

Some of the main Frame_#0 dimensions and its total weight are reported in Table 1. An important feature of such frame is that its legs are inclined of about 48°, evaluated considering the total frame height of about 0.8 m and its base diameter of about 2.0 m. As will be shown later, the frame legs inclination angle represents a key parameter for shape optimization.

Starting from the Frame_#0 design, another configuration with external closing plates (the Frame_#1 in Figure 4) has been modelled as well. Comparing the Frame_#0 and Frame_#1 performance, in terms of lift and drag forces, it's possible to evaluate their different behaviour in the same flow conditions. Similarly to the Frame_#0, the Frame_#1 data have been reported in

Table 2. By the way, both frame configurations have been already used for sensor deployment.

Table 1 - Frame_#0 main dimensions and data

Frame_#0: components	Weight [kg]	Max thickness [m]	Max width [m]	Max height [m]
Top Cap	21.30	0.003	0.797	0.433
Legs (x6)	8.00	0.003	0.075	0.697
Bottom Cap	88.90	0.003	2.010	0.064
Total Weight:	118.20			

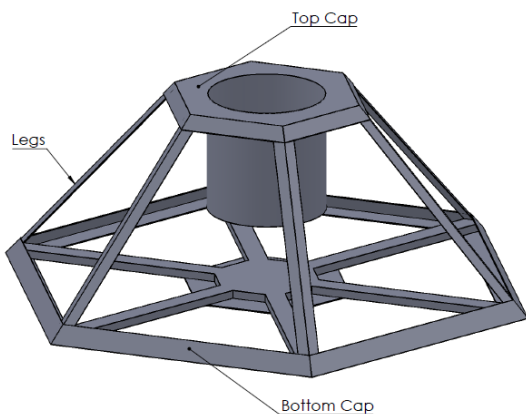


Figure 3 - Frame_#0 components identification



Figure 4 - Frame_#1 CAD model rendering

Table 2 - Frame_#1 main dimensions and data

Frame_#1: components	Weight [kg]	Max thickness [m]	Max width [m]	Max height [m]
Top Cap	21.30	0.003	0.797	0.433
Legs (x6)	8.00	0.003	0.075	0.697
Bottom Cap	88.90	0.003	2.010	0.064
Closing Plates	110.90	0.003	0.948	0.783
Total Weight:	188.00			

The Figure 5 shows a schematic representation of the flow structures expected over the two different frames shapes. As known, when a body is immersed in a flow, due to the pressure distribution over its surfaces, it experiences a force named aerodynamic force (F), whose components perpendicular and parallel to the velocity direction are the lift (L) and drag (D) forces respectively. Indeed, the lift force (L) is defined as the aerodynamic force component perpendicular to the undisturbed flow direction, whereas the drag force (D) is the aerodynamic force component aligned with the asymptotic flow direction. An idea of such forces can be obtained from Figure 5 – (a). A commonly used practice for aerospace application is to refer to such forces in terms of non-dimensional coefficients, generally named force coefficients, through which is possible to compare different aerodynamic shapes independently from the flow field in which they have been tested. This practice has been followed for the scope of this work, using the definitions reported in (1).

$$C_F = \frac{F}{\frac{1}{2}\rho V^2 S} \quad C_L = \frac{L}{\frac{1}{2}\rho V^2 S} \quad C_D = \frac{D}{\frac{1}{2}\rho V^2 S} \quad (1)$$

From Figure 5 is also clear one of the reasons for using the frame closing plates (Figure 5 – (a)): the idea is to protect the sensor from eddies generated inside the frame core, similarly to what the bucket walls do protecting the gimbal and the sensor as well.

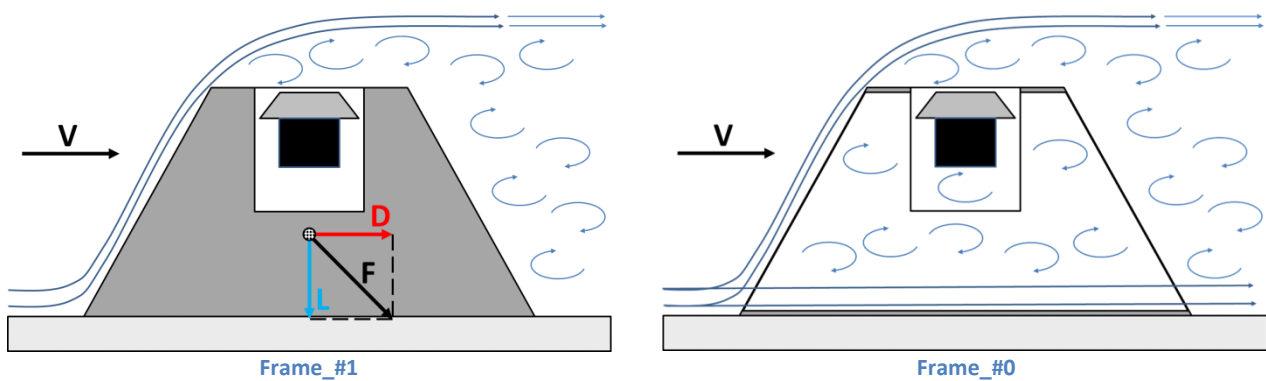


Figure 5 - Schematic flow comparison over different frame shapes

Early CFD simulations on existing frames

The CFD simulations have been performed using the CD-adapco's STAR-CCM+ 9.06.009 software environment lunched on the HPC cluster SCoPe datacentre at the University of Naples Federico II. The pre-process and post-process phases have been completed using a remote access to a computing device located into the Industrial Engineering Dept. – Aerospace Div. buildings at the University of Naples Federico II. Most of the simulations here reported have needed at least one day of computational time using 32 CPUs; in a very limited number of cases, it has been necessary to use up to 128 CPUs for more than 7 days. The computing device for pre/post-process is a Windows 7 machine.

Preliminary CFD simulations have been performed with the aim of evaluating Frame_#0 and Frame_#1 performance in different flow conditions. Naming θ the asymptotic flow direction and considering the frame shape symmetry property as well, three flow angles have been investigated: $\theta = 0^\circ$ (black arrow), meaning that the flow is impinging one of the frame edges; $\theta = 15^\circ$ (blue arrow) and $\theta = 30^\circ$ (purple arrow), when the flow is perpendicular to the frame closing plate (see Figure 6).

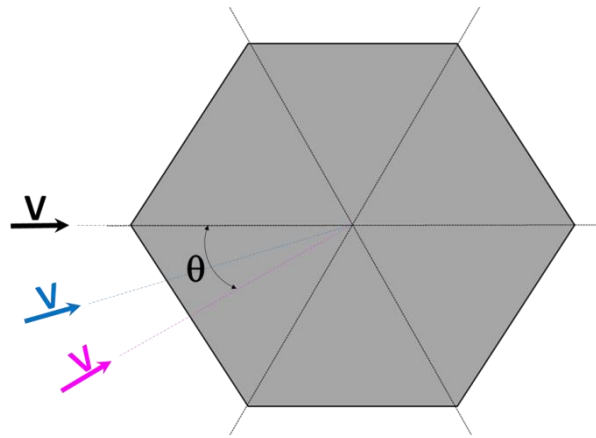


Figure 6 - Flow conditions under test for Frame_#0 and Frame_#1

To create a proper computational domain and set up the grid and the simulation physics, some of the guidelines in [1] for external aerodynamic simulations have been followed (see Figure 7), along with practical examples from reference [2]; some of the used data for such preliminary simulations are in Table 3. Due to the symmetrical properties of both flow conditions and frame shapes, it has been possible to simulate only a half of the three-dimensional computational domain, with a considerable reduction of the required computational time.

The blue surface in Figure 8 represents the domain symmetry plane, while the orange one is the domain outlet; the grey surfaces of the frame and the domain bottom have been modelled as non-slip walls, to allow the boundary layer development on them. All the other surfaces not visible in Figure 8 are the domain inlet where a velocity inlet boundary condition has been used.

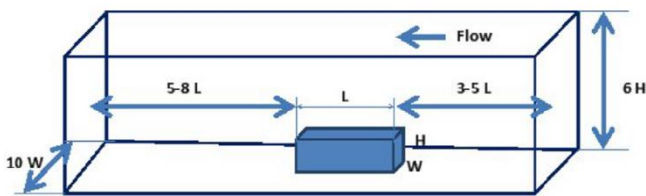


Figure 7 - STAR-CCM+ domain guidelines for CFD domain sizing

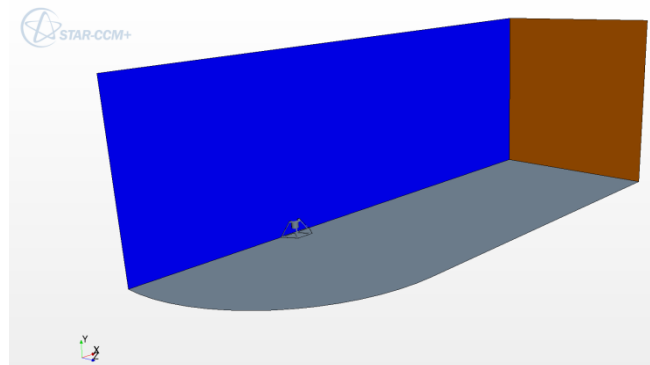


Figure 8 - Computational domain layout

Table 3 - CFD simulations reference data

Domain reference values			Meshing models	
Domain length	30	m	Surface Remesher	✓
Domain width	10	m	Trimmed Cell Mesher	✓
Ref. dimension (frame)	1.5	m	Prism Layer Mesher	✓
Other reference values				
Ref. Velocity	3.6	m/s		
Water density	997.56	kg/m ³		
Water (dyn) viscosity	8.89E-04	Pa-s		
Water depth	50	m		
Reynolds Num.	6.06E+06			
First prism layer distance	0.00031	m	Designed wall-y ⁺ value:	wall-y ⁺ ≈30
Turbulence Model	K-Omega Turbulence – SST (Menter) K-Omega			
Solution Approach	Segregated Flow Solver			
Stopping criteria	Residual reduction (under a defined Threshold)			
	Forces/Engineering quantities invariability			

With the data in Table 3, the computational domain mesh in Figure 9 has been obtained: this mesh includes some refinements to resolve areas with strong gradients and, due to the targeted y^+ value ($y^+=30$), it counts about 3M of cell. To improve grid resolution, an adaptive mesh refinement algorithm has been implemented into the CFD software. This algorithm works using the solved pressure value in each cell: it marks the cells in which a threshold pressure value is exceeded (see Figure 10) and, then, their cell size is reduced accordingly. In this way, a final mesh of about 8M/10M (the total cell count depends on the flow condition analysed, the frame shape under test and the solution accuracy). The final mesh screenshots for the Frame_#0 and the Frame_#1 are in Figure 11 and Figure 12. Furthermore, for validating the chosen setup in Table 3, a sensitivity analysis respect to different BCs, mesh resolutions and turbulence models, has been carried out with no significant differences. Thus, these results aren't present here.

Being not evident from Figure 8, it's important to notify that the seabed surfaces inside the frame structure have been modelled using the same wall boundary condition for the seabed, as no flow is expected there when the frame is deployed on a perfectly smooth seabed (i.e., on sandy/clay seabed).

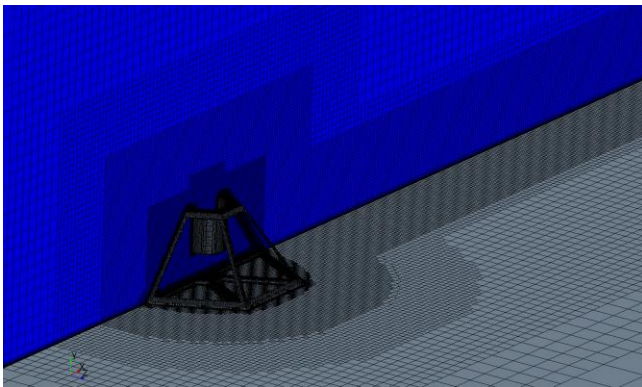


Figure 9 - Mesh (coarse) details along with some refinements

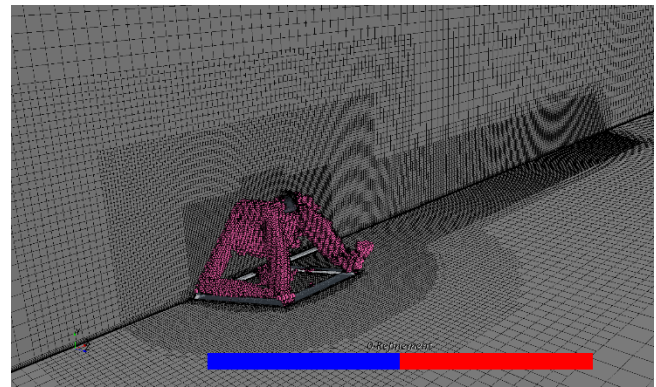


Figure 10 - Pressure based adaptive mesh refinement around the Frame_#0

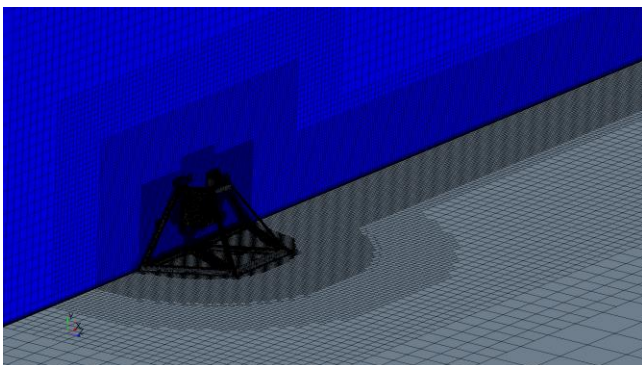


Figure 11 - Mesh (fine) around the Frame_#0

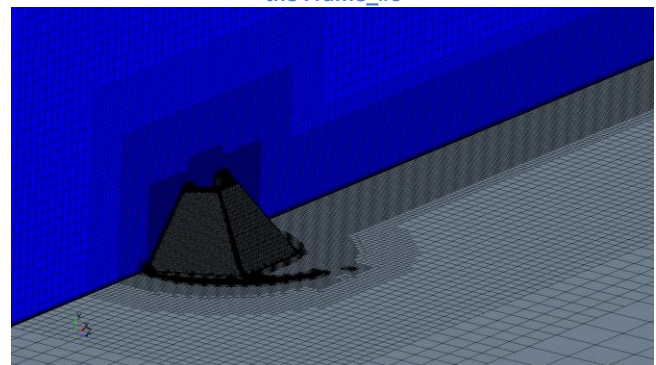


Figure 12 - Mesh (fine) around the Frame_#1

The lift and drag data obtained from the steady flow simulations, considering different flow directions, are reported in Figure 13. As expected, that figure shows how the frame forces change accordingly to the water flow direction. A remarkable result is that the Frame_#1 produces a reasonable amount of downforce, whilst the Frame_#0 produces an upward lift force. These vertical forces are of key importance as they influence the ability of the frame to remain on the sea bottom: in principle, if the frame produces an upward lift force, it requires more ballast to avoid any movement from the seabed; conversely, a frame generating downforce requires less ballast.

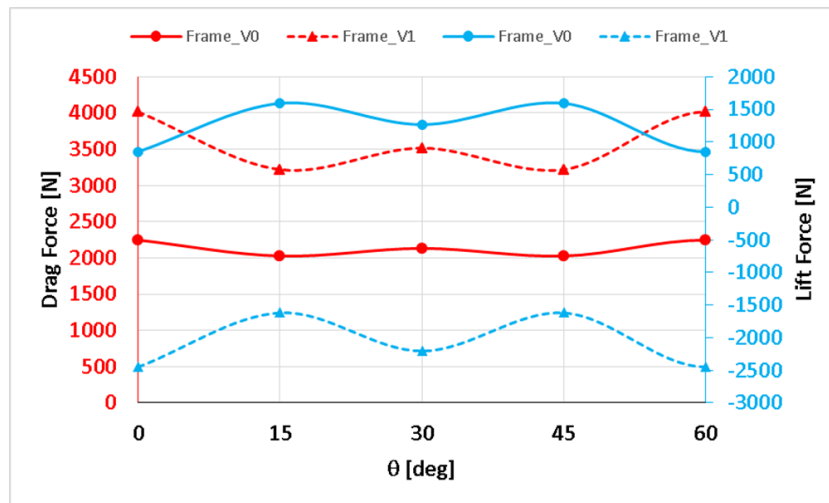
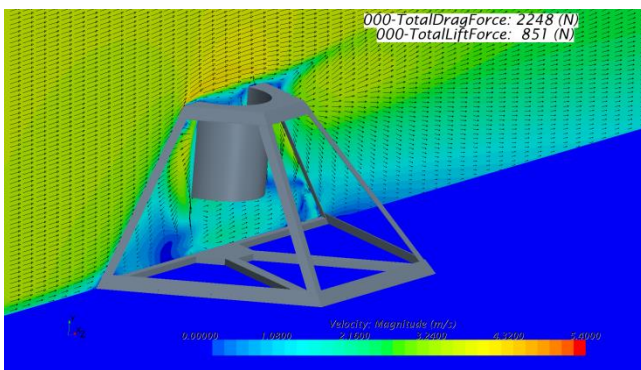
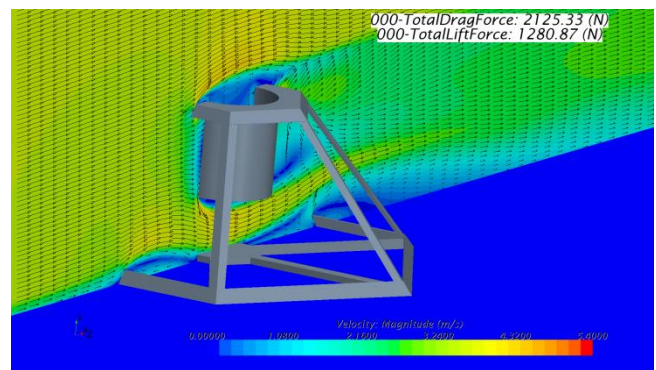


Figure 13 - Lift and drag force data comparison

The Figure 14 and Figure 15 depict the flow field in the sensor frame symmetry plane. It clearly shows how the velocity flow field around the sensor frame is affected by the flow direction. Major evidence of flow field variations on that plane can be observed from Figure 15, looking at the front vortex before the sensor frame and at the wake shapes as well. Nevertheless, it's also evident from Figure 14 the shielding effects of the frame legs and how these effects are reliant on flow direction. Obviously, each of those flow field variations has a strong impact on the forces experienced by the frame.

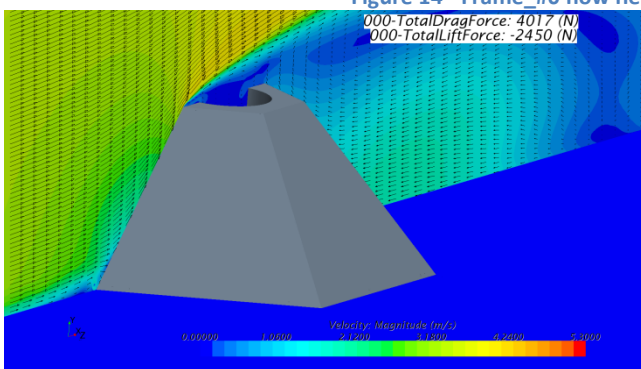


θ = 0°

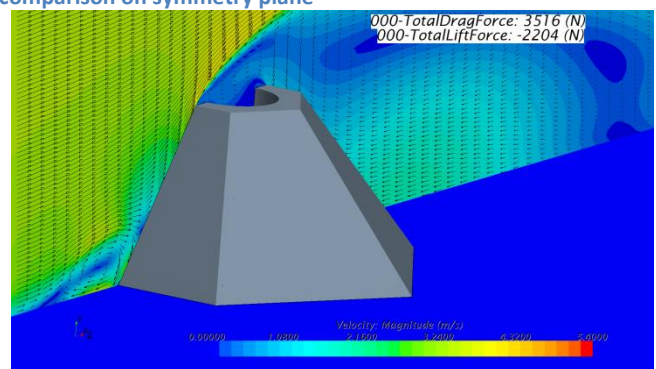


θ = 30°

Figure 14 - Frame_#0 flow field comparison on symmetry plane



θ = 0°



θ = 30°

Figure 15 - Frame_#1 flow field comparison on symmetry plane

Another remarkable result is shown in Figure 16: it displays one of the Frame_#0 well-known issue. Indeed, it has been experienced that, in particular flow conditions, the sensor inside the Frame_#0 bucket is affected by the frame generated eddies. They are highly dependent on the flow velocity direction, causing unwanted and unexpected sensor tilting with the result of poor quality or loss of data. Hence, one of the objective of the new frame shape must be to improve sensor protection, reducing eddies sensitivity as well.

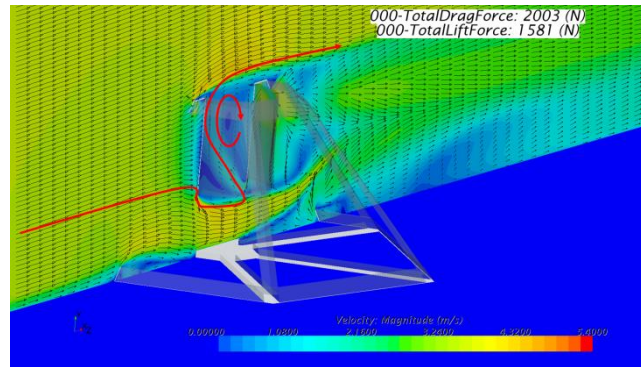


Figure 16 - Frame_#0 flow field inside the sensor installation bucket – $\theta = 15^\circ$

This flow field analogy with the previous deployment experiences has been used as a first validation for the Frame_#0 case. A different data validation process has been done for the Frame_#1 using the reference [3]. The idea has been to compare the Frame_#1 with the performance of an inclined flat plate, shown in Figure 17: using those formulas, is ideally possible to compare the C_L and the C_D of a flat plate with the Frame_#1.

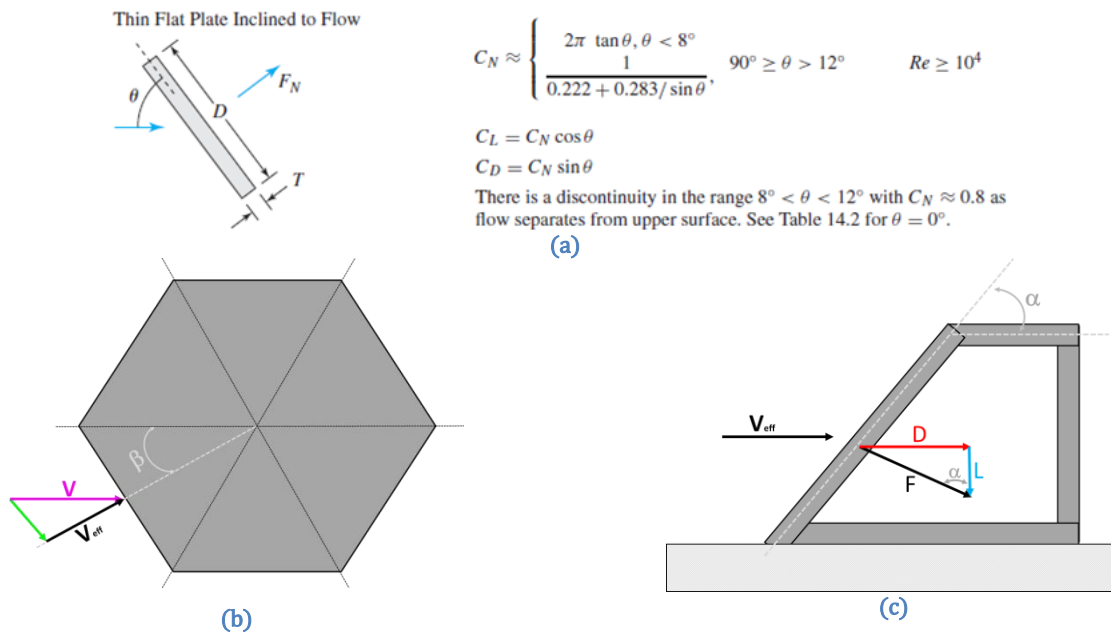


Figure 17 – Flat plate comparison laws with Frame_#1 outer surfaces

Using the notations in Figure 17, the data in Table 4 and the classical lift and drag equations in (4), it has been evaluated the lift and drag values of a flat plate comparable with the Frame_#1 external closing plates. The flat plate drag value in (4) is relative to the CFD semi-model while the ones showed in Figure 14, Figure 15 and Figure 16 are referred to the whole frame. Hence, to evaluate the error between CFD and this simplified theory, it is necessary to double the drag value in (4) for considering two plates exposed to the asymptotic flow. From equation (5), it seems that the lift values are within the 10% error range, whereas the drag ones are overestimated. Such overestimation it's due to different assumptions between the used theory from [3], relative to a two-dimensional infinite flat plate, and the values used for the Frame_#1, relative to a finite three-dimensional geometry. In other words, because the infinite flat plate theory is two-dimensional, it doesn't take into consideration other drag mechanisms peculiar of bluff bodies and its strongly three-dimensional flow. Anyway, such theory it's mostly used to validate lift values than drag ones and, in the light of this, being below the 10% error threshold is a good figure for the acceptance of CFD results.

Table 4 - Frame_#1 reference data

Frame_#1 reference values
$\alpha = 50^\circ$
$\theta = 180^\circ - \alpha = 130^\circ$
$\beta = 30^\circ$
$\rho = 997.56 \text{ kg/m}^3$
$S = 0.435 \text{ m}^2$ (CFD semi - model)
$V_{eff} = V \cos \beta = 3.12 \text{ m/s}$

$$C_N = 1.607 \quad (2)$$

$$C_D = 1.137 \quad C_L = -1.137 N \quad (3)$$

$$D = 1/2 \rho V_{eff}^2 S C_D = 2732 N \quad L = 1/2 \rho V_{eff}^2 S C_L = -2292 N \quad (4)$$

$$\Delta D = \frac{5465 - 4017}{5465} = +26.5 \% \quad \Delta L = \frac{-2292 - (-2450)}{-2292} = -6.9 \% \quad (5)$$

The equation (4) gives more information about the possible design parameter to consider. The aerodynamic forces are linearly dependent on frontal area and drag coefficient, while they are quadratic dependent on flow velocity. Among them, only the frontal area and the drag coefficient can be considered design parameters, as the flow conditions are independent by the design. By the way, changing the frame dimension (i.e., the frame height) can also affect the flow conditions in which the frame will be deployed and, in turn, the total amount of aerodynamic forces.

For completing these preliminary investigations, some unsteady runs have been performed as well. The idea has been to understand how the frame wake characteristics are affected by the frame shape. For setting up the total simulation time for these unsteady simulations, the time needed by the wake to reach the outlet computational domain boundary has been considered. Thus, an overall time of 9.0 s has been simulated, being the domain 30 m long and the flow velocity at 3.6 m/s. Concerning the time discretization, the time step has been chosen taking into account the estimated shedding frequency ($f = \frac{St \cdot V}{d}$), based on the frame geometrical parameters, and also a rule of thumb from [1]: between those values, the minimum one has been used as the simulation time step (see (6)). For evaluating the T_2 timestep, the value of the Strouhal number (St) has been deduced from Figure 18.

$$T_1 = \frac{L_{body}}{20 * V} = \frac{1.5 \text{ m}}{20 * 3.6 \text{ m/s}} = 0.021 \text{ s} \quad T_2 = \frac{1}{2 * f} = \frac{1 * d_{body}}{2 * St * V} = \frac{1 \text{ m}}{2 * 0.42 * 3.6 \text{ m/s}} = 0.331 \text{ s} \quad (6)$$

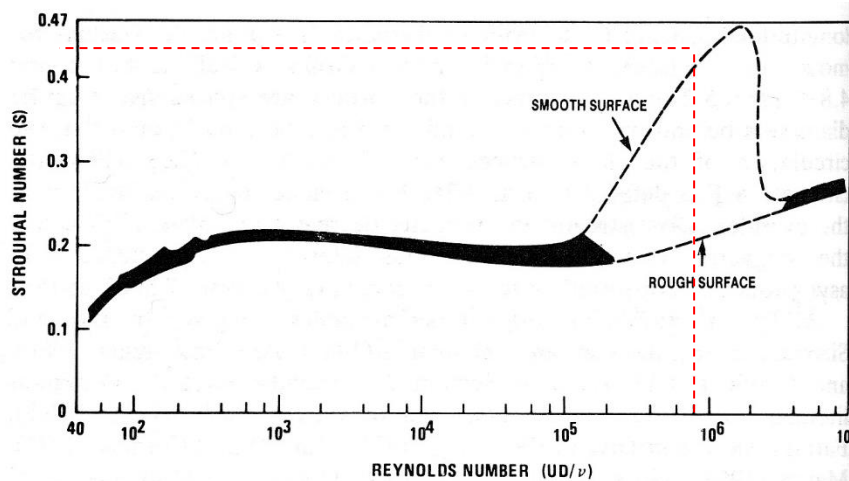


Figure 18 - Strouhal number values from [4]

The unsteady simulation results are presented in Figure 19. Those aerodynamic forces data are referred to the simulated half frame and, thus, they have to be doubled for considering the whole frame shape. The Figure 19 shows that the Frame_#1 is less affected by forces oscillations (vortex shedding), in both the tested flow conditions, even though the amount of downforce and drag force generated are higher. Conversely, the Frame_#0 produces more unsteady forces due to the eddies that continuously detach from the frame legs and the sensor bucket. Hence, the force data require more time to converge on a stable periodic history. Also, it's remarkable that there is a little difference between the unsteady and the steady results, allowing for using the steady approach for the shape optimization process.

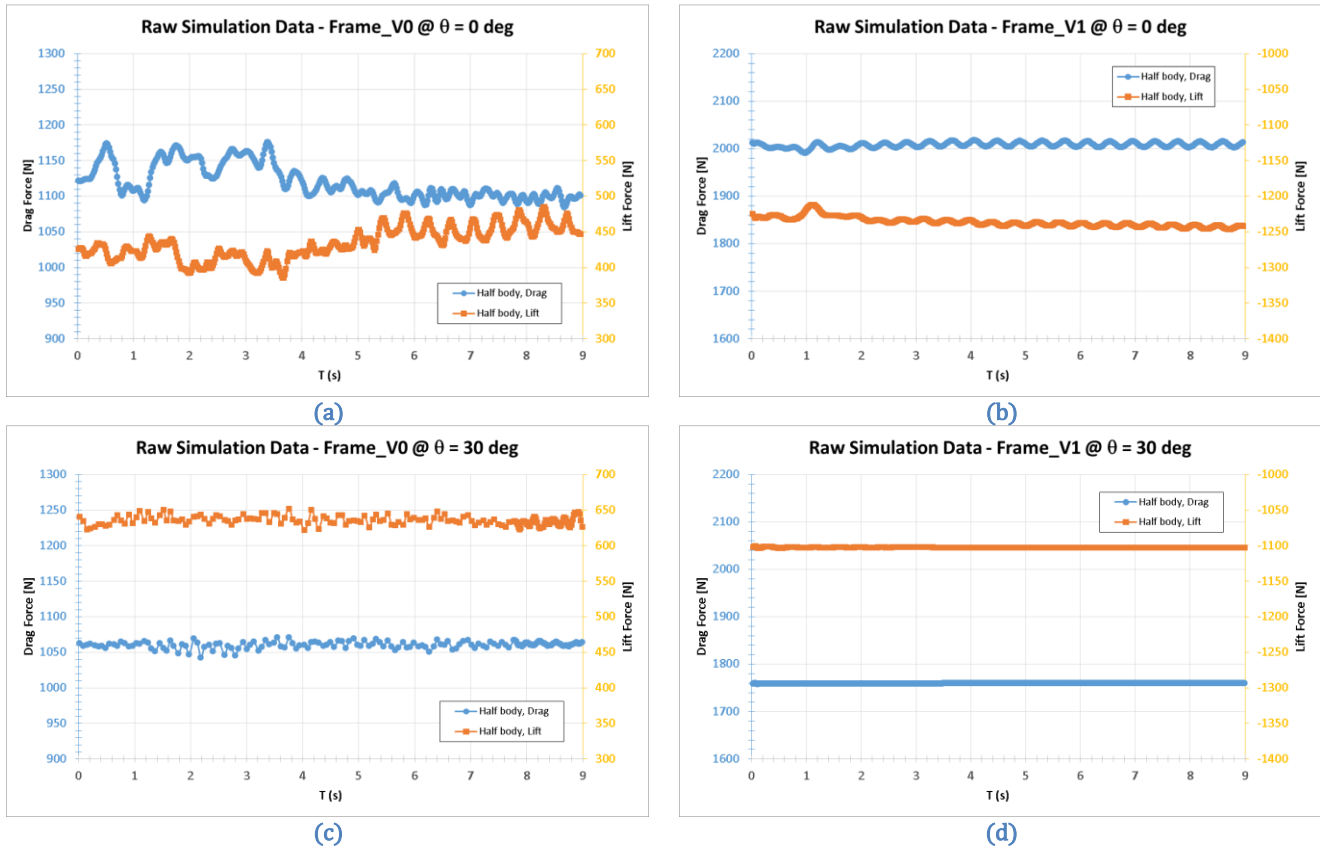


Figure 19 – Unsteady simulations results comparison

After assessing the proper aerodynamic force data for both the investigated frame shapes, it's important to understand how such figures affect the deployment effort, for driving the design process towards some configurations easier to deploy. To do so, it is necessary to evaluate the amount of ballast to keep the frame steadily on the seabed.

Schematically, the forces acting on a generic frame are represented in Figure 20. For evaluating the minimum amount of needed ballast, equilibrium between frame drag (D) and frame-seabed friction forces (F) has to be imposed. Being the friction force proportional to the normal force N generated by the frame, through the seabed friction coefficient μ , the equilibrium equation is the following: $F = \mu N = \mu(W + B - L)$, where W is the frame weight, B is the ballast and L is the frame generated lift/downforce. Thus, the minimum amount of ballast is given by:

$$D \leq F = \mu(W + B - L) \Rightarrow B \leq \frac{D}{\mu} - W + L \quad (7)$$

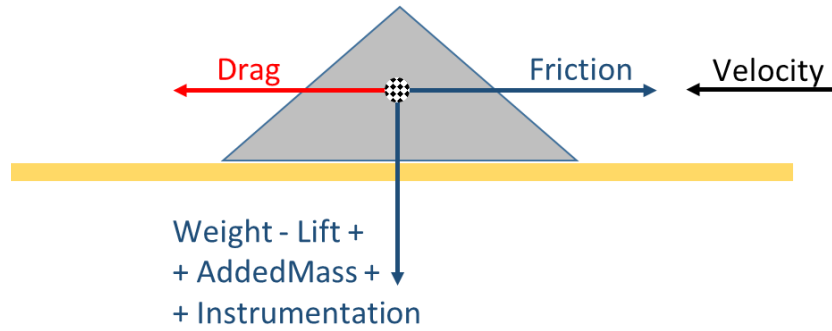


Figure 20 – Schematic representation of the forces on the frame for ballast evaluation

Even though the formula in (7) is easy to use, to obtain a correct ballast evaluation it is necessary to choose the correct value of the friction coefficient μ . Such evaluation is not trivial as its value is highly dependent on the nature of the seabed. For this purpose, several references (see [5], [6], [7], [8], [9], [10]) have been checked. An example of these friction coefficients data is shown in Table 5.

The amount of required ballast depends on both frame aerodynamic performance and geometric data: for ballast evaluation, these values are listed in Table 6. In Table 7 is finally showed the minimum evaluated amount of ballast using a friction coefficient $\mu = 0.74$. The interesting outcome from Table 7 is that the Frame_#1, producing more downforce, don't require any ballast, using this seabed friction coefficient; conversely, the Frame_#0 requires up to 200 kg, in the same seabed conditions.

This figure has been considered for the purpose of designing the new frame shape.

Table 5 – Seabed friction coefficients extracted from [10]

Mooring Line	Ocean Bottom	Friction Factors, μ	
		Starting	Sliding
Chain	Sand ^a	0.98	0.74
	Mud With Sand ^a	0.92	0.69
	Mud/Clay	0.90	0.56
Wire Rope	Sand ^a	0.98	0.25
	Mud With Sand ^a	0.69	0.23
	Mud/Clay	0.45	0.18

Table 6 – Frame reference data used for ballast evaluation

	CAD Estimated Weight [kg]	CAD Estimated Weight [N]	Instrumentation Weight [kg]	Instrumentation Weight [N]	$\theta = 0^\circ$		$\theta = 30^\circ$	
					D [N]	L [N]	D [N]	L [N]
Frame_#0	192,0	1884	30	294,3	2248	851	2133	1268
Frame_#1	301,6	2959			4017	-2450	3517	-2205

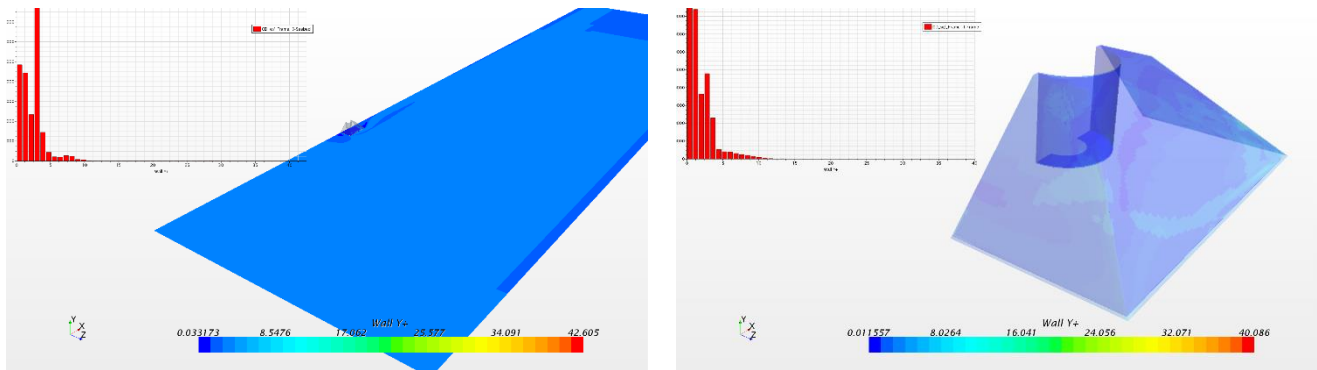
Table 7 – Required ballast for both Frame_#0 and Frame_#1

Friction coefficient $\mu = 0.740$	Ballast [N]	Ballast [kg]	θ [°]
Frame_#0	1711	174	0
	1973	201	30
Frame_#1	-275	-28	0
	-705	-72	30

Final CFD simulations results on existing frames (Frame_#0, Frame_#1)

After the bespoke preliminary simulations, needed to validate the simulation setup, a second set of runs have been performed. The simulations setup has been slightly improved using more convergence criteria and a modified mesh setup, resulting in a lower value of the wall- y^+ field function throughout the computational domain. It is worth to say that the wall- y^+ field function represents an important field to

monitor for CFD simulation accuracy: their values have to be tuned up accordingly to the chosen turbulence model and the needs of resolving the velocity boundary layers around the bodies. This field function is active only on wall boundaries, like the frame itself and the seabed. To reduce wall- y^+ values, it's necessary to increase the cell count, refining the mesh where large gradients are expected. In Figure 21 it is shown the wall- y^+ distribution from one of the simulation performed, for both the seabed surface and the frame one.



(a) (b)
Figure 21 – Wall- y^+ distribution over the seabed (a) and the frame (b) surfaces

Moreover, the Figure 21 shows the cell distribution plot on those surfaces, highlighting that most cells are below the acceptance threshold of wall- $y^+=5$ for resolving the near wall boundary layer. Indeed, the Figure 22 describes the possible different approach for determining the near-wall velocity field: an approach, named law of the wall, is used when wall- $y^+>30$, while the laminar sublayer one is followed when wall- $y^+<5$. While the former approach models the boundary layers following the so-called law of the wall (a log law equation between U^+ and wall- y^+ , the latter resolves directly the boundary layer equations, requiring an increased computational effort. In any case, the blending region has to be avoided as none of these two model is able to correctly describe the boundary layer development when $5 < \text{wall-}y^+ < 30$.

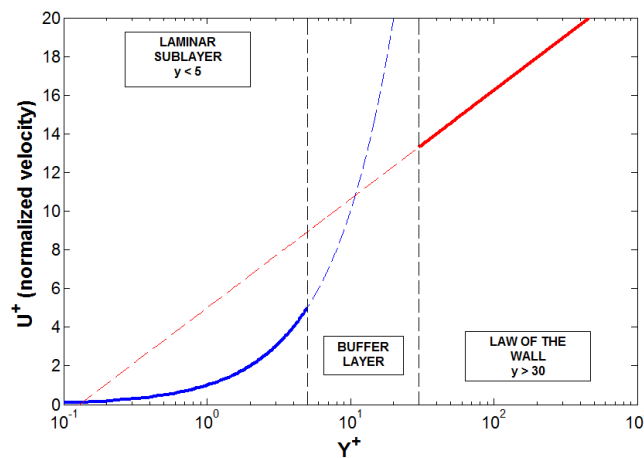
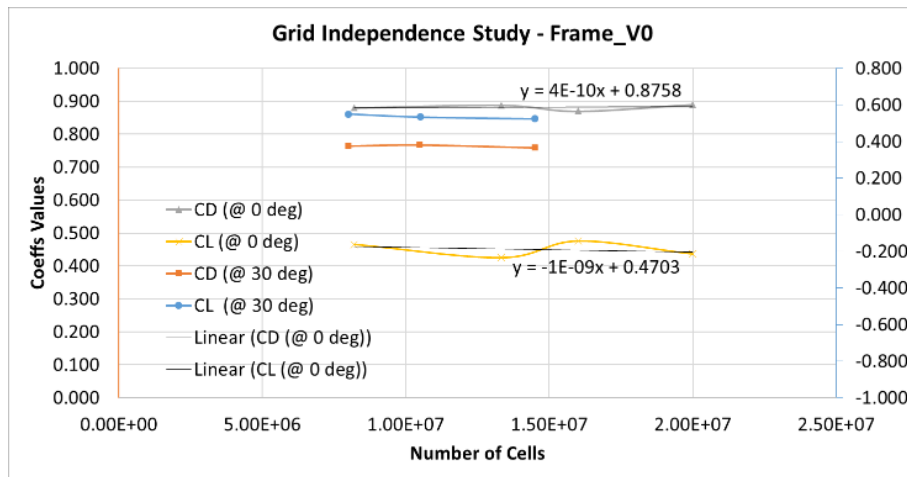


Figure 22 – Wall- y^+ range of validity of different approaches [11]

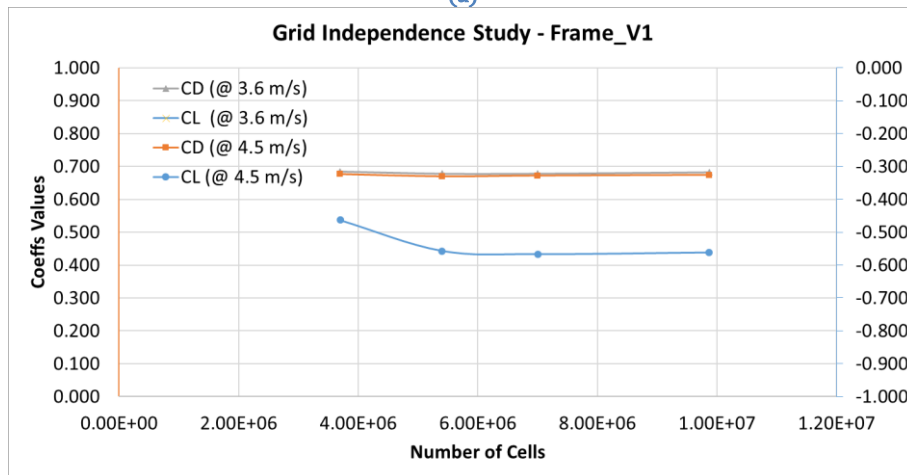
As explained before, there are many difficulties for a proper numerical-experimental validation. Hence, the obtained results have been amended using the well-established practice for CFD simulations of comparing results on several refined grids. Actually, it is known that scaling the mesh continuously, from coarser to finer mesh, allows to minimize the grid dependant errors, even though other error sources cannot be discovered and solved using this approach. Comparing non-dimensional coefficients on different meshes permits to judge if the simulation result is converged, within a certain error threshold, to the real one (in theory, the numerical approximation vanishes when the grid is infinitively refined); furthermore, it is also possible to estimate the percentage of error between one grid to another.

The used CFD software permits to perform such independence analysis, allowing scaling of the mesh based on the so-called base size parameter: four base size values have been investigated from 2.0 m to 1.0 m. For the purposes of the following grid independence analyses, only proper symmetric flow conditions have been simulated that are $\theta = 0^\circ$ and $\theta = 30^\circ$.

In Figure 23 are shown some data related to Frame_#0 and Frame_#1: from Figure 23 – (a) is also evident that non-dimensional coefficients converge more rapidly to a steady value for the $\theta = 0^\circ$ than in the $\theta = 30^\circ$ case, when some data oscillation can be observed. Despite this, the trend lines are all aligned around a common value, for both the C_D and the C_L . The Figure 23 – (b) shows the data associated with the Frame_#1 for two different velocities, without any appreciable difference. As expected, being the Frame_#1 flow field well established and less prone to vortex shedding, aerodynamic values convergence is easier on coarser mesh for the Frame_#1 than the Frame_#0. The Table 8 and Table 9 summarize the aerodynamic data and indicate also the coefficients percentage deviations among different grid sets. All of the following reported data are based on a steady velocity of 3.6 m/s, uniformly distributed at the inlet boundary.



(a)



(b)

Figure 23 – Mesh independence study for Frame_#0 and Frame_#1 cases

Table 8 – Frame_#0 mesh independence study data

BaseSize [m]	CellsNumber	C_D (@0°)	ΔC_D	C_L (@0°)	ΔC_L	BaseSize [m]	CellsNumber	C_D (@30°)	ΔC_D	C_L (@30°)	ΔC_L
2.00	8.20E+06	0.880	1.12%	0.465	-6.41%	1.50	8.00E+06	0.764	-0.66%	0.550	-4.76%
1.50	1.33E+07	0.888	0.22%	0.426	2.52%	1.25	1.05E+07	0.767	-1.05%	0.534	-1.71%
1.25	1.60E+07	0.870	2.25%	0.475	-8.70%	1.00	1.45E+07	0.759		0.525	
1.00	2.00E+07	0.890		0.437							
Interpolated data:		0.8758		0.4703							

Table 9 – Frame_#1 mesh independence study data

BaseSize [m]	CellsNumber	C_D (@3.6 m/s)	ΔC_D	C_L (@3.6 m/s)	ΔC_L	C_D (@4.5 m/s)	ΔC_D	C_L (@4.5 m/s)	ΔC_L
2.00	3.70E+06	0.684	-0.29%	-0.460	17.12%	0.676	-0.30%	-0.463	17.62%
1.50	5.40E+06	0.678	0.59%	-0.547	1.44%	0.670	0.59%	-0.557	0.89%
1.25	7.00E+06	0.678	0.59%	-0.573	-3.24%	0.672	0.30%	-0.567	-0.89%
1.00	9.87E+06	0.682		-0.555		0.674		-0.562	

Using those updated data for the Frame_#0 and the Frame_#1, a new ballast evaluation has been performed. Moreover, the seabed friction coefficient has been reduced for considering a more challenging seabed, made up of sandstone: using a frictional coefficient $\mu=0.340$, the required ballast for deployment is reported in Table 10. In this seabed conditions, it seems that, even if the Frame_#1 produces a large amount of downforce, its increased frontal area produces more drag that doesn't help to keep the frame on the seabed; thus, a larger amount of ballast is needed in both flow condition.

Table 10 – Ballast evaluation for Frame_#0 and Frame_#1 based on a Sandstone seabed

Friction = $\mu \cdot (\text{Weight} - \text{Lift} + \text{AddedMass}) [\text{N}] > \text{Drag}$							
Friction coefficient (Sandstone) $\mu = 0.340$	Drag [N]	Lift [N]	Frontal Area [m ²]	AddedMass [N]	AddedMass [kg]	Flow angle [°]	Total Weight [kg]
Frame_#0	2061	1107	0.182	5712	582	0	731
	2061	1425	0.210	6030	615	30	763
Frame_#1	3833	-3119	0.435	6015	613	0	831
	4382	-3341	0.497	7409	755	30	973

Optimizing existing frame models

In this section, an optimization process performed from the previously analysed sensor frames is presented. Starting from them, it has been evaluated how to improve their performance, improving the recognized beneficial effects of Frame_#1 than Frame_#0.

To reduce computational time, faster and less computational demanding two-dimensional simulations have been used. The purpose of such simplified two-dimensional simulations is to evaluate how some modifications on the frame external shape can increase the lift (L) to drag (D) ratio. In the aeronautical field, this lift-to-drag ratio is commonly defined as aerodynamic efficiency (E). So, the optimisation objective is to find the frame shape external layout able to maximize the absolute value of frame aerodynamic efficiency, in this case related to the lift direction downward to the seabed (the optimization aim is to maximize the downforce-to-drag ratio).

In Figure 24, it can be seen the computational domain used for those two-dimensional simulations, along with the indication of the used boundary condition. The general layout of this computational domain is the same used for the three-dimensional simulations, even though mesh refinements have been slightly increased. On the frame surface, a No-Slip wall boundary conditions has been used as well. The total two-dimensional cell amount depends on the dimension of each grid parameter and analysed shape, but, namely, it's about 120k cells. With such mesh dimension, a reasonable time for performing the overall optimization process has been obtained. The inlet velocity value is 3.6 m/s, the same figure used for the preliminary three-dimensional simulations.

For investigating the frame cross-section shape effects on aerodynamic performance, the parameter set in Figure 25 have been defined: the parameter set includes the holes number, dimension and position, the dimension of simple vortex generator (defined by the *Top Cap Closure* parameter) and the *Sensor Hole Closure* for improving sensor protection. Keeping the main frame dimensions unchanged, the principal idea has been to create some guide vanes on the frame surface reduce the drag: the number and the dimensions of the guide vanes are two of the investigated parameters. Thus, modifying each of these parameters, it is possible to obtain an optimized cross-section which allows some of the flow to go through, reducing frame drag, and some of the flow to be tilted up, generating a certain amount of downforce. Furthermore, a proper angle of those guide vanes can further increase the frame aerodynamic performance.

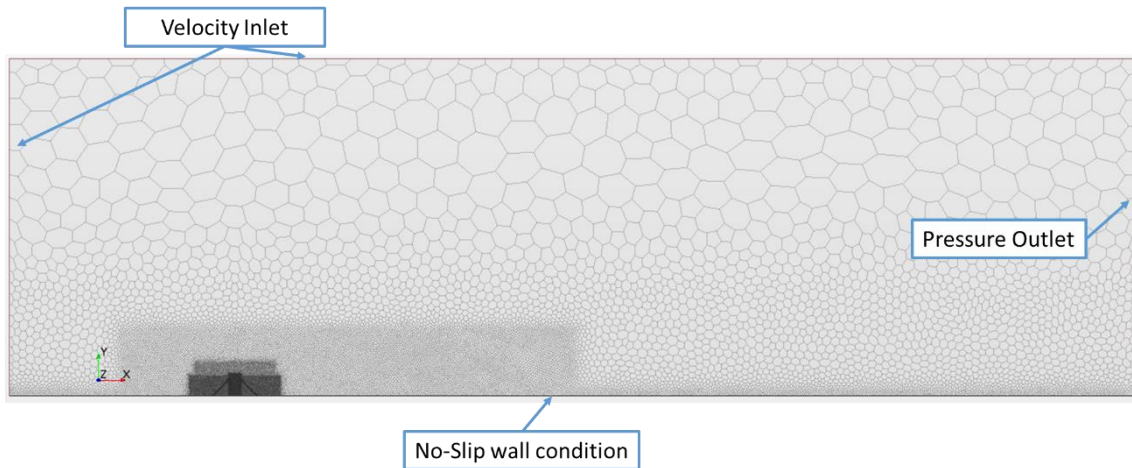


Figure 24 – Two-dimensional simulation computational domain with indication of boundary conditions

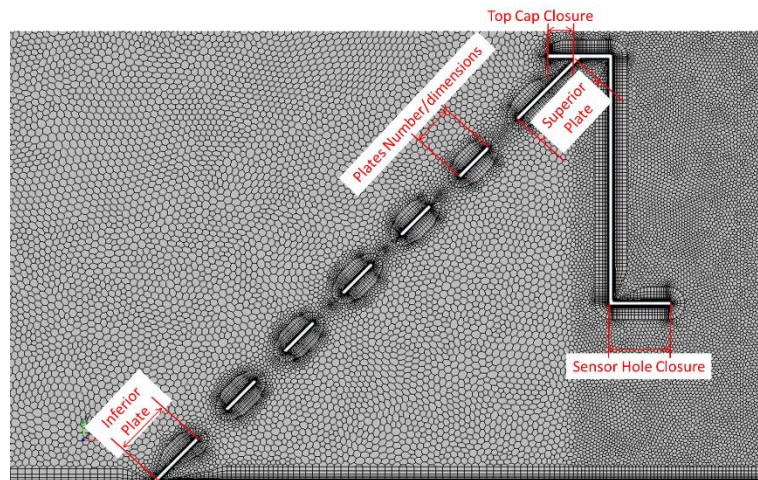
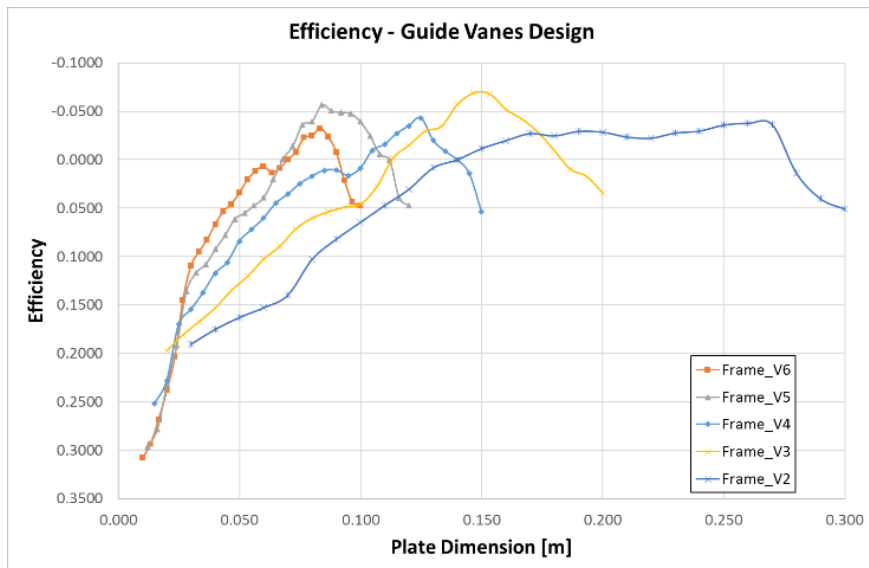


Figure 25 – Two-dimensional simulation parameters for optimization purposes

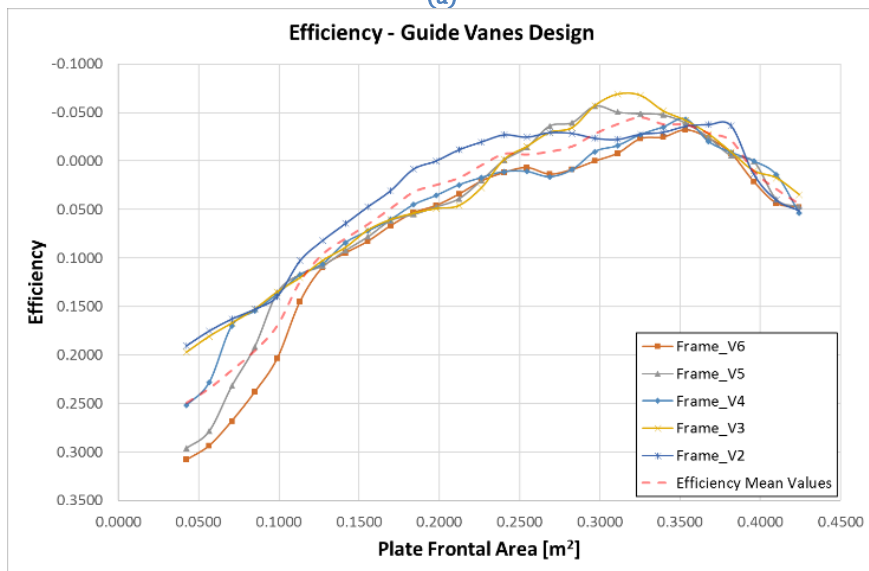
Every parameter has been analysed using a single objective optimization (each parameter has been modified keeping the others fixed) and the effects of each parameter dimension have been compared in terms of aerodynamic efficiency (E). The results are presented in Figure 26: it shows the lift-to-drag ratio of the frame equipped with different number of guide vanes (indicated by the number in the legend, so the Frame_V4 is equipped with 4 plates), comparing their dimension effects in the range 0.010 m to 0.300 m, depending on the plate number.

In order to compare all these analysed configurations with different guide vanes number and dimensions, the frontal area generated by each configuration has been considered. It's almost clear from Figure 26 – (b) that the maximum value of the downforce-to-drag value occur when the vanes frontal area is in the range $0.300 \text{ m}^2 \div 0.375 \text{ m}^2$, with very small differences among such configurations. The highest aerodynamic efficiency value has been observed for the Frame_V3 configuration (that is with three guide vanes), having an efficiency value of -0.0688: the three vanes are equally spaced and their length is of 0.147 m each.

Concerning the plate angle, the investigated angle range is from 0° , when these vanes are aligned with superior and inferior plates, to 45° , which correspond to have these vanes aligned with the flow direction. The plate angle upper limit comes from the consideration that, for further angle increments, they will produce an upward lift force instead than a downward one. As expected, in Figure 27 it's shown that the maximum aerodynamic efficiency occurs at 0° for all the configuration, as increasing this angle reduces the vanes angle of attack, that is the angle between the flow direction and the vanes surfaces.



(a)



(b)

Figure 26 – Plate dimensions and number analysed configuration

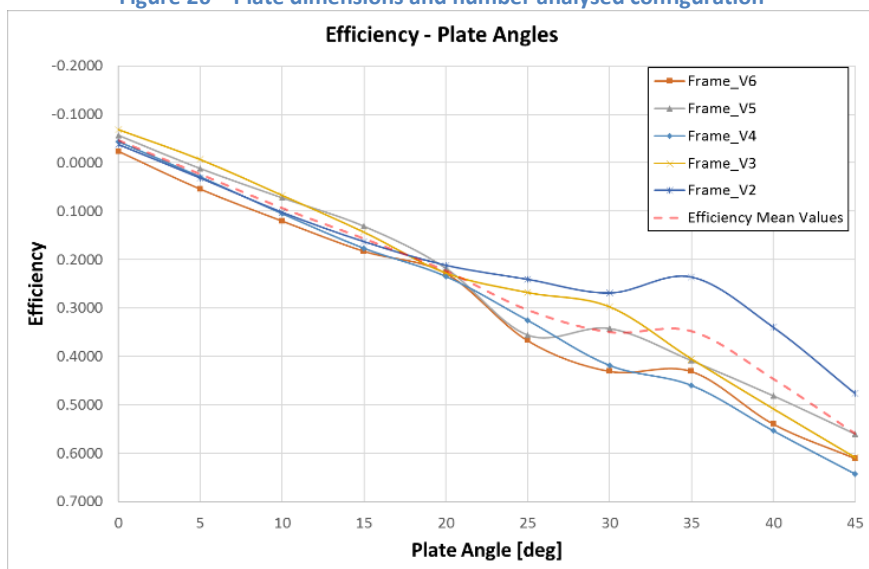


Figure 27 – Plate angle for each analysed configuration

Using the Frame_V3 two-dimensional configuration, the secondary investigated parameters have been the dimension of the so-called *Inferior Plate* (the plate closer to the seabed) and the *Superior Plate*, while the sensor bucket length has remained unchanged. In this way, the relative position of the guide vanes has been analysed, as these guide vanes are equally spaced to fit the space between the *Inferior Plate* and the *Superior Plate*. Being fixed the dimension and the number of plates (three equally spaced plates of 0.147 m length), the *Inferior Plate* and the *Superior Plate* dimensions are interconnected, as the sum of the two dimensions has to be 0.250 m. So, the Figure 28 shows also the effect of positioning such vanes on different positions along the frame outside surface: it results that these three guide vanes work better when they are closer to the seabed, as the best *Inferior Plate* length is 0.090 m while the *Superior Plate* one is 0.160 m. Another remarkable observation is that, choosing values in the range 0.070 m ÷ 0.090 m for the *Inferior Plate* and 0.180 m ÷ 0.160 m for the *Superior Plate*, there is no much difference in terms of frame aerodynamic efficiency.

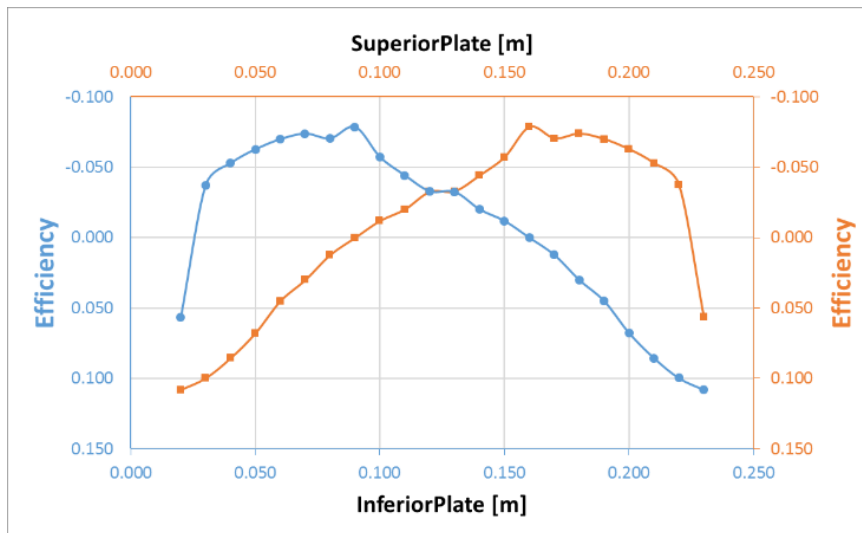


Figure 28 – Superior and Inferior plate dimensions effects

Lastly, the possibility of reducing the bottom bucket hole for improving sensor protection (modifying the *Sensor Hole Closure*) and the presence of a simple vortex generator (here named *Top Cap Closure*) have been examined as well. For those last two parameters, only the horizontal extension has been changed. The Figure 29 shows how the presence of a small vortex generator can improve the frame performance: in particular, when the *Top Cap Closure* dimension is 0.040 m, the frame shows an increased efficiency due to the interaction of such vortex generator with the flow field around the frame; also, a notable result is that longer vortex generator lengths seem to work in an opposite way than the shorter ones. A possible explanation of the trend observed in Figure 29 is that, increasing the vortex generator dimension, the flow is blocked to tilt up and is pushed to go inside the sensor frame, through the guide vanes. Such effect, that is strong in a completely two-dimensional flow field (as no out-of-plane velocity component are allowed) should be less pronounced in a three-dimensional flow field. Concerning the dimension of the *Sensor Hole Closure* parameter, no relevant effects have been observed, being this surface well inside the frame and protected by the other outside surfaces.

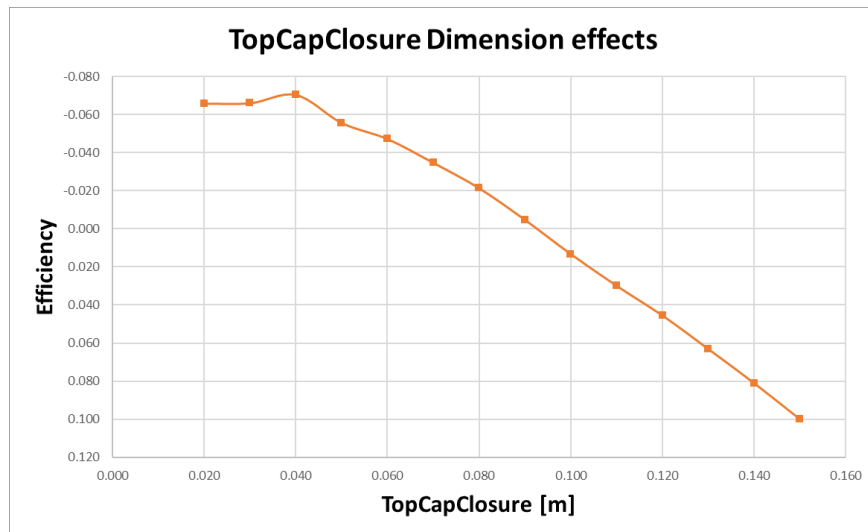


Figure 29 – Top Cap Closure dimension effects

Using the parameters dimensions obtained from optimization is possible to modify the Frame_#0: the optimized Frame_#0 is shown in Figure 30. This frame could be defined as the result of a blending process of the Frame_#0 and the Frame_#1, as it includes an improved version of the Frame_#1 closing plates. The total weight of the frame in Figure 30 is 169 kg, that is 43% heavier than Frame_#0 and 10% lighter than Frame_#1. Despite its attractive characteristics, such frame has not been considered as a suitable frame for deployment, due to the complexity and the effort involved for its manufacture process. Anyway, even if no three-dimensional simulations have been run on this frame configuration, some of the former optimization results have been used lately for the definition of some of the new frame features.

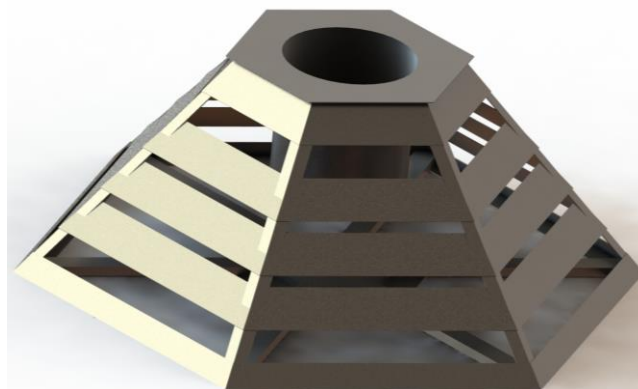


Figure 30 – Optimized configuration of the Frame_#0

Preliminary design of the Frame_#2 specific

To define a completely new frame design, the first step has been to compare the performance of different base shapes. Using two-dimensional simulations, the effects of different base shapes have been investigated. The two-dimensional simulation computational domain used for this purpose is the same in Figure 24, where the No-Slip boundary condition at the bottom has been substituted with a symmetry boundary condition (it's worth to notify that, namely, there is no big difference between a Slip wall boundary condition and a symmetry one). Considering that the Frame_#0 and Frame_#1 base shape is a six edges shapes (later called Hexa), five different base shapes have been analysed. Such shapes have all a common dimension for comparison purposes:

Cyl: a cylinder with a 1.0 m radius, comparable with the Frame_#0 main dimension

Deca: a shape with ten edges, included inside the 1.0 m radius cylinder (each side is 0.62 m length)

Hexa: a shape with six edges, like the Frame_#0 and Frame_#1, included inside the 1.0 m radius cylinder (each side is 1.0 m length)

Rect: a rectangular shape, included inside the 1.0 m radius cylinder (each side is 1.41 m length)

Tri: a triangular equilateral shape, included inside the 1.0 m radius cylinder (each side is 1.73 m length)

Not all the bespoke shapes (i.e., the cylinder) are sensitive to flow direction; but, to see how their performance are influenced by the flow direction, two flow angles have been tested: $\theta=0^\circ$ (the flow approaches the edge of the analysed shapes, as indicated for the former analysed cases) and a particular θ value to cause that the flow direction is perpendicular to one of the sides of the analysed shapes. Such θ depends on the base shape under investigation as the edge number and angles are different.

Although the results in Figure 31 shows clearly that using a cylinder shape assures less flow sensitivity and lower two-dimensional drag coefficient, this figure doesn't show one of the well-known troubles related with such shape: in particular flow condition (speed and turbulence), the cylindrical shape is prone to exhibit strong vortex shedding phenomena, which represent a big issue for measurements: the vortex induced vibrations can affect strongly the measurement accuracy. Thus, even though the Deca and Hexa shapes have both a slightly lower drag coefficient, due to the frame manufacturability aspect and the limited flow direction sensitivity, the Rect shape has been chosen as base shape. The Rect shape has shown good performance compared with the other analysed shapes: in fact, the higher drag coefficient of the Rect shape at $\theta=0^\circ$ is mostly due to the bigger flow exposed area as compared with the other shapes (likely the Tri shape exposed to mid-plate flow). The Figure 32 shows a comparison of the flow fields generated by the different base shapes.

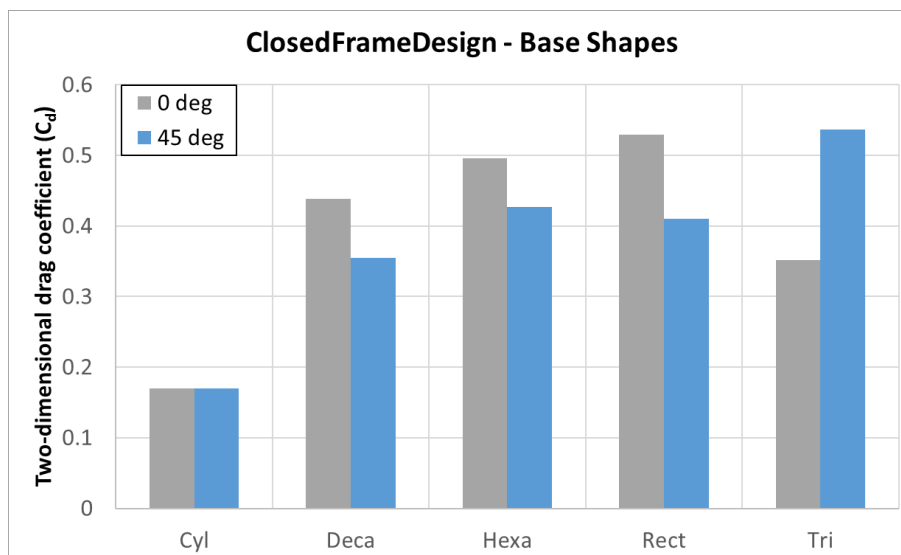
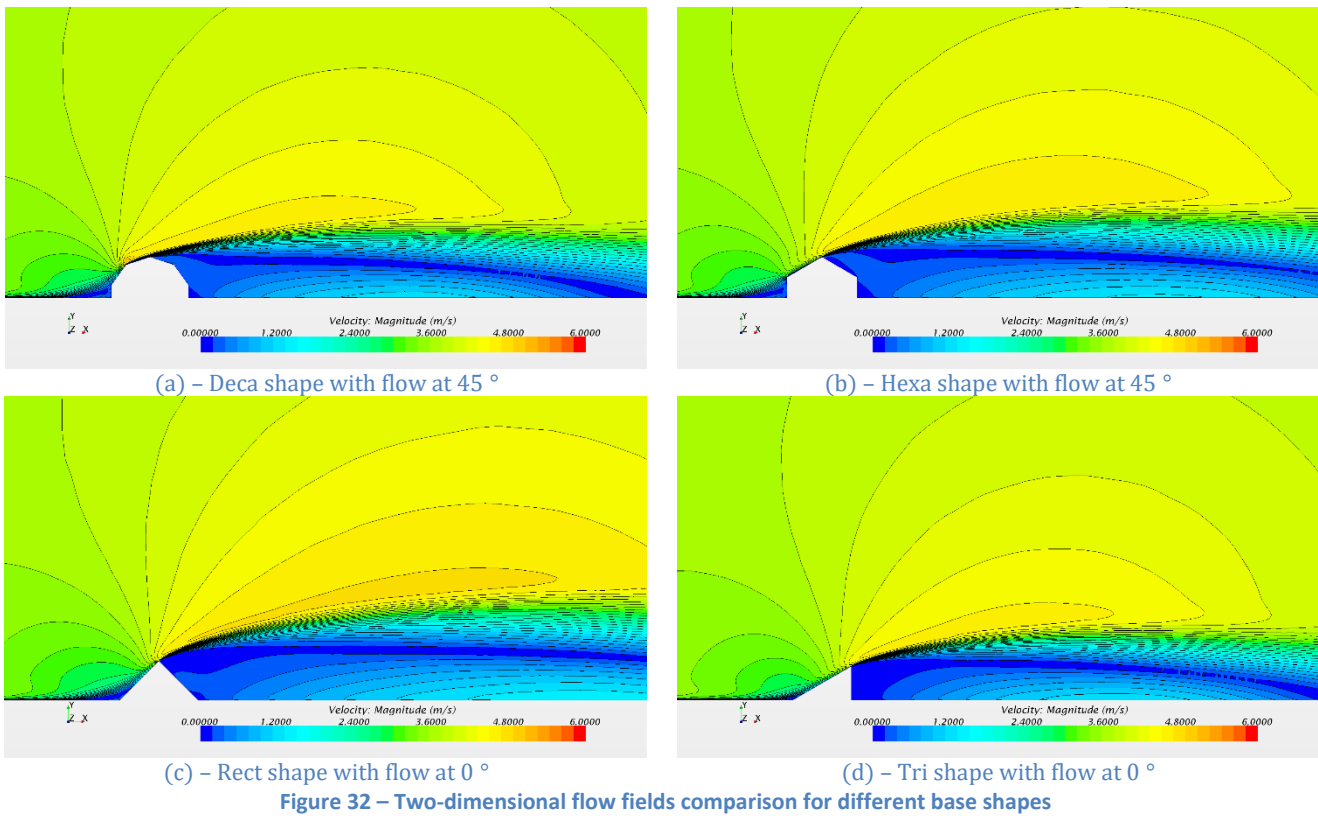


Figure 31 – Two-dimensional performance comparison of different base shapes



Using the same approach of Figure 17, it is possible to estimate the effect of the so-called plate angle, assuming that the plate behaves like an inclined flat plate. During the years, a number of experiments have been carried out: from [12], the Figure 33 shows how the C_N changes with the angle of attack (AOA). As defined before, the normal force coefficient C_N is the sum of the lift and drag coefficients of such flat plate, shown in Figure 34 with the indication of C_L and C_D as well. For our purposes (see Figure 17 – (c)), we are interested on AOA values bigger than 90 °: the Figure 34 clearly indicates that for AOA greater than 90 ° the C_L is negative due to a downward force.

The Figure 36 zooms the area of interest for practical reasons. In fact, the minimum value of the plate internal angle (α) is 25 °, as lower values don't allow easy operation inside the frame. Moreover, it exists a lower allowable limit of 40 ° for the plate internal angle (α): this 40 ° limit is necessary to have main dimensions similar to Frame_#0 and Frame_#1. Indeed, the Figure 35 depicts that, for lower α angles, the x dimension would be higher than d or D , being fixed the frame height at 0.75 m.

The values of C_L and C_D for each suitable α angle are stated in Table 11: the C_L and C_D values have been evaluated using both the so-called approximated method (Figure 17 – (a), from [12]) and the experimental data from Figure 33. The Figure 36 shows the comparison of the two methods, highlighting the coefficients overestimation of the approximated method respect to the experimental results. From Table 11 it's evident that having a flat plate with α angle as lower as practicable promises lower drag and higher downforce. Hence, the lower practicable angle to use is $\alpha=45$ °, which produces the lower drag with the higher downforce.

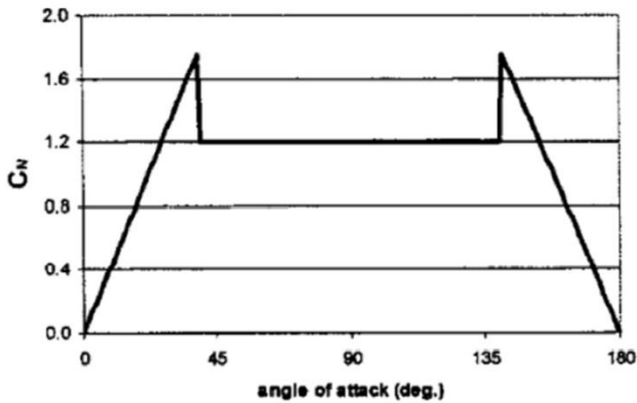


Figure 33 – Normal force coefficient of a flat plate at AOA [12]

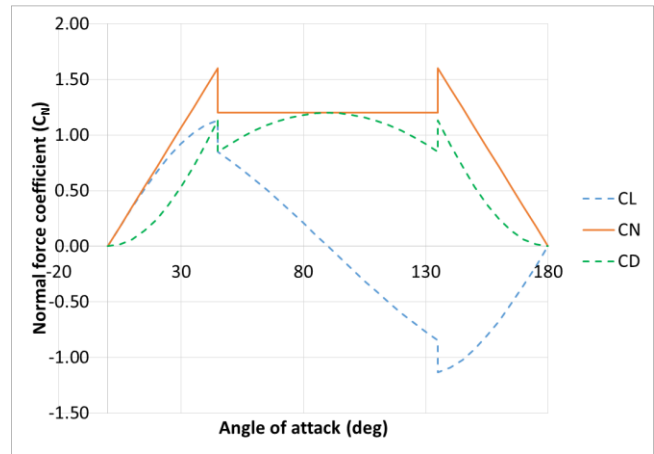


Figure 34 – Drag and lift coefficients of a flat plate at AOA

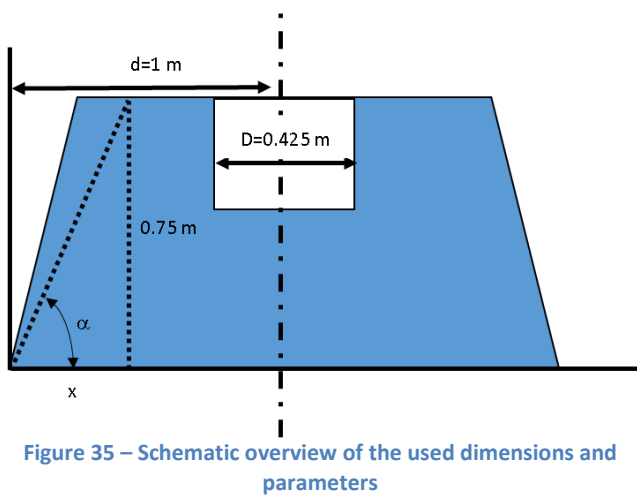


Figure 35 – Schematic overview of the used dimensions and parameters

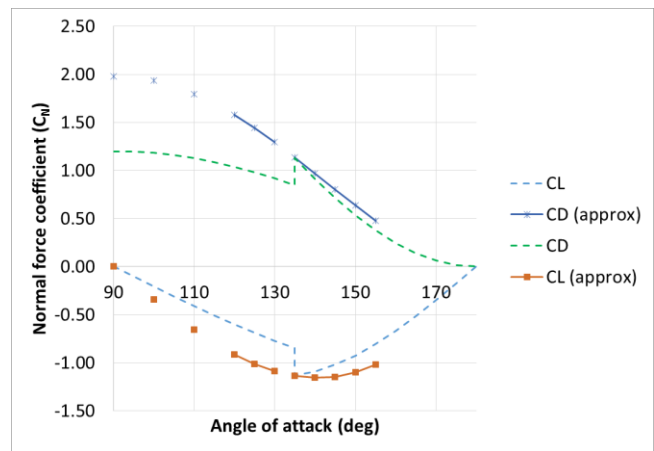


Figure 36 – Comparison of data for a flat plate at AOA from two different methods

Table 11 – Numerical data used for Figure 36

α	x	S [m ²]	θ	From Figure 33 - Experimental			Using Figure 17 – Approx. method			
				C _N	C _D	C _L	C _N	C _D (approx.)	C _L (approx.)	
25	1.609	>d	0.147	155	1.20	0.474	-1.017	1.122	0.474	-1.017
30	1.300	>d	0.263	150	1.20	0.635	-1.100	1.269	0.635	-1.099
35	1.071	>d	0.348	145	1.20	0.802	-1.145	1.398	0.802	-1.145
40	0.894	<D	0.415	140	1.20	0.971	-1.157	1.510	0.971	-1.157
45	0.750	0.469	135	1.20 ÷ 1.60	0.849 ÷ 1.137	-0.848 ÷ -1.136	1.607	1.137	-1.136	
50	0.630	0.514	130	1.42	1.300	-1.087	1.691	1.296	-1.087	
55	0.525	0.553	125	1.24	1.444	-1.011	1.762	1.444	-1.011	
60	0.433	0.588	120	1.07	1.578	-0.911	1.822	1.578	-0.911	
70	0.273	0.648	110	0.71	1.796	-0.654	1.912	1.796	-0.654	
80	0.132	0.700	100	0.36	1.933	-0.341	1.963	1.933	-0.341	
90	8.7E-05	0.750	90	0.00	1.980	0.000	1.980	1.980	0.000	

With the above results about the plate internal angle ($\alpha=45^\circ$), some two-dimensional investigation have been performed to investigate how frame vertical displacements from the seabed (seabed clearance) can influence the frame aerodynamic performance. Having such bottom clearance allows a certain amount of fluid to flow underneath the frame; moreover, being the simulated frame completely closed at the bottom, there is no possibility for water to run through the frame, from the bottom to the top. The Figure 38 shows the effect of letting some flow pass below the sensor frame, a very normal situation experienced during deployments. Due to the seabed roughness and uneven bathymetry in the deployment areas, it is more likely that there would be a gap between the sensor frame and the seabed itself. In the light of this, having a fully closed frame bottom could affect its stability: indeed, the frame bottom can hit the seabed in different points respect to the designed ones, resulting in a less stable configuration. As discussed before for the vortex shedding

phenomena, unstable situations must be avoided to improve measurements accuracy and then, even if having a closed bottom frame seems to help its aerodynamic performance, the final frame will be open to improve its stability.

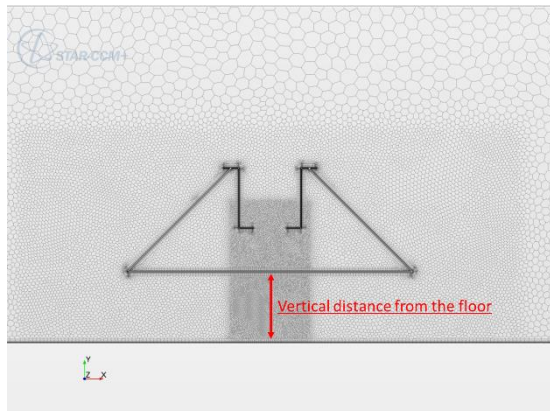


Figure 37 – Vertical distance from the floor parameter

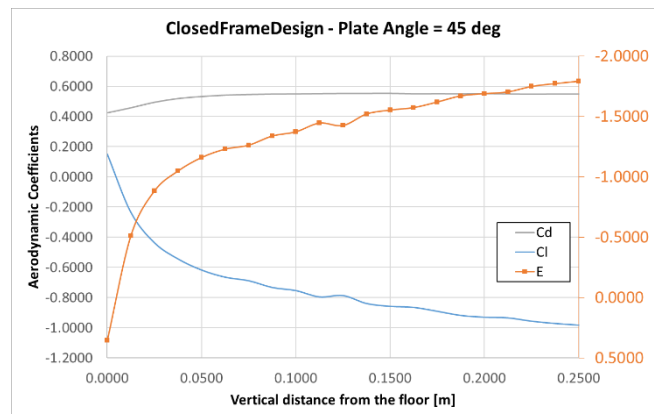


Figure 38 – Two-dimensional performance of a vertically displaced frame

Using the above two-dimensional results, a new frame (Frame_#2), with rectangular base, has been designed and used for more accurate three-dimensional CFD analysis. The overall dimensions of Frame_#2 in Figure 39 are the same of Frame_#0 and Frame_#1, unless that the base shape is rectangular (Rect) instead than hexagonal (Hexa). The maximum footprint of the Frame_#2 is 2.0 m, that is equal to the maximum base distance (corner-to-corner) of the Frame_#0 and Frame_#1.

Figure 39 – (a) and Figure 39 – (b) represent the frame when the flow is perpendicular to the external plate ($\theta = 45^\circ$) whereas Figure 39 – (c) and Figure 39 – (d) are related to the flow approaching one of the frame edge ($\theta = 0^\circ$). These two flow conditions are exactly similar to the $\theta=30^\circ$ and $\theta=0^\circ$ for the Frame_#0 and Frame_#1. In terms of simulations setup and flow speed, the data used for analysing the Frame_#2 have been the same of Frame_#0 and Frame_#1. In Table 12 the results of the mesh independence analyses for the Frame_#2 are presented. Such frame specification produces more downforce than the Frame_#1, even though the drag is almost the same.

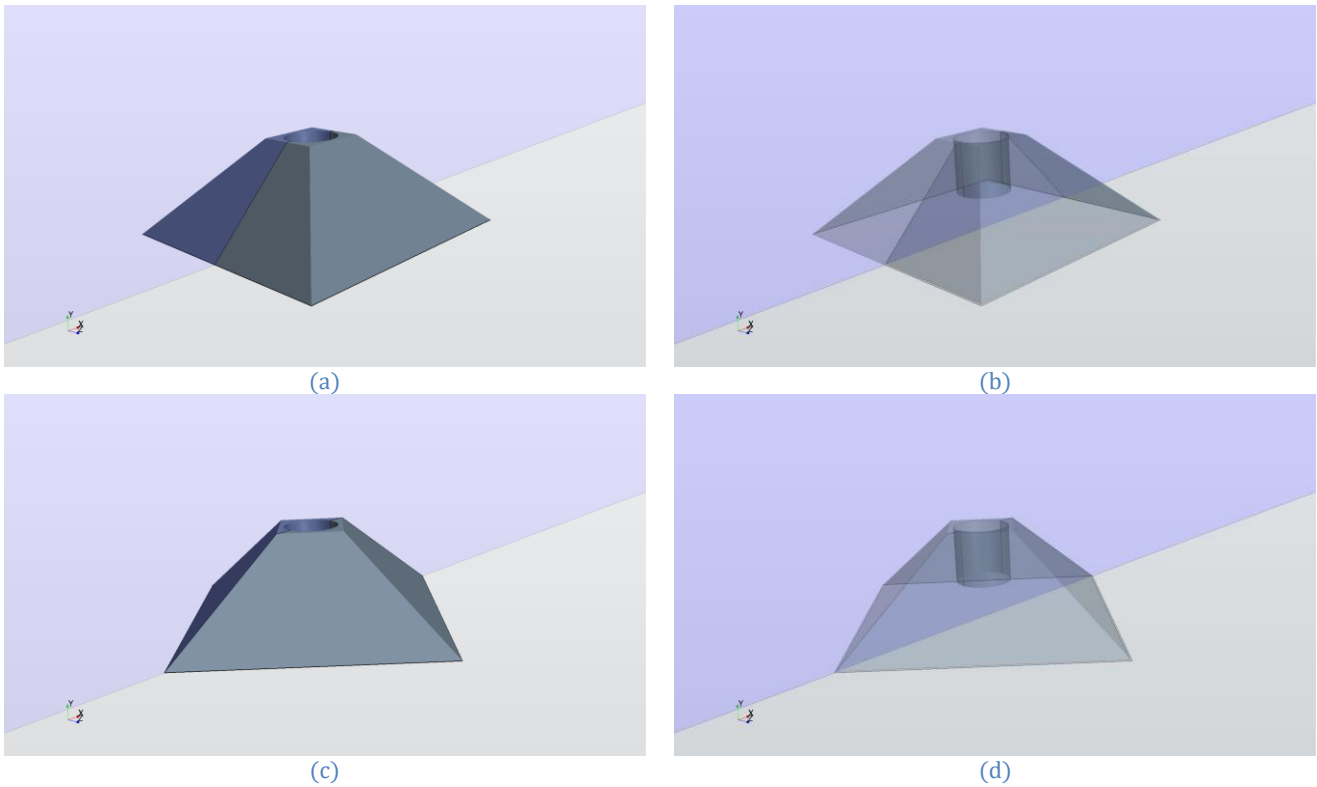


Figure 39 – Rectangular base frame with same principal dimensions of the Frame_#0 and Frame_#1

Table 12 – Frame_#2 mesh independence study data

BaseSize [m]	CellsNumber	C_D (@0°)	ΔC_D	C_L (@0°)	ΔC_L	BaseSize [m]	CellsNumber	C_D (@45°)	ΔC_D	C_L (@45°)	ΔC_L
2.00		0.567	-2.16%	-0.573	18.72%	2.00	4.60E+06	0.630	5.26%	-0.644	7.34%
1.50	8.61E+06	0.562	-1.26%	-0.732	-3.83%	1.50	6.80E+06	0.650	2.26%	-0.688	1.01%
1.25	11.7E+06	0.559	-0.72%	-0.739	-4.82%	1.25	8.90E+06	0.651	2.11%	-0.678	2.45%
1.00	17.0E+06	0.555		-0.705		1.00	14.4E+06	0.665		-0.695	

In Table 13 the data of Frame_#2 are compared with the ones of Frame_#0 and Frame_#1. The Frame_#2 shows increased drag and downforce as compared with Frame_#1: in particular, at $\theta = 0^\circ$, drag coefficient is reduced of about 23%, along with a 21% increased downforce coefficient; in the other flow condition under test, drag coefficient reduction is less ($\Delta C_D = -2.5\%$) while the increased downforce is confirmed ($\Delta C_L = +25\%$). In terms of forces at $V=3.6$ m/s, in both the flow conditions there is an increased downforce of more than 30%; drag also increases of 20% at $\theta = 0^\circ$ and of 7% when the flow is right at the external plate centre.

Table 13 – Frame_#2 aerodynamic data

V = 3.6 m/s	$\theta = 0^\circ$				$\theta = 0^\circ$			
	C_D	C_L	D [N]	L [N]	C_D	C_L	D [N]	L [N]
Frame_#0	0.876	0.4703	2061	1107	0.759	0.525	2061	1425
Frame_#1	0.682	-0.555	3833	-3119	0.682	-0.520	4382	-3341
	$\theta = 0^\circ$				$\theta = 45^\circ$			
Frame_#2	0.555	-0.705	4728	-6006	0.665	-0.695	4015	-4196

Using the data of Table 13, it is possible to estimate and compare the needed amount of ballast for the Frame_#2 with the ones obtained for the Frame_#1 and Frame_#2. It is evident from Table 14 that, at the same steady velocity of 3.6 m/s, the Frame_#2 requires less ballast than the former frames, with a reduction of the total weight required for deployment.

Table 14 – Ballast evaluation for Frame_#2 based on a Sandstone seabed

Friction = $\mu \cdot (\text{Weight} - \text{Lift} + \text{AddedMass}) \text{ [N]} > \text{Drag}$							
Friction coefficient (Sandstone) $\mu = 0.340$	Drag [N]	Lift [N]	Frontal Area [m ²]	AddedMass [N]	AddedMass [kg]	Flow angle [°]	Total Weight [kg]
Frame_#0	2061	1107	0.182	5712	582	0	731
	2061	1425	0.210	6030	615	30	763
Frame_#1	3833	-3119	0.435	6015	613	0	831
	4382	-3341	0.497	7409	755	30	973
Frame_#2	4728	-6006	0.659	5236	534	0	805
	4015	-4196	0.467	4948	504	45	776

In real environments, the flow velocity isn't steady with a fixed value: it grows from 0 m/s at the seabed to the nominal flow velocity (V_s), within a distance called boundary layer. The boundary layer can be modelled or measured and, for our purpose, it has been assumed to follow the so-called 10th power law formula (Figure 40). Using equation (8), it is possible to estimate the expected velocity on the sensor frame top cap and, using that velocity, scale the value of forces and ballast as well. The assumption made here is that the aerodynamic coefficients don't change as a consequence of a velocity variation: this assumption isn't far from reality when the Reynolds number doesn't change abruptly (a big Reynolds number change means a big change in flow field structures, passing from laminar flow to turbulent one and vice versa).

$$V_D = 1.1 * V_s \qquad V(y) = V_D * \left(\frac{y}{H}\right)^{0.10} \qquad (8)$$

Using the 10th power law formula and assuming that the total frame sensor height is 0.8 m, a velocity of 2.70 m/s is obtained. The evaluation of the needed ballast for all the analysed frames is reported in Table 15. As before, the Frame_#2 total weight is less than the Frame_#1, mainly due to the change of the plate angle from 48°, for the Frame_#1, to the 45°, for the Frame_#2. Concerning the amount of ballast, the values reported here include the frame weight: those weights, for all the frame specifications later reported, are based on a CAD model estimation and, obviously, they can be different from the final frame structure.

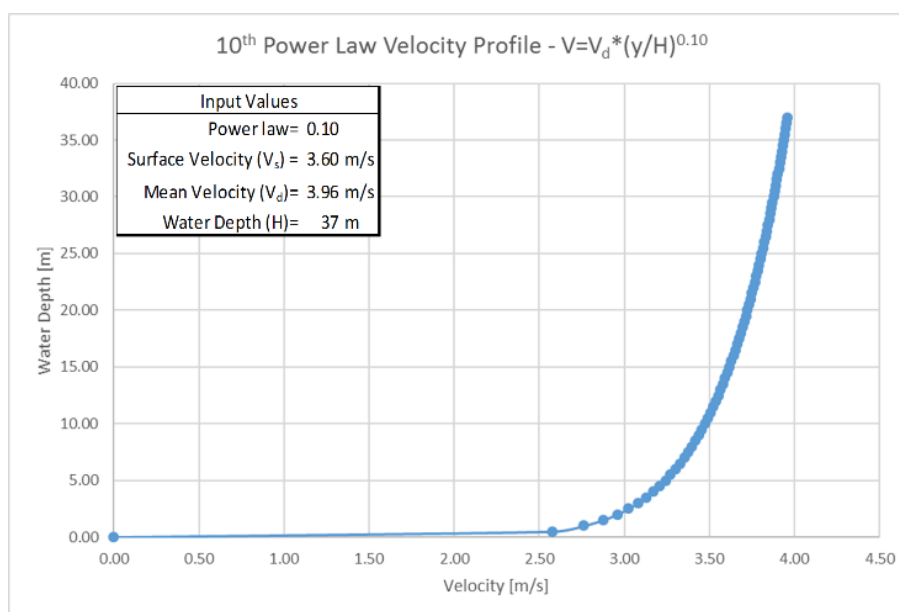
Figure 40 – 10th power law velocity profile

Table 15 – Ballast evaluation using the velocity from the 10th power law (2.70 m/s) on the frame top cap

Friction = $\mu \cdot (\text{Weight} - \text{Lift} + \text{AddedMass}) \text{ [N]} > \text{Drag}$

Friction coefficient (Sandstone) $\mu = 0.340$	Drag [N]	Lift [N]	Frontal Area [m ²]	AddedMass [N]	AddedMass [kg]	Flow angle [°]	Total Weight [kg]
Frame_#0 (118 kg)	1158	622	0.182	2573	262	0	411
	1158	801	0.210	2752	280	30	429
Frame_#1 (188 kg)	2154	-1753	0.435	2444	249	0	467
	2463	-1878	0.497	3227	329	30	547
Frame_#2 (241 kg)	2658	-3376	0.659	1776	181	0	453
	2257	-2358	0.467	1614	165	45	436

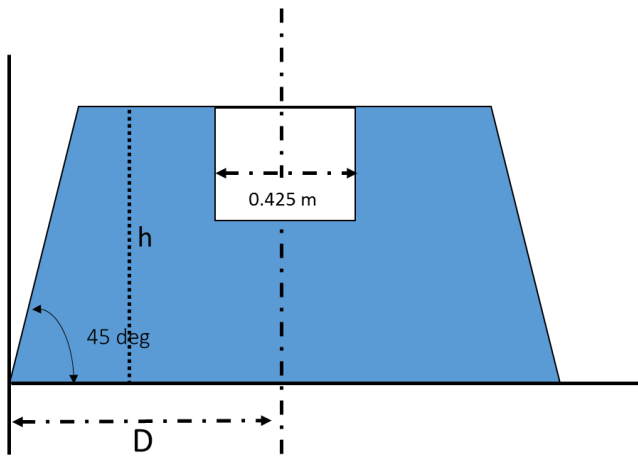
Optimizing Frame_#2 shape: the Frame_#3

One of the parameter involved into the aerodynamic force generation is the frame frontal area (see (4)): the aerodynamic forces depend linearly on the frontal area (S) and quadratically on the flow speed (V). Thus, the only design parameters involved into the aerodynamic forces equations are the drag and lift coefficients and the frame frontal area. Supposing that the environmental conditions doesn't change sharply and, in turn, the Reynolds number remains at the same order of magnitude, it is possible to reduce the aerodynamic forces (especially, the drag force that is detrimental for the frame seakeeping performance) limiting the frame frontal area as much as possible.

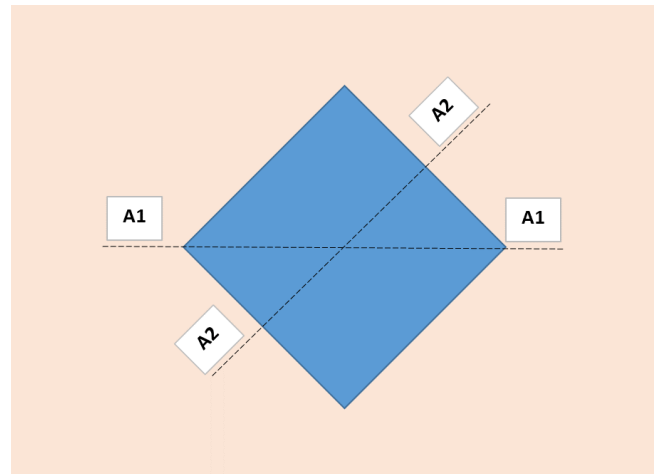
Being some dimensions fixed by the space needed by the sensor, the other parameters involved in defining the final frame shape are not independent: to keep the plate internal angle at $\alpha=45^\circ$, both the frame footprint and height have to be modified (see Figure 41 – (a)). Moreover, the frontal area values depend on the flow direction (Figure 41 – (b)) as well as the frame height will affect the highest velocity on the sensor frame top cap. In fact, having a lower frame height is helpful because it reduces the speed at the frame top cap, as the flow velocity develops following a law similar to Figure 40.

Using the notation in Figure 41, the height and, consequently, the frame footprint of the Frame_#2 have been scaled: in Figure 42 and Figure 43 are presented how the frame weight and the frontal area change due to a reduction of the frame height. The interesting result is that, keeping the internal angle of $\alpha=45^\circ$, the frontal area can be reduced up to 87%, from $A_1=0.6629 \text{ m}^2$ to $A_1=0.3535 \text{ m}^2$ and from $A_2=0.4687 \text{ m}^2$ to $A_2=0.2500 \text{ m}^2$. Such reductions have also a huge impact on the frame total weight, which is expected to reduce from 264 kg to 177 kg. Using these values, it has been possible to evaluate how the ballast are affected by frame height changes, obtaining the curves in Figure 44. These curves have been obtained supposing that the frame drag and lift coefficients don't change. The Figure 44 includes the comparison between the cases with a steady velocity of 2.70 m/s and the ones in which the velocity reduces in accordance to the frame height (the top cap reference velocity changes with frame height), following the equation (8).

In the validity of the bespoke assumption, it's evident that a remarkable reduction of ballast can be obtained reducing the frame height and, also, that an overestimation of the needed ballast results using a fixed velocity value.



(a)



(b)

Figure 41 – Frontal area design parameters

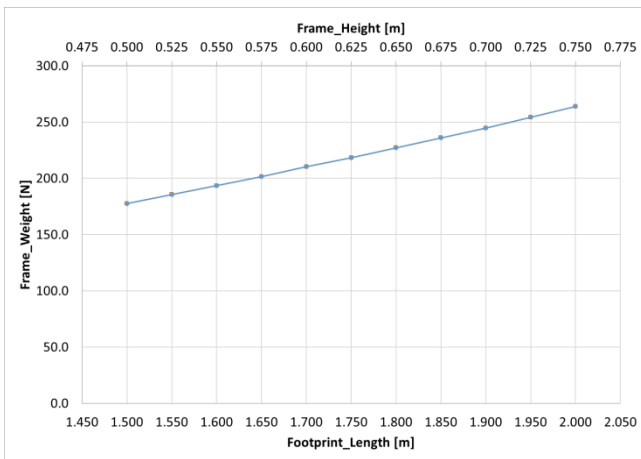


Figure 42 – Height scaling effect on frame weight

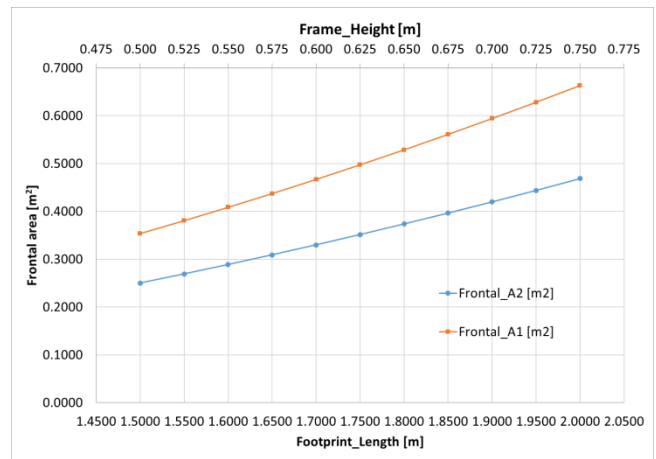


Figure 43 – Height scaling effect on frame frontal area

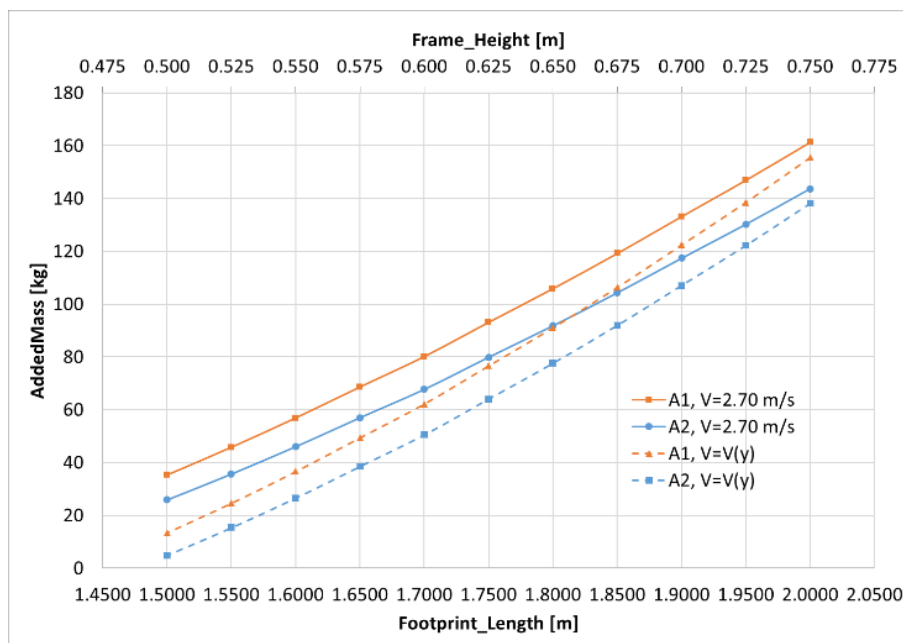


Figure 44 – Height scaling effect on frame ballast

This preliminary examination has conducted to the definition of a 0.500 m height sensor frame (Frame_#3) to be analysed with CFD. For the CFD analysis purposes, the frame has been defeatured,

preserving only the footprint length (1.500 m on each side), the height (0.500 m), the bucket size (0.430 m) and the bucket length (0.400 m). As before, only half of the Frame_#3 has been modelled inside the same CFD domain, applying symmetry condition on the symmetry plane. In Table 16, the results of the clean Frame_#3 configuration are reported for different levels of grid refinements: the final results of C_D and C_L , in the same flow conditions, show that reducing the frame height slightly affects the non-dimensional coefficients.

Table 16 – Frame_#3 mesh independence study data

BaseSize [m]	CellsNumber	C_D (@0°)	ΔC_D	C_L (@0°)	ΔC_L	BaseSize [m]	CellsNumber	C_D (@45°)	ΔC_D	C_L (@45°)	ΔC_L
2.00		0.549	1.48%	-0.290	-60.06%	2.00	3.50E+06	0.630	0.80%	-0.180	-75.38%
1.50		0.545	0.74%	-0.583	-19.70%	1.50	5.15E+06	0.616	-1.44%	-0.715	-2.19%
1.25		0.543	0.37%	-0.662	-8.82%	1.25	7.00E+06	0.622	-0.48%	-0.708	-3.15%
1.00	1.50E+07	0.541		-0.726		1.00	9.88E+06	0.625		-0.731	

Comparing the data for the Frame_#2 and Frame_#3 (Table 17), the latter results improved in terms of drag reduction and downforce generation, in all the tested flow conditions. By the way, even if such improvement don't seem huge in terms of coefficients, it causes an important reduction of the forces on the frame, being the frontal area reduced.

Table 17 – Frame_#3 mesh independence study data

	C_D (@0°)	ΔC_D	C_L (@0°)	ΔC_L	C_D (@45°)	ΔC_D	C_L (@45°)	ΔC_L
Frame_#2	0.555		-0.705		0.665		-0.695	
Frame_#3	0.541		-0.726		0.625		-0.731	
		-2.58%		+2.89%		-6.40%		+4.92%

Being 0.5 m the Frame_#3 height, the flow velocity on the frame top cap is 2.57 m/s (using the 10th power law of Figure 40): with this flow velocity, the drag force is reduced of about 46%, whereas the lift force is about 51% less. The effects of these reductions on the needed ballast are shown in Table 18: as compared with the previous configurations, the Frame_#3 doesn't need any ballast: indeed, using the equation (7), the ballast estimation gives negative values, meaning the Frame_#3 weight can easily hold itself on the seabed.

Table 18 – Ballast evaluation using the velocity from the 10th power law on the frame top cap

$$\text{Friction} = \mu * (\text{Weight} - \text{Lift} + \text{AddedMass}) [\text{N}] > \text{Drag}$$

Friction coefficient (Sandstone) $\mu = 0.340$	Drag [N]	Lift [N]	Frontal Area [m ²]	AddedMass [N]	AddedMass [kg]	Flow angle [°]	Total Weight [kg]
Frame_#0 (118 kg, V=2.70 m/s)	1158	622	0.182	2573	262	0	411
	1158	801	0.210	2752	280	30	429
Frame_#1 (188 kg, V=2.70 m/s)	2154	-1753	0.435	2444	249	0	467
	2463	-1878	0.497	3227	329	30	547
Frame_#2 (241 kg, V=2.70 m/s)	2658	-3376	0.659	1776	181	0	453
	2257	-2358	0.467	1614	165	45	436
Frame_#3 (199 kg, V=2.57 m/s)	1277	-1714	0.357	-206	-21	0	229
	1046	-1223	0.253	-396	-40	45	229

Some flow field visualizations around the Frame_#3 are in Figure 45, for both $\theta = 0^\circ$ and $\theta = 45^\circ$ flow directions. The flow field around the Frame_#3 is almost similar to the Frame_#1, even though the base shape is different. From Figure 45, it's evident that, being very smooth at the external surfaces, some flow is allowed to enter inside the bucket, where normally the ADCP sensor is installed.

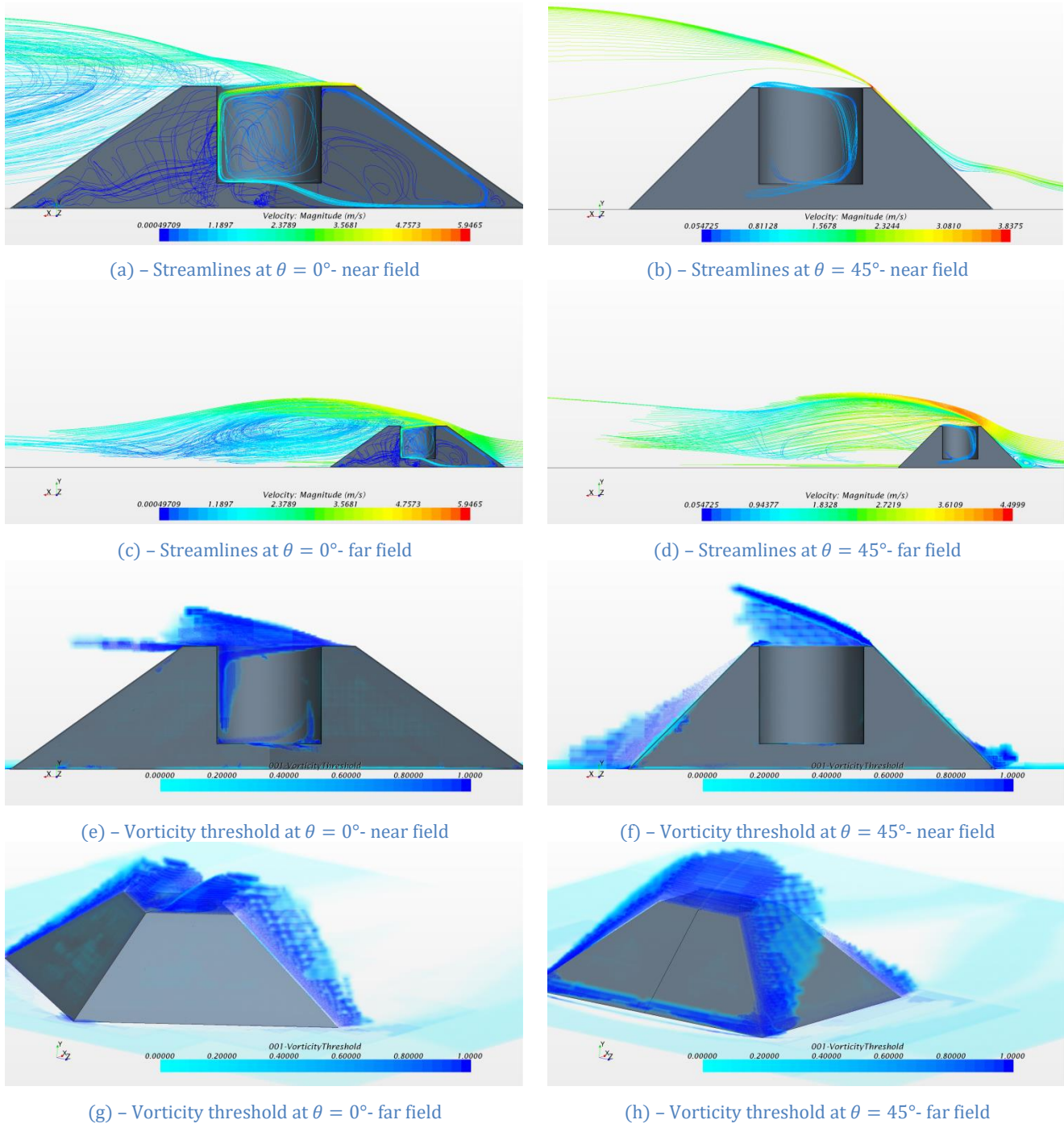


Figure 45 – Flow field visualization for the Frame_#3

To improve sensor protection and avoid unwanted sensor tilting (as explained in Figure 16), some other investigations have been performed fitting a vortex generator on the frame top cap. Two different vortex generator shapes have been tested: the first one (VG_1) in Figure 46 – (b) is a flat plate vortex generator, whose dimensions and angle of inclination can be adjusted; the second one (VG_2, VG_3), in Figure 46 – (c) and Figure 46 – (d), are equilateral pyramidal shapes, whose dimensions and distances from the top cap edge can be modified.

Concerning the VG_1 vortex generator, its main dimension, that is the distance from the top cap, has been already investigated using two-dimensional simulations. From Figure 29, the length of 0.040 m causes the best lift-to-drag ratio. Hence, that dimension has been also tested by means of three-dimensional simulations. Furthermore, the angle respect to the horizontal top cap surface has been investigated as well.

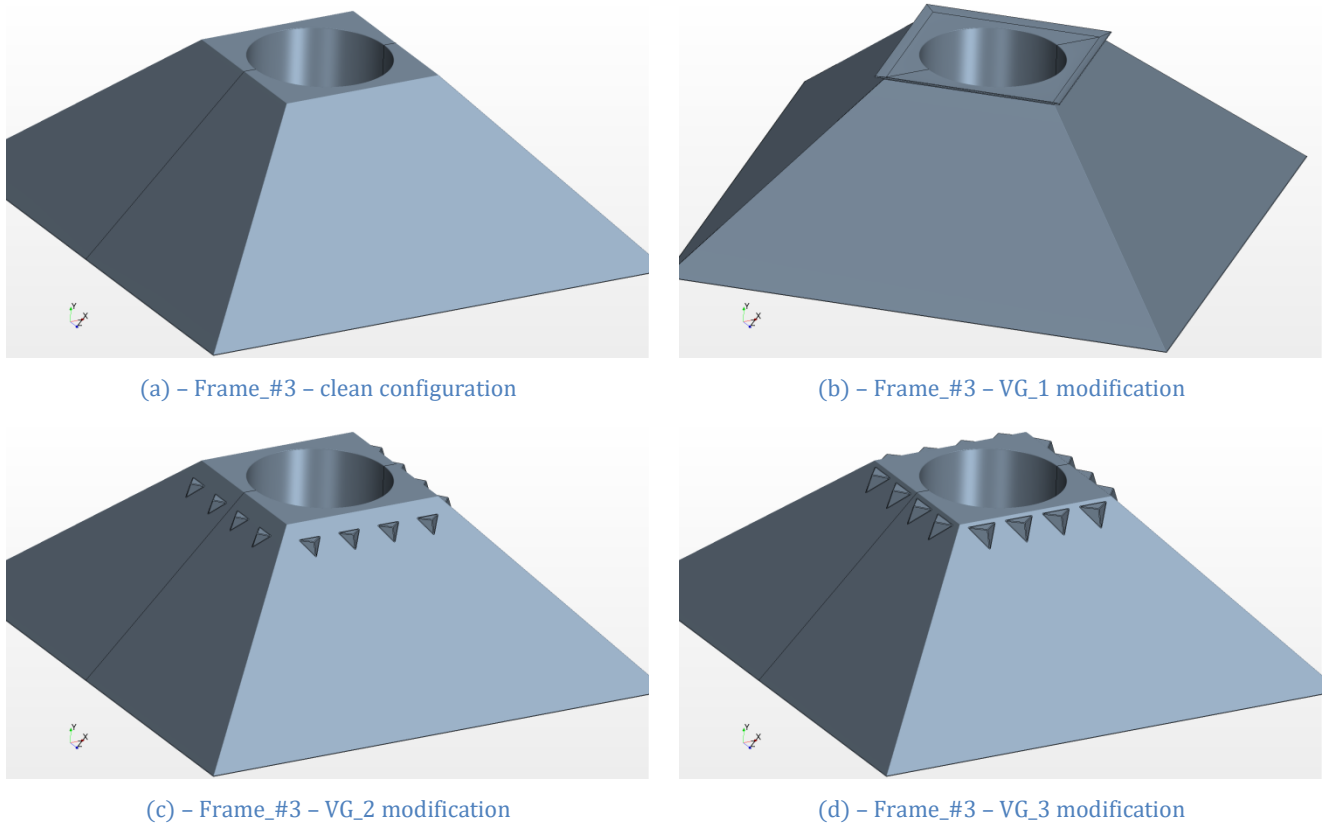


Figure 46 – Comparison of different vortex generator shapes fitted on Frame_#3

Frame_#3 performance results improved by the use of such VG_1 vortex generator and such improvements are more evident when the velocity increases. This feature is of matter of importance as it assures that the frame could be deployed safely in stronger flow conditions, due to its increased downforce. In fact, the aerodynamic forces difference between the Frame_#3 clean configuration and the Frame_#3 fitted with the VG_1 vortex generator increases with the flow speed.

In Table 19, the aerodynamic coefficients of the Frame_#3 with the VG_1 parallel to the top cap surface (later indicated at 0°), over different meshes, are summarized. These data show that the Frame_#3 with VG_1 vortex generator produces both more drag (+8.9% at $\theta = 0^\circ$ and +11.7 at $\theta = 45^\circ$) and more downforce (+12.4% at $\theta = 0^\circ$ and 7% at $\theta = 45^\circ$) when compared with the clean configuration.

Table 19 – Frame_#3 with VG_1 vortex generator mesh independence study data

BaseSize [m]	CellsNumber	C_D (@ 0°)	ΔC_D	C_L (@ 0°)	ΔC_L	BaseSize [m]	CellsNumber	C_D (@ 45°)	ΔC_D	C_L (@ 45°)	ΔC_L
2.00	6.10E+06	0.597	1.36%	-0.834	2.21%	2.00	4.10E+06	0.675	-3.30%	-0.801	2.43%
1.50	9.40E+06	0.591	0.34%	-0.824	0.98%	1.50	6.20E+06	0.696	-0.29%	-0.780	-0.26%
1.25	1.30E+07	0.589		-0.816		1.25	1.05E+07	0.698		-0.782	
1.00						1.00					

Another parameter to investigate is the VG_1 angle respect to the top cap surface. For reducing computational times, such optimization has been performed using the coarse mesh (base size equal to 2.0 m). Assuming that positive angles are when the flat plate rotates towards lateral closing plates, from the data in Table 20 it's easy to identify that the angle of -10° assures highest improved efficiency (lift-to-drag ratio) at $\theta = 0^\circ$; when $\theta = 45^\circ$, changing the VG_1 angle produces efficiency variations no more than 2% from the angle of maximum efficiency. Hence, the angle of -10° has been chosen as the design angle of the VG_1 vortex generator.

In Table 20 the efficiency increments with respect to the VG_1 angle of maximum efficiency (ΔE_{\max}) and with the Frame_#3 clean configuration (ΔE_{clean}) are also presented. The Figure 47 represents the curves obtained with the values in Table 20.

Table 20 – VG_1 angle effects on lift-to-drag ratio

VG_angle [deg]	C_D (@0°)	C_L (@0°)	E (@0°)	(ΔE_{\max}) [%]	$(\Delta E_{\text{clean}})$ [%]	VG_angle [deg]	C_D (@45°)	C_L (@45°)	E (@45°)	(ΔE_{\max}) [%]	$(\Delta E_{\text{clean}})$ [%]
5.0	0.596	-0.867	-1.455	-2.10%	8.40%	5.0	0.681	-0.841	-1.235	-1.96%	5.59%
2.5	0.591	-0.859	-1.453	-2.18%	8.31%	2.5	0.672	-0.842	-1.253	-0.53%	7.13%
0.0	0.597	-0.834	-1.397	-5.98%	4.10%	0.0	0.675	-0.801	-1.187	-5.79%	1.46%
-2.5	0.594	-0.861	-1.449	-2.45%	8.01%	-2.5	0.674	-0.849	-1.260	0.00%	7.70%
-5.0	0.600	-0.870	-1.450	-2.42%	8.05%	-5.0	0.682	-0.851	-1.248	-0.94%	6.69%
-7.5	0.602	-0.888	-1.475	-0.73%	9.92%	-7.5	0.686	-0.854	-1.245	-1.17%	6.44%
-10.0	0.603	-0.896	-1.486	0.00%	10.73%	-10.0	0.686	-0.850	-1.239	-1.63%	5.94%
-12.5	0.604	-0.888	-1.470	-1.06%	9.56%	-12.5	0.688	-0.856	-1.244	-1.23%	6.38%
-15.0	0.605	-0.891	-1.473	-0.89%	9.74%	-15.0	0.688	-0.846	-1.230	-2.38%	5.13%

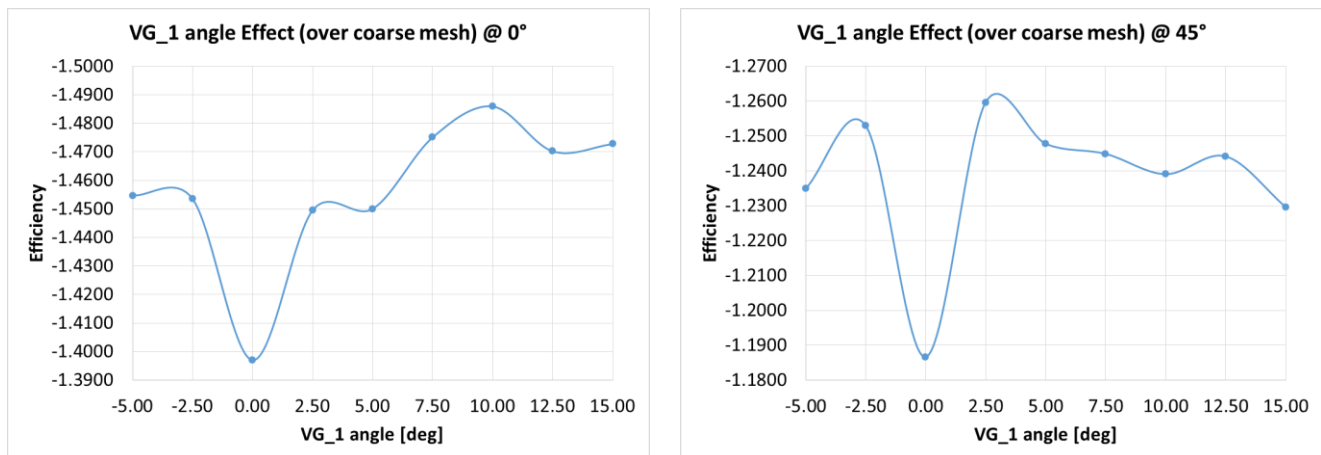
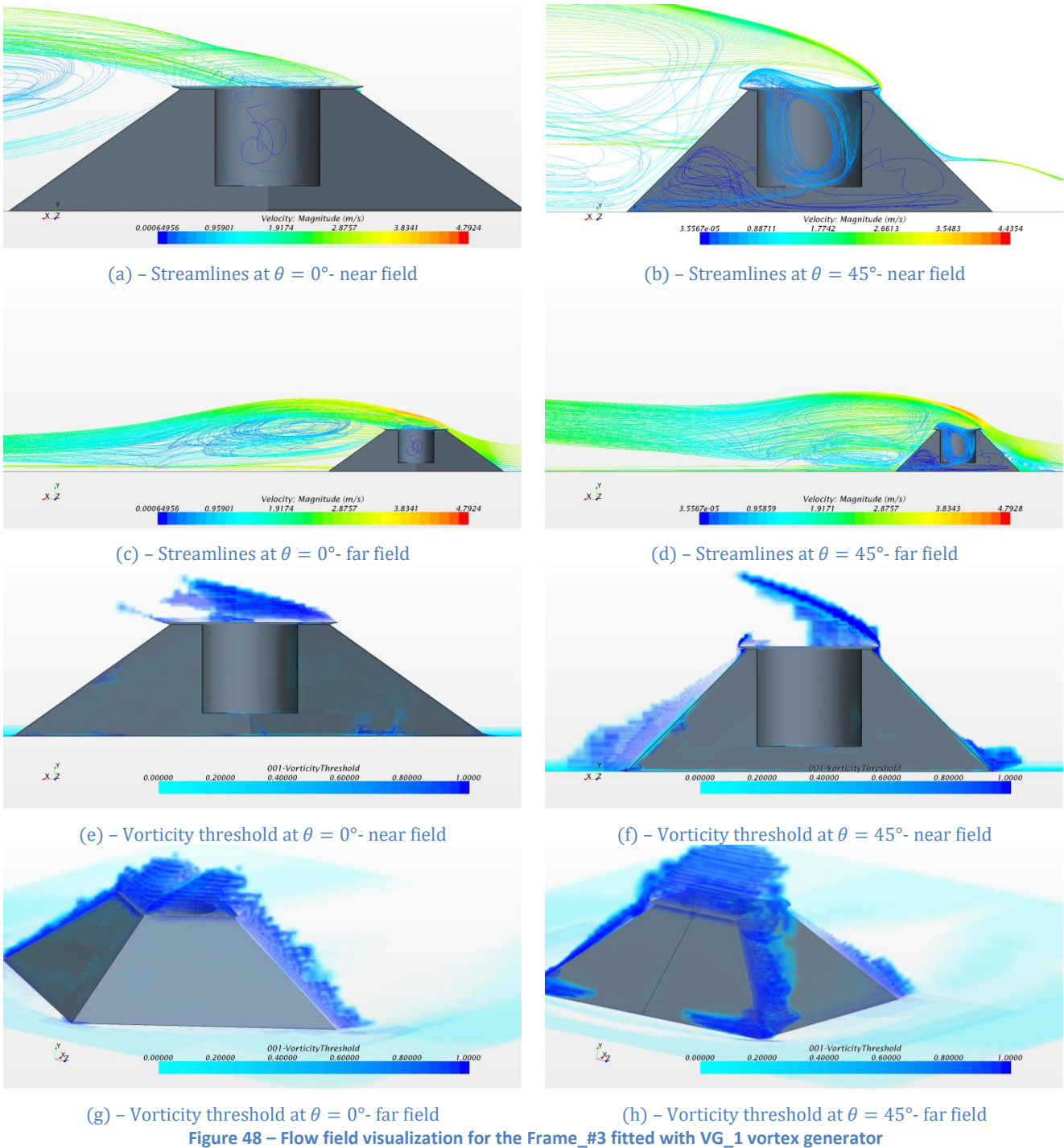


Figure 47 – VG_1 angle effects on lift-to-drag ratio

In terms of flow field distribution, the use of VG_1 vortex generator increases the vertical separation between the sensor head and the flow passing over the top cap (see Figure 48 – (a), Figure 48 – (b)) and, in turns, allows weaker flow inside the bucket. Moreover, the wake behind the frame seems to be pushed slightly far back, indicating the frame could be less affected by the wake induced vibrations (see Figure 48 – (c), Figure 48 – (d)). Finally, the vorticity threshold visualization indicates that turbulence near the sensor (inside the bucket) is reduced, achieving also the objective of turbulence reduction.



The VG_2 and VG_3 vortex generators have the same shape, being different for dimensions and position. Their base shape is an equilateral triangle whose length is a design parameter: for the VG_2 such length is 0.08 m, whereas it is 0.10 m for VG_3. These vortex generators are extruded in order to generate a pyramidal shape. They can be placed on the outside closing plate, using a parametrical distance from the top cap edge: in the VG_2, such distance is 0.05 m, while it is 0.01 m for the VG_3. They have been tested in the same conditions of the VG_1 vortex generator.

Unfortunately, the VG_2 and VG_3 vortex generators don't work well as expected. Comparing the flow fields in Figure 49 and in Figure 50 with the ones relative to the VG_1 vortex generator (Figure 48), it's evident that such shapes don't assure the same sensor protection and allow more energetic flow into the bucket. Furthermore, the VG_3 configuration has shown a big flow direction sensitivity, improving frame efficiency

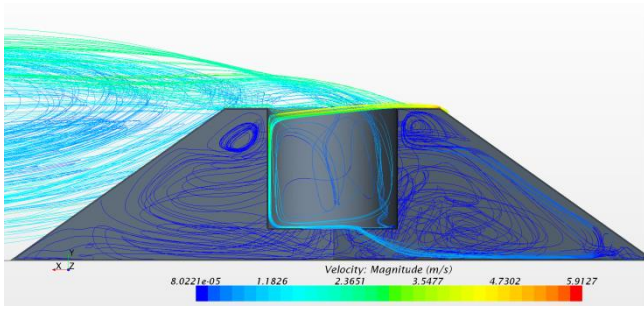
($E=-1.508$) at $\theta = 0^\circ$ but being disadvantageous ($E=-1.095$) at $\theta = 45^\circ$. Conversely, despite the more geometrical complexity, the VG_2 vortex generator performance are very close to the VG_1 ones.

Table 21 – Frame_#3 with VG_2 vortex generator mesh independence study data

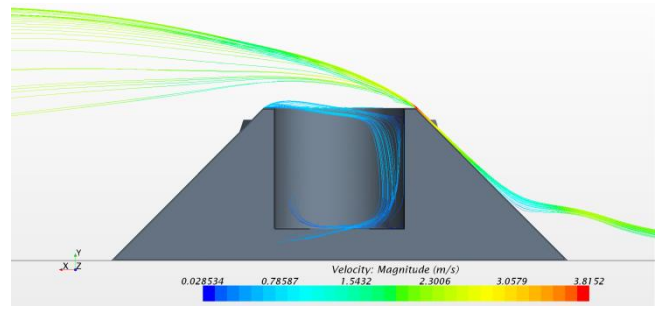
BaseSize [m]	CellsNumber	C_D (@0°)	ΔC_D	C_L (@0°)	ΔC_L	BaseSize [m]	CellsNumber	C_D (@45°)	ΔC_D	C_L (@45°)	ΔC_L
2.00		0.540	0.93%	-0.815	9.54%	2.00		0.549	1.48%	-0.831	1.84%
1.50		0.538	0.56%	-0.783	5.24%	1.50		0.543	0.37%	-0.863	5.76%
1.25		0.537	0.37%	-0.760	2.15%	1.25		0.545	0.74%	-0.818	0.25%
1.00		0.535		-0.744		1.00		0.541		-0.816	

Table 22 – Frame_#3 with VG_3 vortex generator mesh independence study data

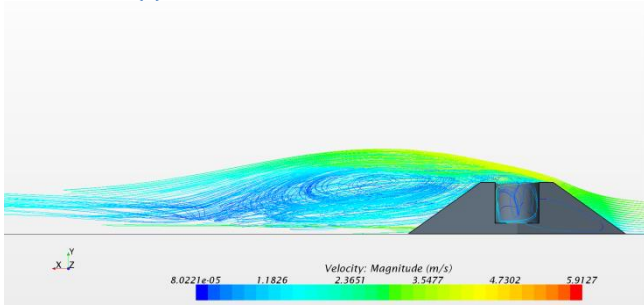
BaseSize [m]	CellsNumber	C_D (@0°)	ΔC_D	C_L (@0°)	ΔC_L	BaseSize [m]	CellsNumber	C_D (@45°)	ΔC_D	C_L (@45°)	ΔC_L
2.00		0.604	-2.27%	-0.719	4.05%	2.00		0.619	-1.75%	-0.704	2.03%
1.50		0.608	-1.62%	-0.664	-3.91%	1.50		0.619	-1.75%	-0.655	-5.07%
1.25		0.613	-0.81%	-0.692	0.14%	1.25		0.627	-0.48%	-0.689	-0.14%
1.00		0.618		-0.691		1.00		0.630		-0.690	



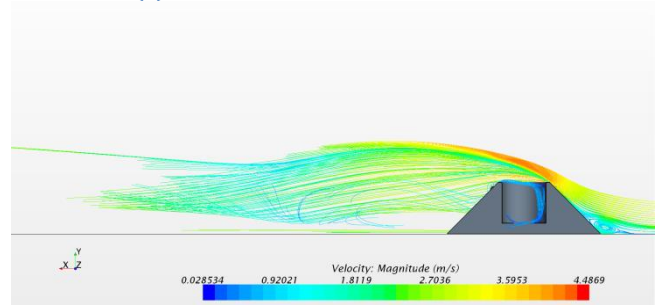
(a) - Streamlines at $\theta = 0^\circ$ - near field



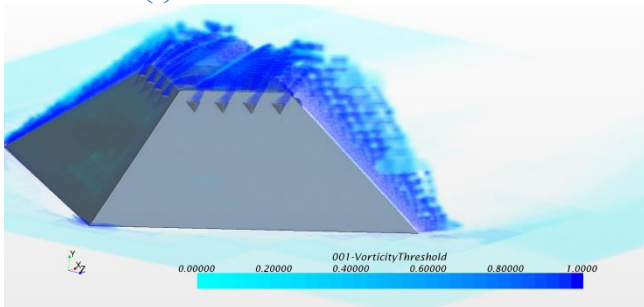
(b) - Streamlines at $\theta = 45^\circ$ - near field



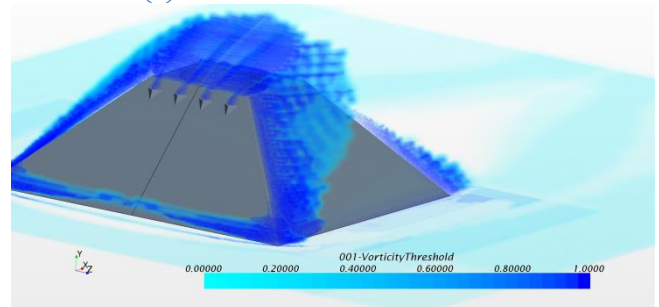
(c) - Streamlines at $\theta = 0^\circ$ - far field



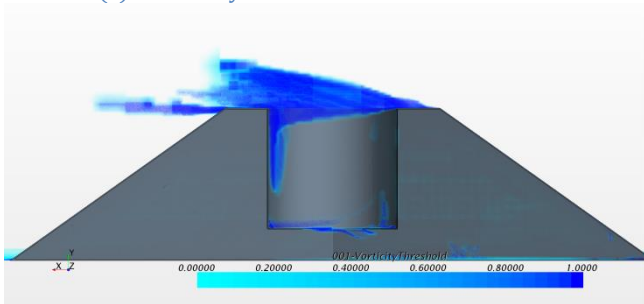
(d) - Streamlines at $\theta = 45^\circ$ - far field



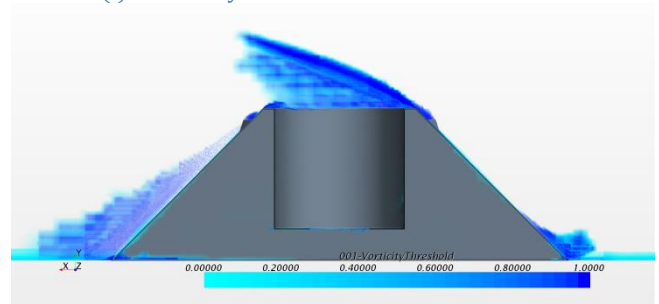
(e) - Vorticity threshold at $\theta = 0^\circ$ - near field



(f) - Vorticity threshold at $\theta = 45^\circ$ - near field

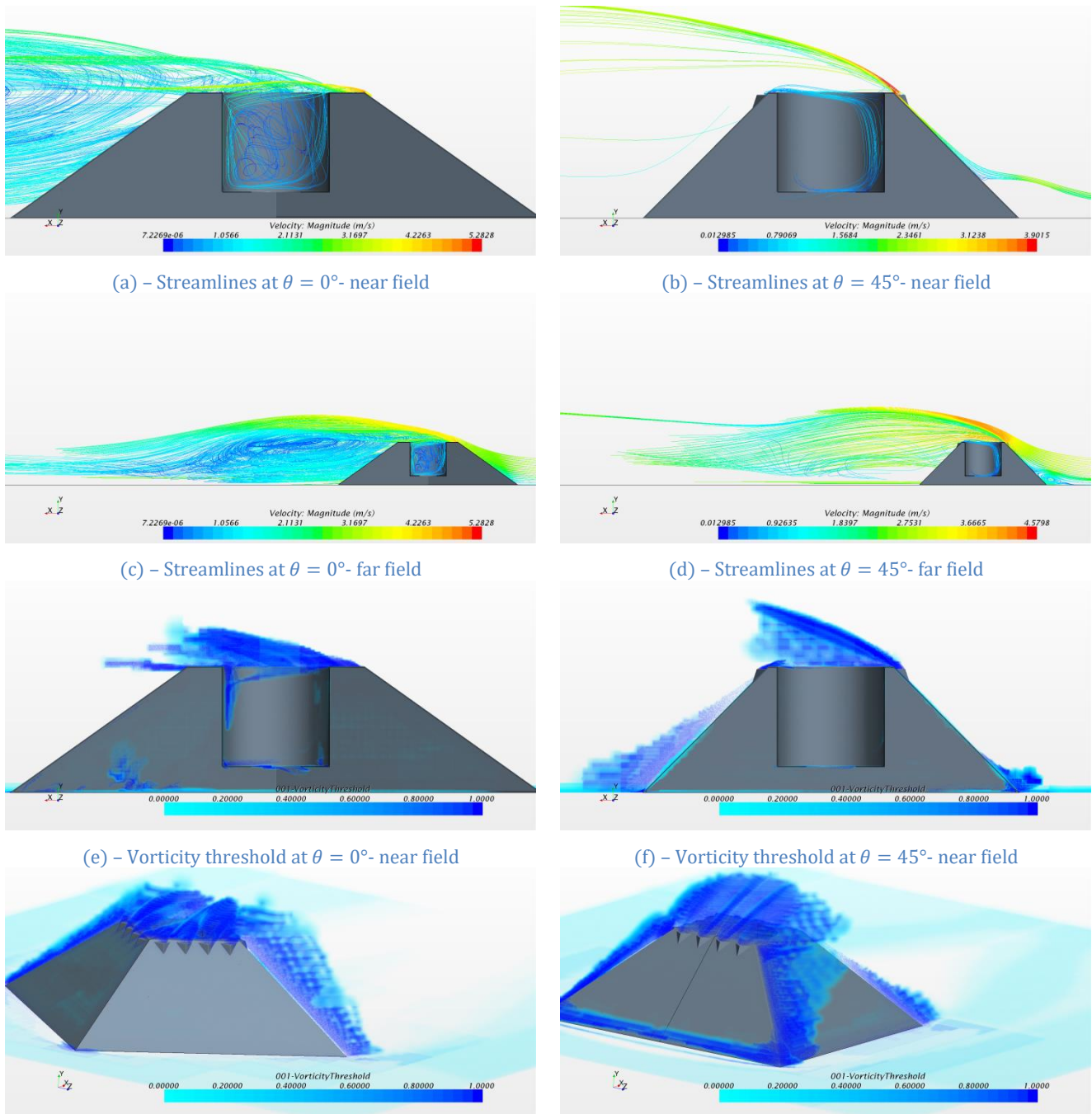


(g) - Vorticity threshold at $\theta = 0^\circ$ - far field



(h) - Vorticity threshold at $\theta = 45^\circ$ - far field

Figure 49 – Flow field visualization for the Frame_#3 fitted with VG_2 vortex generator



(a) – Streamlines at $\theta = 0^\circ$ - near field

(b) – Streamlines at $\theta = 45^\circ$ - near field

(c) – Streamlines at $\theta = 0^\circ$ - far field

(d) – Streamlines at $\theta = 45^\circ$ - far field

(e) – Vorticity threshold at $\theta = 0^\circ$ - near field

(f) – Vorticity threshold at $\theta = 45^\circ$ - near field

(g) – Vorticity threshold at $\theta = 0^\circ$ - far field

(h) – Vorticity threshold at $\theta = 45^\circ$ - far field

Figure 50 – Flow field visualization for the Frame_#3 fitted with VG_3 vortex generator

Table 23 – Ballast evaluation using the velocity from the 10th power law on the frame top cap

$$\text{Friction} = \mu * (\text{Weight} - \text{Lift} + \text{AddedMass}) [\text{N}] > \text{Drag}$$

Friction coefficient (Sandstone) $\mu = 0.340$	Drag [N]	Lift [N]	Frontal Area [m ²]	AddedMass [N]	AddedMass [kg]	Flow angle [°]	Total Weight [kg]
Frame #0 (118 kg, V=2.70 m/s)	1158	622	0.182	2573	262	0	411
	1158	801	0.210	2752	280	30	429
Frame #1 (188 kg, V=2.70 m/s)	2154	-1753	0.435	2444	249	0	467
	2463	-1878	0.497	3227	329	30	547
Frame #2 (241 kg, V=2.70 m/s)	2658	-3376	0.659	1776	181	0	453
	2257	-2358	0.467	1614	165	45	436
Frame #3 (199 kg, V=2.57 m/s)	1277	-1714	0.357	-206	-21	0	229
	1046	-1223	0.253	-396	-40	45	229
Frame #3 w/ VG_1 (199 kg, V=2.57 m/s)	1391	-1927	0.357	-85	-9	0	229
	1165	-1305	0.253	-128	-13	45	229

In Table 23 the ballast amounts for all the frame configurations analysed so far are compared. It's worth noting that, even though the Frame_#3 with the VG_1 vortex generator seems to need more ballast than the clean configuration, such figure is however negative, meaning that, in principle, no ballast is needed. Moreover, it has been noticed that the vortex generator effect becomes more important when the velocity increases, assuring a certain safety margin whenever the flow speed results more challenging. For safety reason, it's recommend to deploy such frame with, at least, 10% more weight than required (having a total frame weight of 252 kg).

Frame_#4: final configuration of the optimized frame

In this section, some features of the final frame configuration submitted for manufacturing are explained. The Frame_#4 differs marginally from Frame_#3 and, then, some of the final CFD simulations presented here account for the ADCP sensor as well. In fact, when the ADCP sensor is installed into the bucket, it influences the flow over the bucket area and, also, being exposed to the flow, it transfers fluid forces on the frame. In all the CFD simulations shown so far, the ADCP sensor isn't installed into the bucket.

Furthermore, the final Frame_#4 configuration has to be fitted with, at least, three supporting feet to assure the correct frame stability on very rough seabed. Due to this clearance underneath the sensor frame, some fluid is allowed to flow from the bottom to the top, inside the frame, and this, in turn, can affect its aerodynamic performance. Hence, there should be some flow modifications to investigate.

Another important aspect to investigate is whether the presence of the VG_1 vortex generator can cause ADCP oscillations. To do so, the ADCP has been included into the CFD computational domain, into a simulated gimbal with two degrees of freedom (DOF): the pitch, around the x-axis, and the roll, around the z-axis. When the ADCP is exposed to the flow, the fluid forces on the sensor cause it to rotate around the gimbal axis and, if the flow forces are almost steady, it assumes an equilibrium position with steady pitch and roll angles; most likely, the sensor would oscillate around such equilibrium position and the objective is to estimate such oscillations for comparison with previous deployment.

The Figure 51 presents the final Frame_#4 modelled into the CFD software, including also the ADCP Signature 500 sensor, used for evaluating sensor oscillations. The sensor is normally exposed to two counteracting forces, the resultant fluid force (cyan arrow) and the stabilizing gravity force (yellow arrow). Due to the offset between the application points of those forces, they produce counteracting moments, with the gravity moments that reduces the fluid induced oscillations. Whereas the fluid force magnitude is dependent on the fluid itself and its application point is on the gimbal supports, the gravity force and its application point are imposed by a stabilizing mass usually attached to the sensor (see Figure 52): such mass helps to align the sensor normally to the seabed and, in turn, reduce the sensor oscillations caused by the flow.

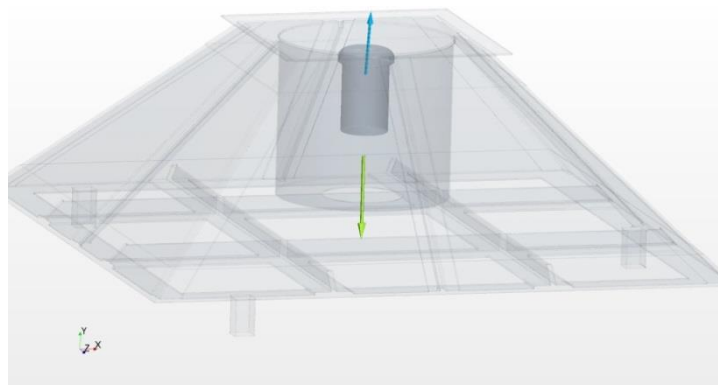


Figure 51 – Frame_#4 equipped with the Signature 500 sensor: CFD simulation screenshot with the indication of fluid force (cyan) and gravity force (yellow)

Using a mass of about 2.3 kg at 0.300 m from the sensor head, the resulting total sensor mass is about 3.5 kg and the centre of gravity (CoG) is placed at 0.210 m below the gimbal attachment points. Such figures have been used to setup the Star-CCM+ DFBI model, which allow the computation of flow induced rotation and translation of a defined region. This kind of simulation requires the definition of two different regions which interacts through the Overset grid algorithm, exchanging flow field information between two overlapped computational grid (background and overset meshes).

Moreover, as can be seen from Figure 51, the Frame_#4 used in those simulations isn't simplified, keeping most of the expected real frame features. This choice has caused more expensive and longer computational time for obtaining CFD results, even using the coarse mesh setup. The simulations are divided in two distinct phases: the first one, from 0 s to 9 s, needed to allow the flow field to develop and reach the quasi-steady condition (the ADCP sensor is not allowed to move during this time); the second one, from 9 s to 45 s, in which the sensor is free to move and exhibit its own dynamics. The mesh counts slightly less than 40M cells and it takes about 14 days to complete 45 s of simulation time, using 128 CPUs.



Figure 52 – Signature 500 sensor with added mass for increased stability

In Figure 53 it is presented the recorded sensor roll and pitch angles during a real deployment near Taransay, an island in the Outer Hebrides (Scotland, UK): what is interesting from that is the magnitude of such angles ($1^\circ \div 2^\circ$).

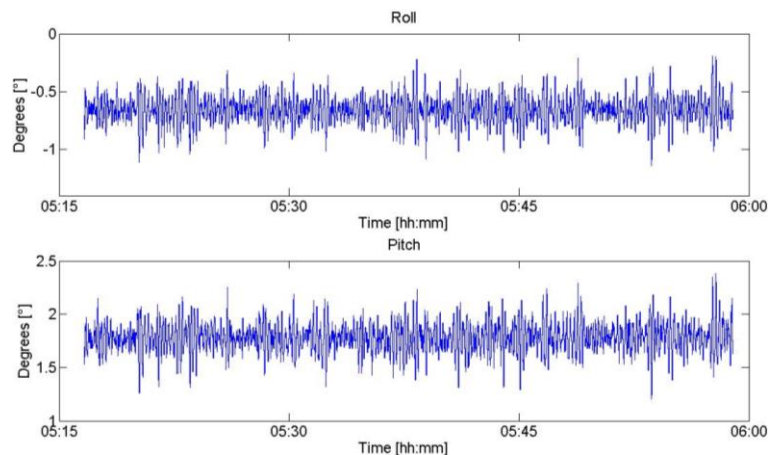
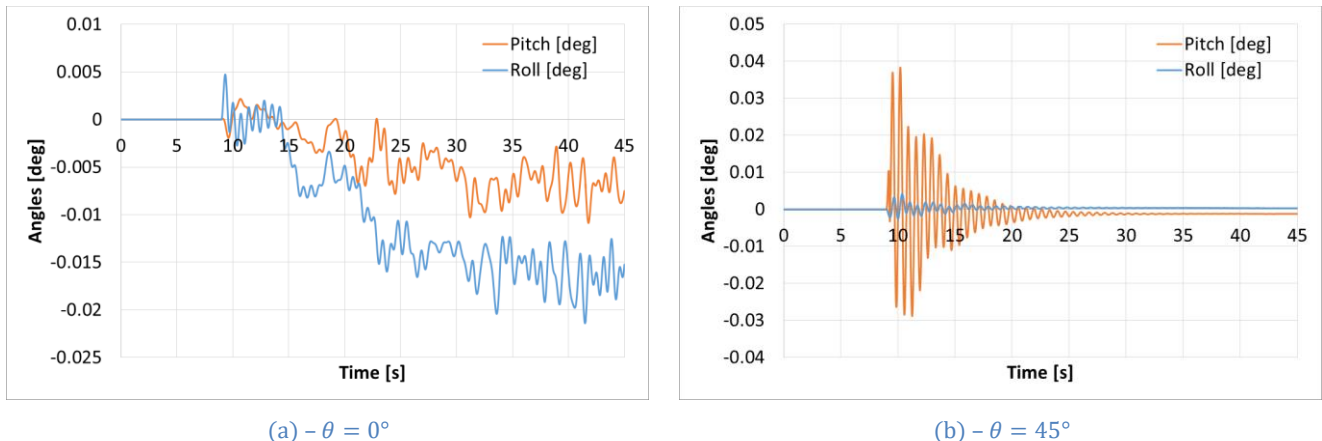


Figure 53 – Signature 500 sensor with added mass for increased stability

In order to understand how the sensor can affect the whole frame aerodynamic performance, a run using the Frame_#3, equipped with the VG_1 vortex generator and the moving ADCP sensor, has been completed. The roll and pitch angles time histories are in Figure 54, for both the flow directions of $\theta = 0^\circ$ and $\theta = 45^\circ$. The interesting fact is that, in both situations, the angles amplitudes are lesser than the ones in Figure 53. In terms of coefficients, in Table 24 is presented the comparison between the two cases (without and with the Signature 500 sensor), on the same mesh resolution. Due to the presence of the ADCP sensor, the coefficients are higher in all the flow conditions. In any case, such analysed situation is quite far from reality as

the flow direction could easily be with any other angle between $\theta = 0^\circ$ and $\theta = 45^\circ$, that are symmetric flow conditions (in the light of this, the Figure 53 and Figure 54 have to be compared).



(a) - $\theta = 0^\circ$ (b) - $\theta = 45^\circ$
 Figure 54 – Signature 500 sensor pitch and roll angles, using the Frame_#3 with VG_1 vortex generator

Table 24 – Influence on aerodynamic force of sensor presence (Frame_#3 with VG_1 vortex generator, coarse mesh)

	C_D (@0°)	ΔC_D	C_L (@0°)	ΔC_L	C_D (@45°)	ΔC_D	C_L (@45°)	ΔC_L
Frame_#3 w/ VG_1	0.597		-0.834		0.675		-0.801	
Frame_#3 w/ VG_1 and Signature 500	0.628		-1.010		0.719		-0.873	
		+5.19%		+21.1%		+6.52%		+8.99%

Similar runs have been performed using the Frame_#4: such frame configuration is similar to Frame_#3 except for some clearance underneath, due to the presence of some feet. Being the frame height increased, velocity at the top cap is 2.62 m/s, whereas the reference surfaces for $\theta = 0^\circ$ and $\theta = 45^\circ$ can be considered unchanged: indeed, the feet frontal area is small compared with the total frontal area. Thus, aerodynamic results of Frame_#4 can be compared with the ones of Frame_#3: Table 25 shows such comparison. Due to the open bottom and the possibility for the water to flow inside the frame, the Frame_#4 downforce is considerably reduced whereas the drag is almost unchanged. Using those data is clear that the needed ballast will be larger for the Frame_#4 than the Frame_#3, as shown in Table 26. Anyway, as such results consider a completely flat seabed, which allow much stronger stationary flow below the frame than the one experienced during real deployment, it has to be considered that seabed roughness can both close the frame bottom and reduce flow speed underneath, as well.

Table 25 – Aerodynamic forces for the Frame_#4 with VG_1 vortex generator (coarse mesh)

	C_D (@0°)	C_L (@0°)	C_D (@45°)	C_L (@45°)
Frame_#3 w/ VG_1	0.597	-0.834	0.675	-0.801
Frame_#3 w/ VG_1 and Signature 500	0.628	-1.010	0.719	-0.873
Frame_#4 w/ VG_1 and Signature 500	0.645	-0.385	0.738	-0.313

Table 26 – Ballast evaluation using the velocity from the 10th power law on the frame top cap

$$\text{Friction} = \mu * (\text{Weight} - \text{Lift} + \text{AddedMass}) \text{ [N]} > \text{Drag}$$

Friction coefficient (Sandstone) $\mu = 0.340$	Drag [N]	Lift [N]	Frontal Area [m ²]	AddedMass [N]	AddedMass [kg]	Flow angle [°]	Total Weight [kg]
Frame_#3 w/ VG_1 (199 kg, V=2.57 m/s)	1391	-1927	0.357	-85	-9	0	229
	1165	-1305	0.253	-128	-13	45	229
Frame_#4 w/ VG_1 (215 kg, V=2.62 m/s)	1577	-941	0.357	1293	132	0	361
	1278	-542	0.253	812	83	45	312

In terms of sensor pitch and roll angles (see Figure 55) it's clear that, due to the water flowing from bottom to top inside the sensor frame, more sensor oscillations are recorded. Those oscillations are smaller and comparable with the Frame_#3 case at $\theta = 0^\circ$, whereas are bigger than those when $\theta = 45^\circ$, reaching values slightly lower than those reported in Figure 53. By the way, it's worth noting that the data in Figure 55 have been obtained using the velocity profile in Figure 40, based on a surface velocity of 3.6 m/s and such velocity is possibly higher than the one measured during that deployment. In fact, while the velocity expected at the sensor frame top cap is 2.62 m/s, the one measured at Taransay is around 1.5 m/s, with higher peaks during surge phases.

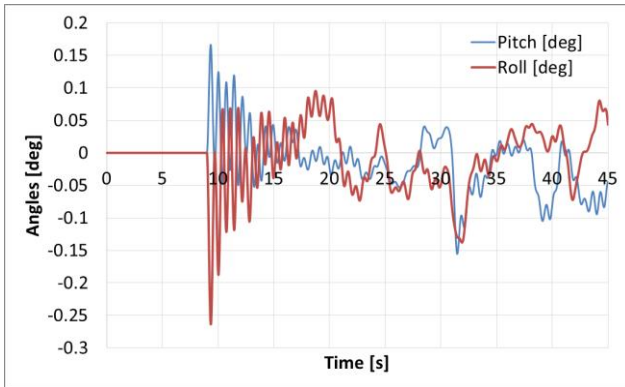
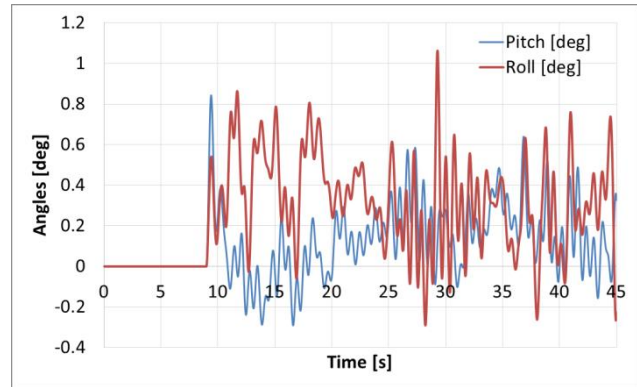
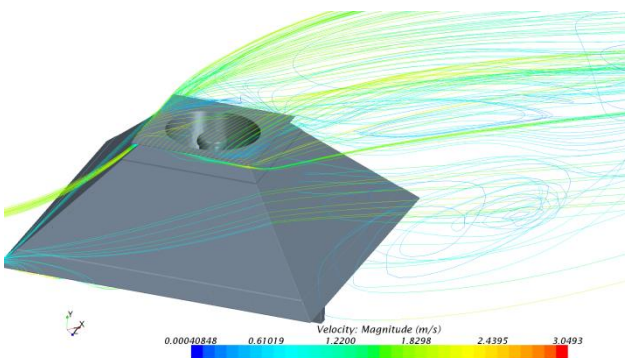
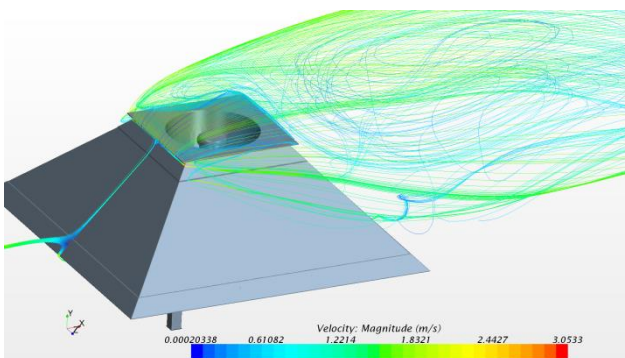
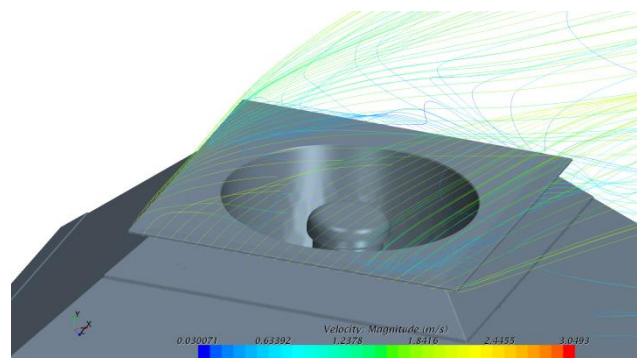
(a) – $\theta = 0^\circ$ (b) – $\theta = 45^\circ$

Figure 55 – Signature 500 sensor pitch and roll angles, using the Frame_#4 with VG_1 vortex generator

Figure 56 – Some streamlines around the Frame_#4 with VG_1 vortex generator at $\theta = 0^\circ$ Figure 57 – Some streamlines around the Frame_#4 with VG_1 vortex generator at $\theta = 45^\circ$

To obtain results comparable with one of the real deployed situation, some calculations have been performed taking into account a modified velocity inlet profile: the idea has been to obtain a velocity inlet profile as much as possible comparable with the ones measured near Westray Firth, Orkney Island (Scotland, UK) reported in Figure 58. The measured data have been compared with the 10th power law and a modified power law in Figure 58, showing how the 10th power law overestimates flow velocity at very low water depth.

Such difference is of key importance as seabed frames are usually deployed at water depth where the 10th power law overestimates flow velocity. To obtain the modified velocity power law, the coefficients in (8) have been modified as shown in (9), using $V_s=1.80$ m/s and $H=58$ m.

$$V_D = 1.1 * V_s \qquad V(y) = V_D * \left(\frac{y}{H}\right)^{0.33} \qquad (9)$$

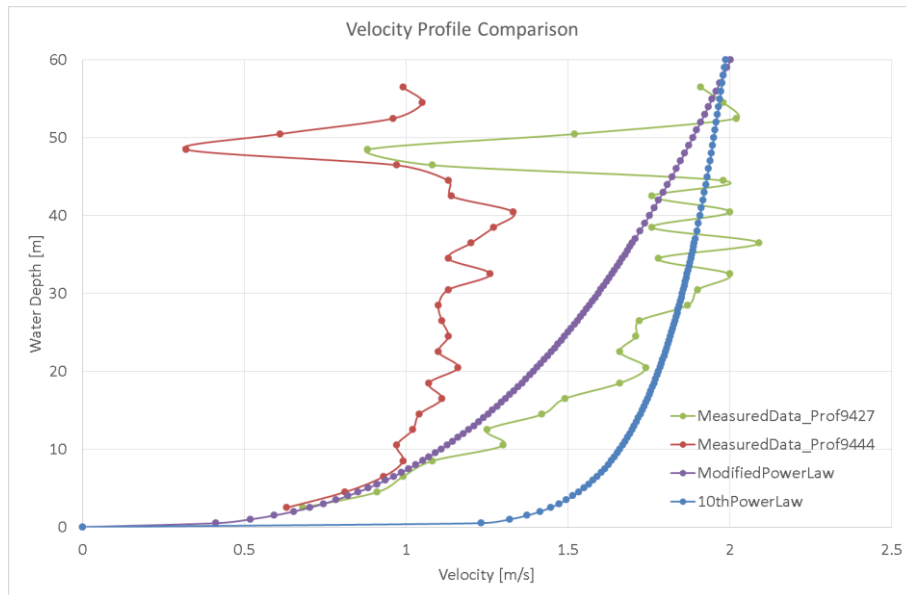


Figure 58 – Modified velocity inlet power law compared with measured data and 10th power law

Being the sensor head at 0.6 m from the seabed, the expected velocity at the top cap is 0.44 m/s, incredibly low as compared with velocities previously used. Because of this, flow structures around the frame are expected to be different, being the non-dimensional Reynolds number decreased from about $6E+06$ to about $7E+05$. Such flow behaviour affects also the amount of aerodynamic force on the frame: in particular, the data obtained from such CFD simulations are in Table 27, along with a new estimation of ballast. The Table 27 shows that no ballast is required with that low velocity value, as the frame weight is able to generate the right amount of friction needed to hold itself on the seabed.

Table 27 – Ballast evaluation using the velocity from the 10th power law on the frame top cap

$$\text{Friction} = \mu * (\text{Weight} - \text{Lift} + \text{AddedMass}) \text{ [N]} > \text{Drag}$$

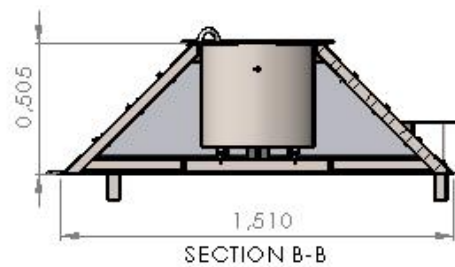
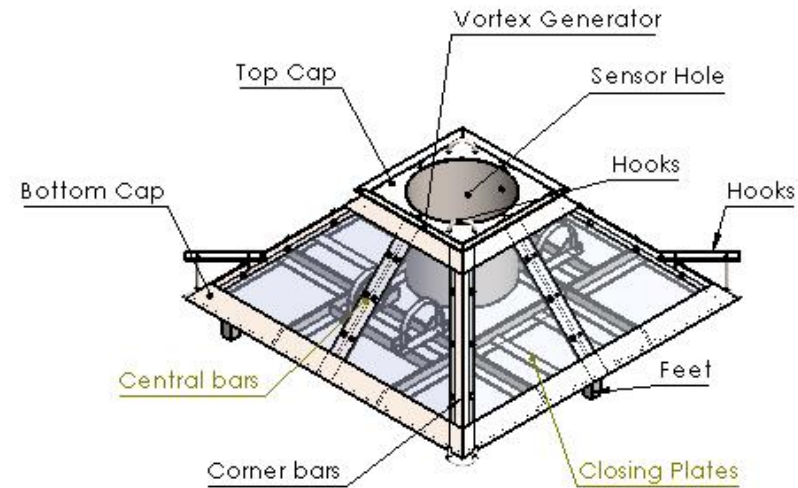
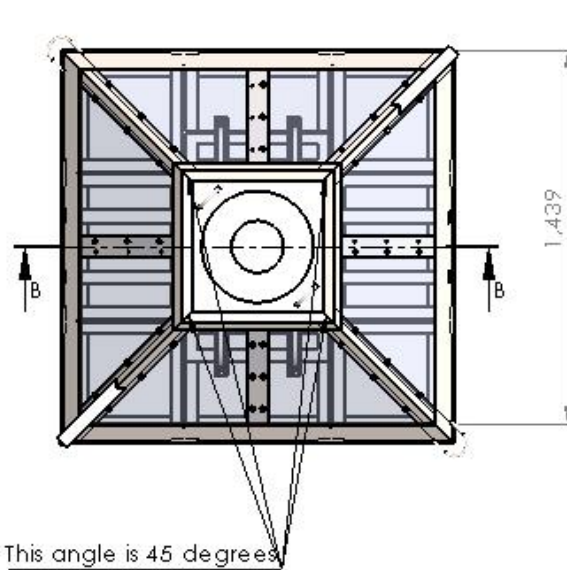
Friction coefficient (Sandstone) $\mu = 0.340$	Drag [N]	Lift [N]	Frontal Area [m ²]	AddedMass [N]	AddedMass [kg]	Flow angle [°]	Total Weight [kg]
Frame_#4 w/ VG_1 (215 kg, V=2.62 m/s)	1577	-941	0.357	1293	132	0	361
	1278	-542	0.253	812	83	45	312
Frame_#4 w/ VG_1 (215 kg, V=0.44 m/s)	38	211	0.357	-2081	-212	0	245
	31	231	0.253	-2081	-212	45	245

Manufacturing process of the Frame_#4

In this section, the technical drawings and some pictures of the manufacturing process for the realization of the Frame_#4 are included. As indicated in the following drawings, all the linear measurements are in meters while the angular ones are in degrees. Based on the CAD model and the chosen material (Stainless Steel 316 – ref. code: AISI 316 (SS)), an estimation of the total weight and parts weight is provided as well.

As can be seen from the technical drawings and the CAD renderings, the Frame_#4 suits several additional parts specifically designed for deployment purposes, like the hooks on the top cap, for attaching the special mark buoy, and the recovery hooks, for recovery the sensor frame using a remotely operated underwater vehicle (ROV).

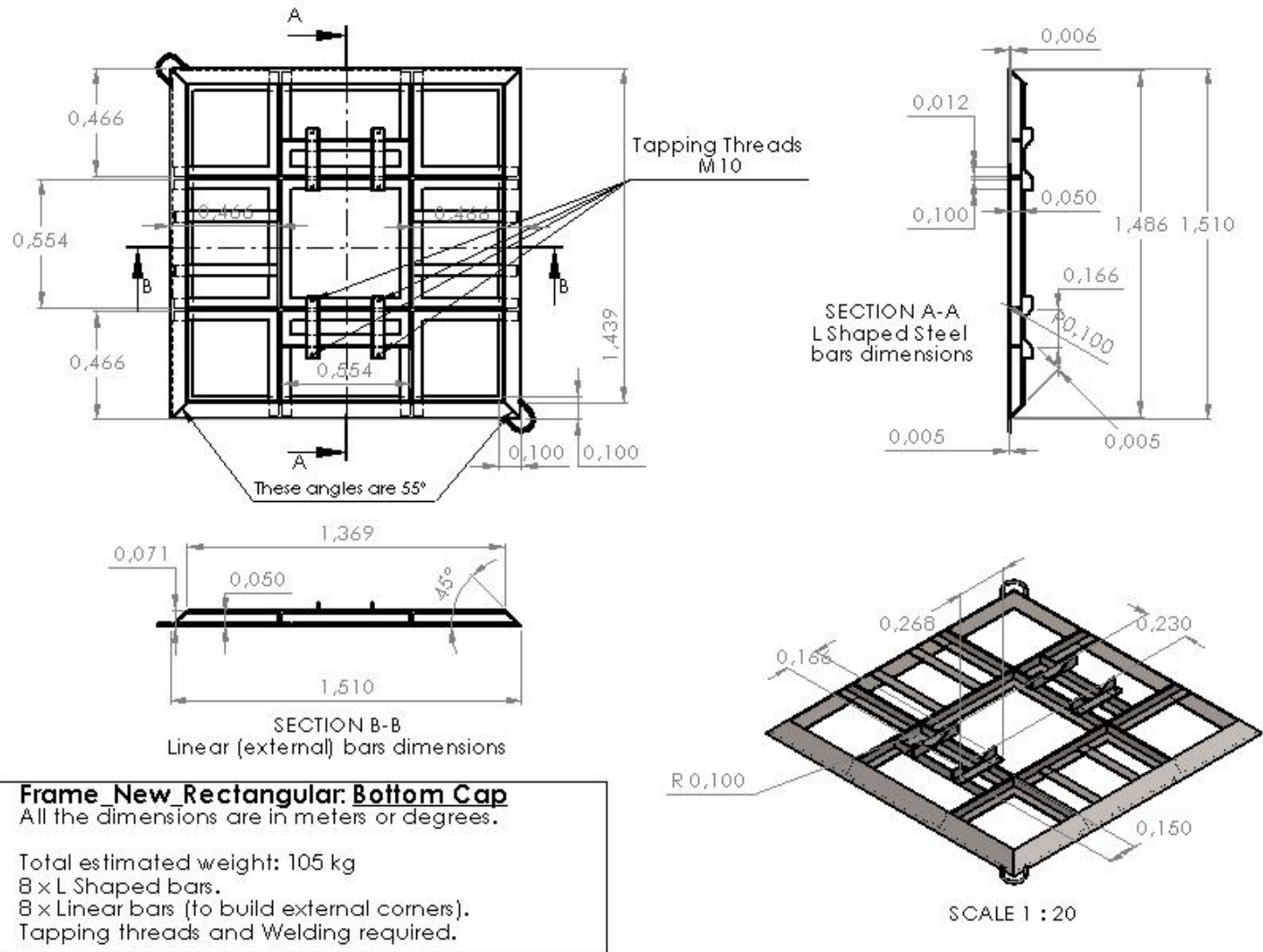
In terms of production, considering the material supply and all the manufacturing processes involved, the Frame_#4 has been finished in about two months.

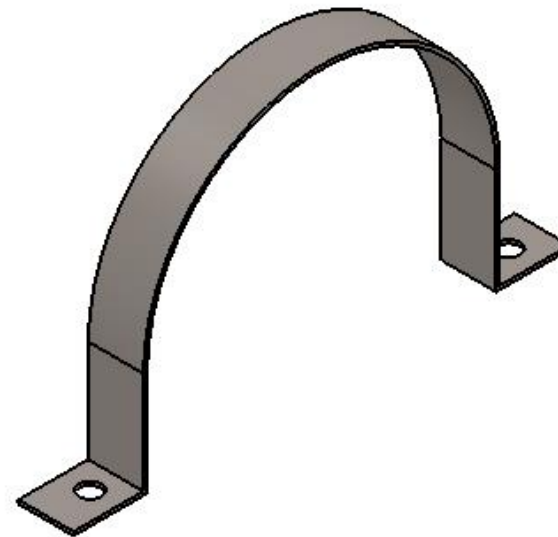
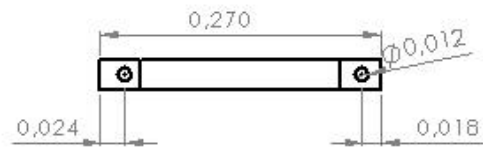
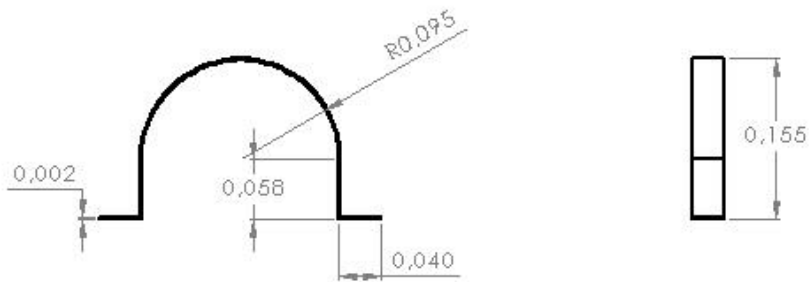


Frame New Rectangular

All the dimensions are in meters or degrees.

- Total estimated weight: 215 kg (w/o ballast)
- 4 x Corner bars.
- 4 x Linear Central bars.
- 1 x Bottom Cap.
- 1 x Top Cap.
- 4 x Trapeziodal Plates ($B=1.295$, $b=0.572$, $H=0.513$, 11.425 kg/each)
- 3 x Feet.
- 1 x Vortex Generator.

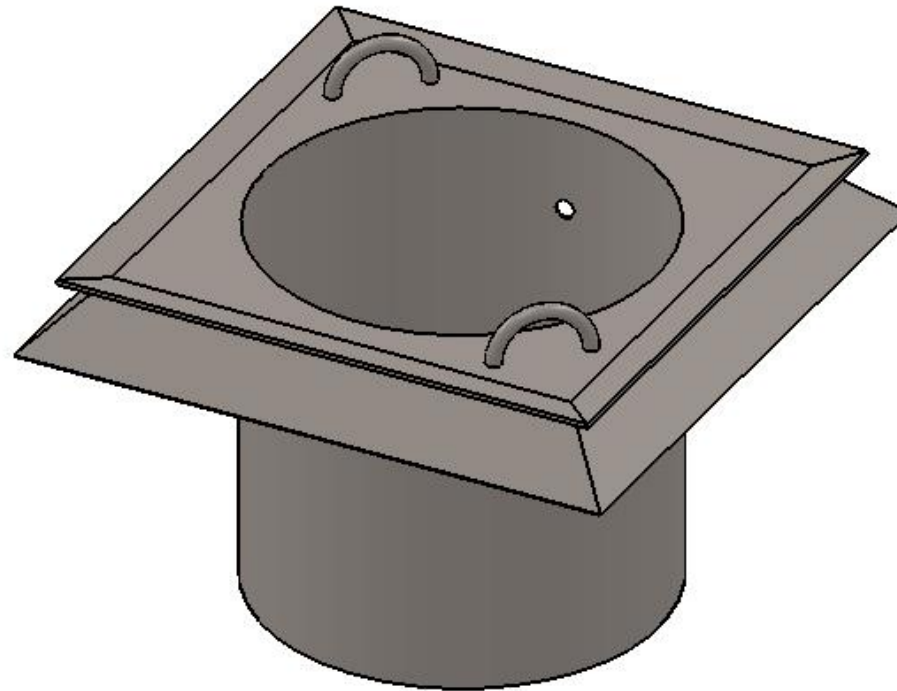
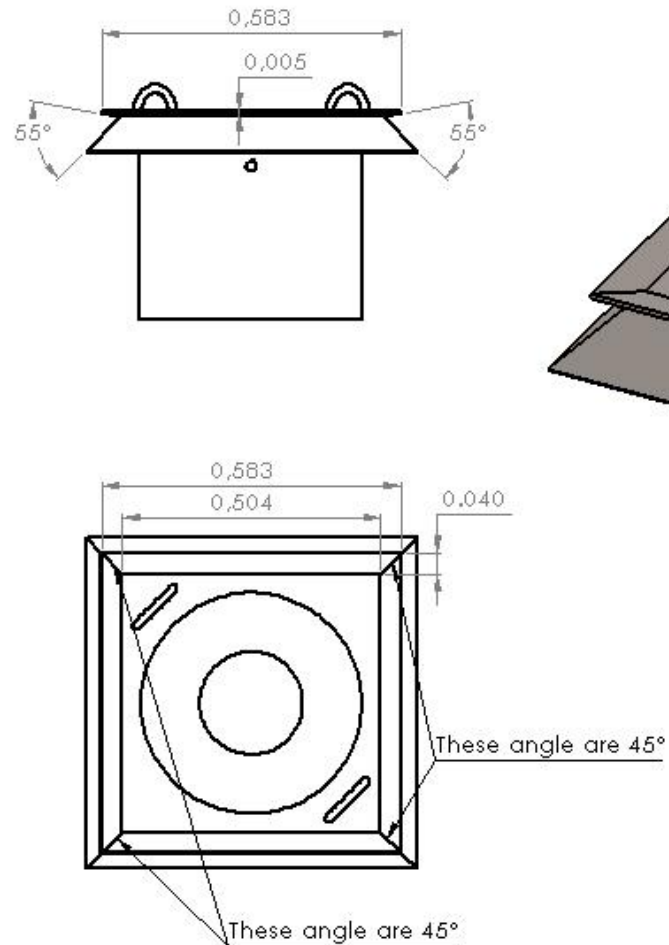




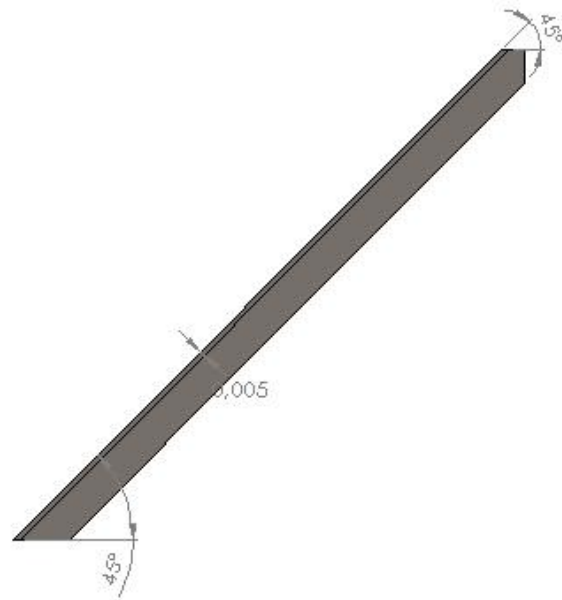
SCALA 1 : 2

Frame_New_Rectangular: Bracket
All the dimensions are in meters or degrees.

Plate bending and Milling.



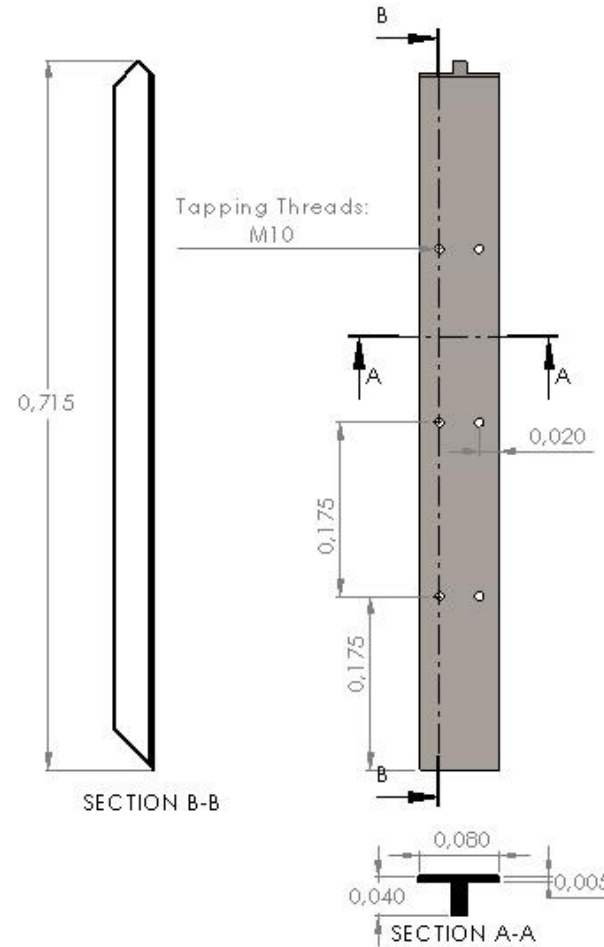
Frame_New_Rectangular: Vortex Generator
All the dimensions are in meters or degrees.
Plate bending and Milling.

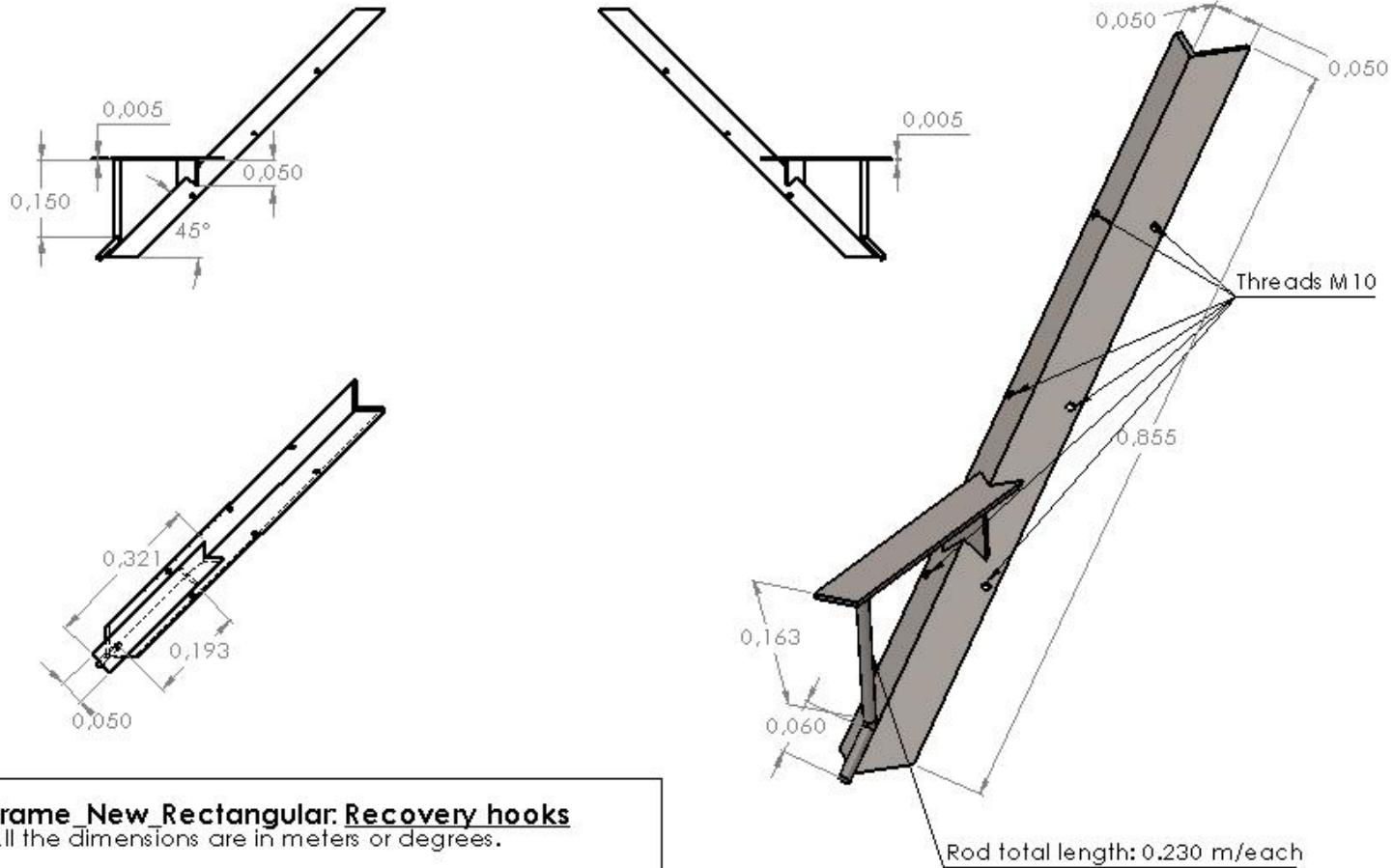


Frame_New_Rectangular: linear central bars

All the dimensions are in meters or degrees.

Total estimated weight: 4.93 kg (each)
 4 x linear bars (L=0.715, t=0.005).
 Milling and Tapping threads required.

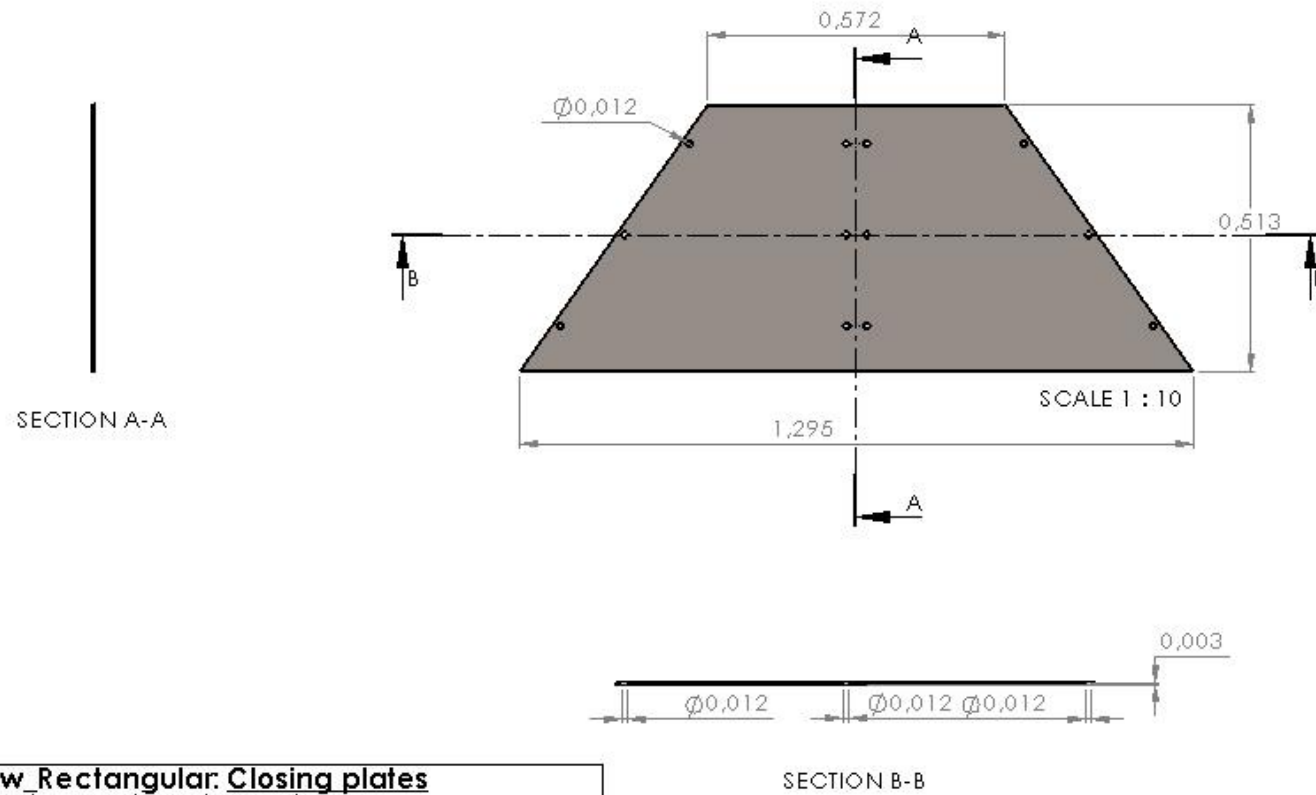




Frame_New Rectangular: Recovery hooks

All the dimensions are in meters or degrees.

Tube bending and Welding required.

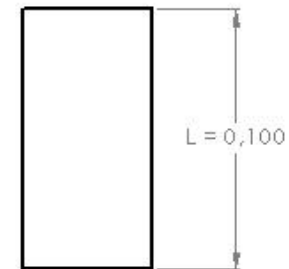
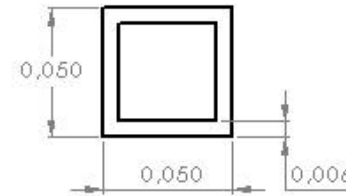
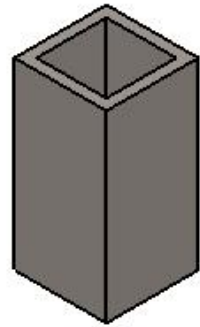


Frame_New Rectangular: Closing plates

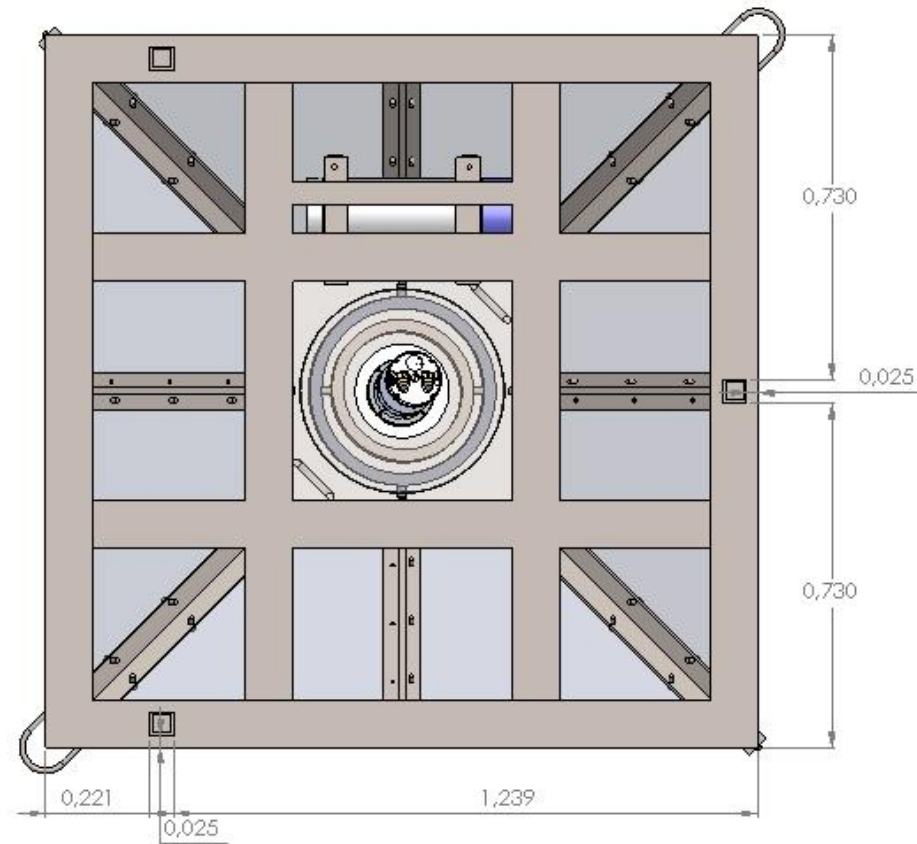
All the dimensions are in meters or degrees.

Total estimated weight: 11,425 kg
 4 x Trapezoidal plate($B=1,295$, $b=0,572$, $h=0,513$, $t=0,003$).

Milling and tapping threads required.



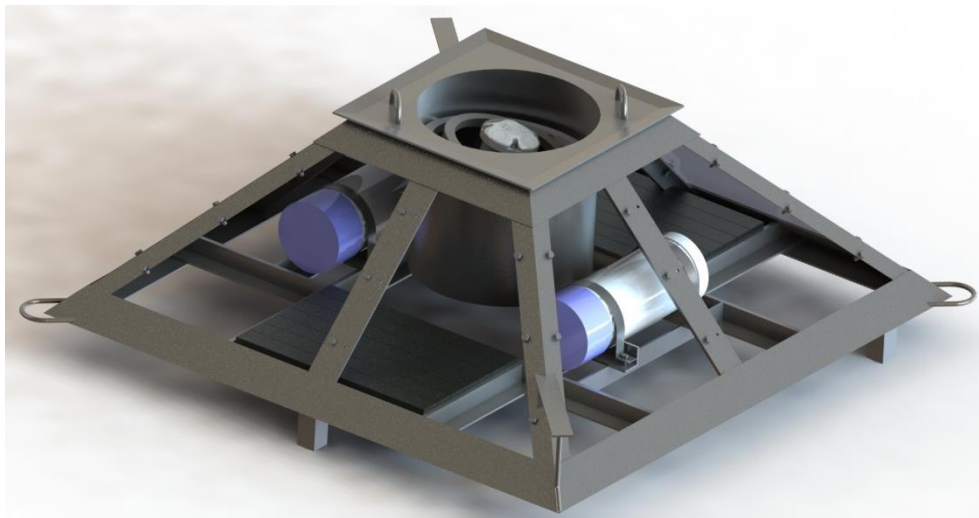
Frame New Rectangular: Feet (x3)
All the dimensions are in meters or degrees.
Total estimated weight: 0.85 kg (each).
6 x L Shaped bars (L = 0.100).
Welding required.

**Frame_New_Rectangular:Feet arrangement**

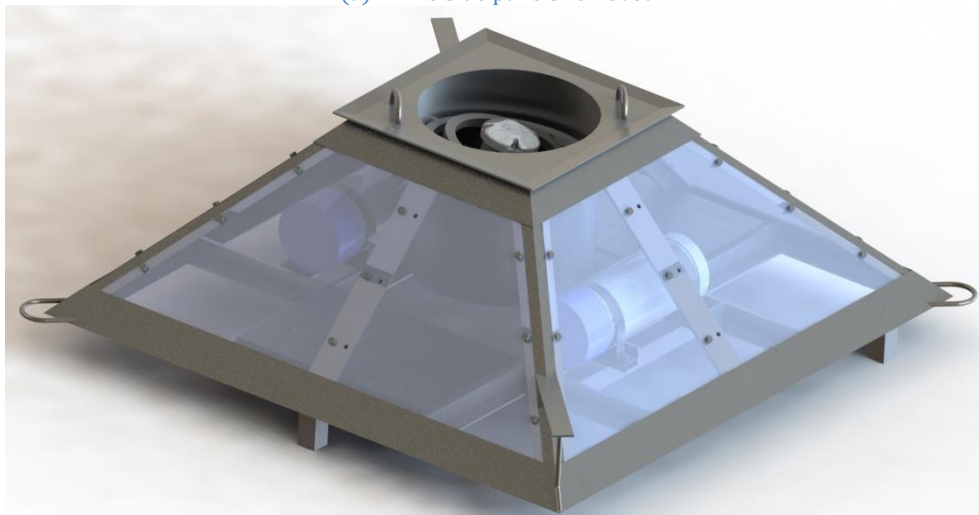
All the dimensions are in meters or degrees.

Welding required.

From the CAD renderings in Figure 59, it can be seen also the Frame_#4 fitted with a possible battery pack and a possible ADCP sensor (i.e., the Signature 500), mounted on a similar gimbal previously used during the deployment of the Frame_#0 and Frame_#1. The Figure 59 shows the open bottom and the three feet, disposed on an equilateral triangle, for increasing the frame stability: such consideration is important for deployment in very unsmooth and rocky areas, like the one around Scotland and the Western Isles. Furthermore, the presence of the three feet increase the seabed friction in other environment mainly characterized by the presence of sand, clay and mud, as they work like the shear keys on a deadweight anchor (see [9]). On the top cap, it can be seen also the presence of a simple vortex generator device, installed on the sensor frame to improve its aerodynamic performance and, in turn, reduce the frame generated turbulence over the sensor head: the vortex generator slightly displaces the flow vertically, moving up the eddies from the sensor head.



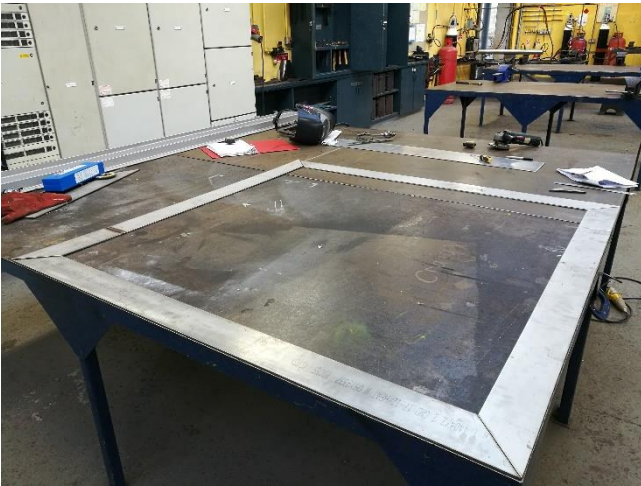
(a) - Two side panels removed



(b) - Completely assembled sensor frame

Figure 59 – Frame_#4 CAD model renderings

In the following pages are attached some of the pictures taken during the production phase of the Frame_#4 at the Lews Castle College UHI in Stornoway.



08/02/2017



08/02/2017



08/02/2017



09/02/2017



09/02/2017



13/02/2017

Design of a low drag universal frame for subsea data acquisition in high energy tidal sites



15/02/2017



20/02/2017



20/02/2017



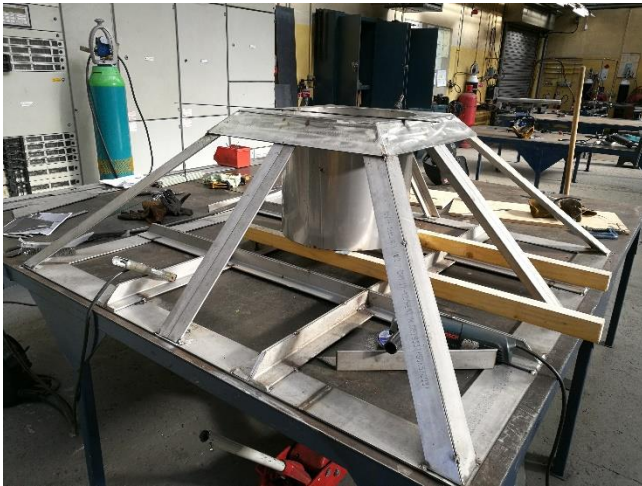
20/02/2017



20/02/2017



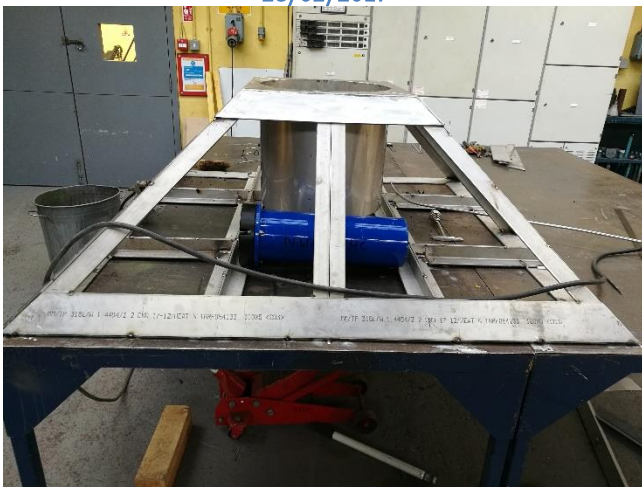
24/02/2017



28/02/2017



01/03/2017



01/03/2017



16/03/2017



16/03/2017



16/03/2017



16/03/2017



22/03/2017



22/03/2017



22/03/2017



22/03/2017



23/03/2017



23/03/2017



23/03/2017



23/03/2017



23/03/2017



23/03/2017



23/03/2017



23/03/2017



23/03/2017

First successful deployment of the Frame_#4 in the Pentland Firth environment

Once the manufacturing process has been completed, the Frame_#4 has been setup for the first deployment in Pentland Firth. The Pentland Firth is well known to be a very challenging environment as strong tidal currents are usually present. The Figure 60 shows the Frame_#4 completely assembled and equipped with the ADCP sensor installed into the sensor gimbal. The ADCP sensor used for such deployment is a RDI Teledyne V50. Inside the frame, behind the closing plates, two batteries have been suited, along with the required ballast. For this first deployment, a larger amount of ballast, approximately 200 kg, has been used to avoid any of losing both the frame and the sensor.



Figure 60 – Frame_#4 completely assembled and ready for the deployment

The final location of this first deployment has been set in the Pentland Firth area at 34m of depth. The Figure 61 shows some of the deployment phases.



Figure 61 – Some pictures of the Frame_#4 deployment in the Inner Sound

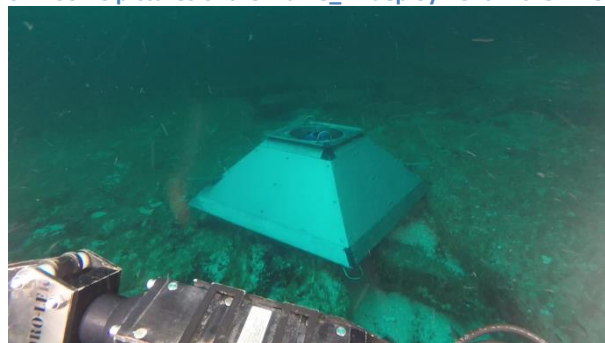


Figure 62 – View of the Frame_#4 at 34m depth from the ROV

After for weeks of deployment, the Frame_#4 has been successfully recovered using the ROV (see Figure 62). The ADCP sensor and the frame haven't reported any failure both at the components level and full prototype.

Once the ADCP sensor has been recovered, the data acquired during all the deployment have been analysed. The Figure 63 is a screenshot of the default analysis software of the RDI Teledyne V50 ADCP sensor. The top coloured map of Figure 63 shows the tide range measured during the deployment, while the bottom three graphs show the sensor heading, pitch and roll during the same period of time.

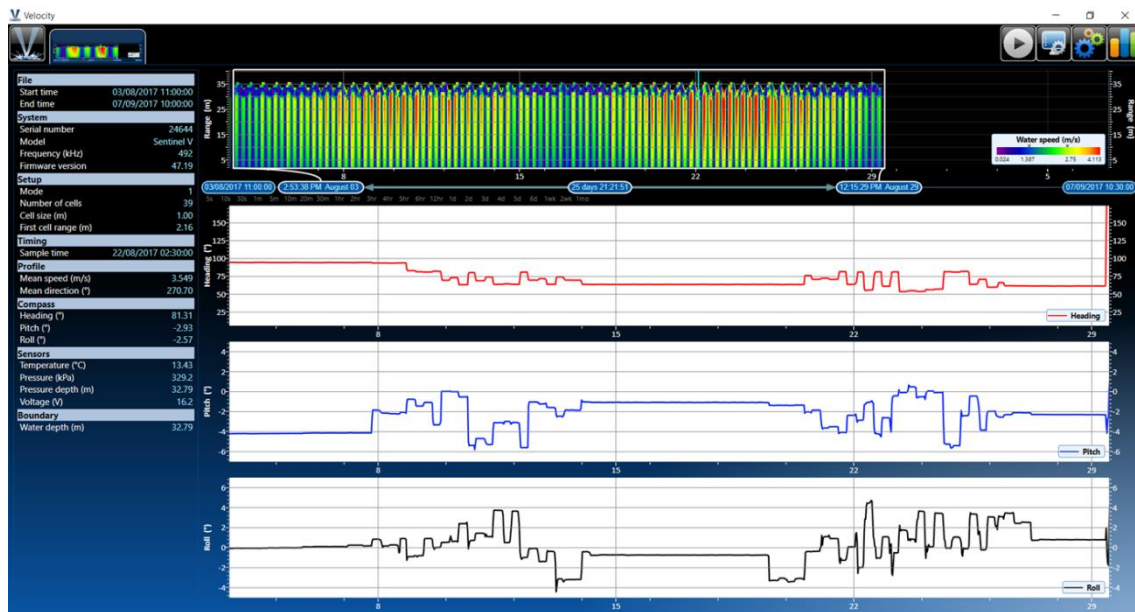


Figure 63 – Screenshot of the default analysis software of the RDI Teledyne V50 ADCP sensor

For a deeper analysis of the acquired data, they have been imported in Excel and post-processed. The Figure 64 shows a limited time history of the velocity magnitude from the late 16/08/2017 to the late 28/08/2017: such time history is highly representative of the tide events occurred in the Pentland Firth during the deployment. The highest velocity plotted in Figure 64 isn't the highest figure measured: a maximum value of 4.6 m/s has been measured as well.

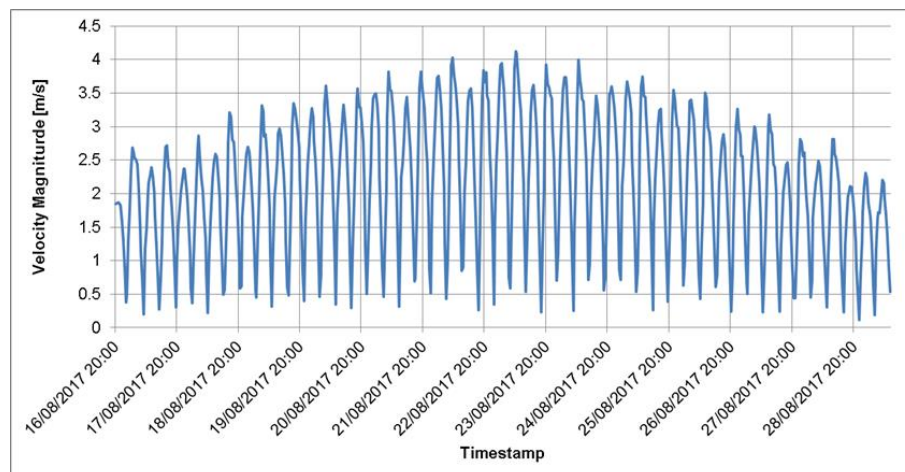


Figure 64 – Velocity magnitude measured from 16/08/2017 to 28/08/2017

In Figure 65 is represented how the velocity is distributed within the water column over the ADCP sensor head. Such velocity profiles are pretty similar to the one in Figure 40: comparing the two figures, some differences can be noticed near the free surface, where the effect of wave orbital motions affects the measurements.

The most interesting result from the deployment is depicted in Figure 66. This figure shows the time history of sensor pitch and roll angles: a small cut of the deployment time is presented here for highlighting the high frequency movements induced by turbulence on the sensor. Despite that, it can be observed how small are such fluctuations, meaning that the sensor is very weakly affected by the flow turbulence. In fact, due to the presence of the vortex generator around the top cap, the maximum overshoots of pitch and roll angles are within the $\pm 0.05^\circ$. This result, along with the ability of the Frame_#4 to remain in place during its

first deployment, is of particular interest, especially considering the highest velocity magnitude measured during the deployment.

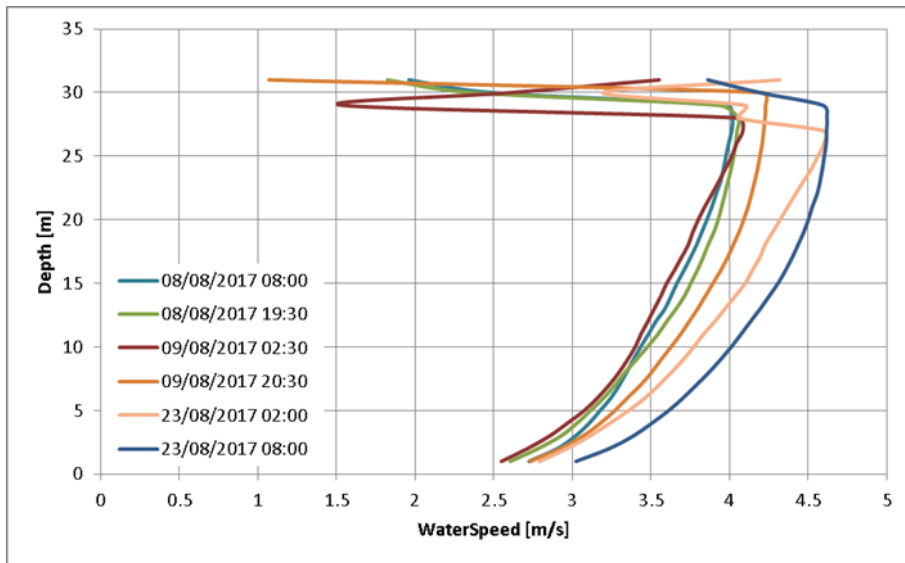


Figure 65 – Velocity profiles acquired with the RDI Teledyne V50 ADCP sensor

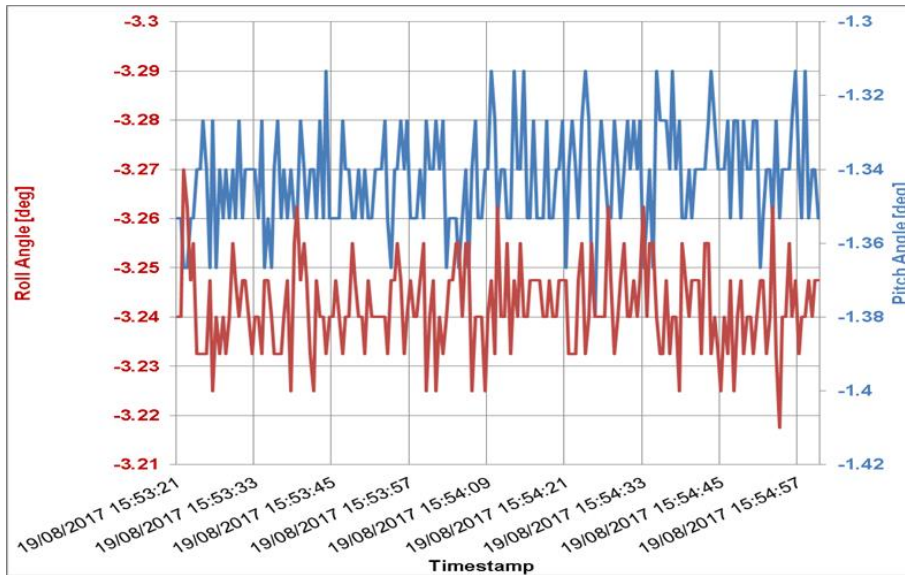


Figure 66 – RDI Teledyne V50 ADCP sensor pitch and roll angular motions

Final remarks

The work presented here shows of the design process of a more efficient seabed sensor frame, through the use of numerical CFD simulations. Starting from the existing sensor frames (Frame_#0, Frame_#1), a reverse engineering process has been followed to model such frames into a CAD software. Successively, their performance in extremely flow conditions have been evaluated using computational fluid dynamics. Interesting results have been obtained from the Frame_#1 that, at the bespoke flow velocities, is able to generate some downforce. Evaluated the amount of aerodynamic forces for both frame shapes, deployment effort required for each frame has been evaluated: due to such aerodynamic downforce, the Frame_#1 require less ballast than the Frame_#0, when the seabed friction coefficient is $\mu=0.740$; reducing the μ value, such trend is not confirmed. Indeed, such ballast evaluation is highly dependent on the seabed friction coefficient and figure requires the exact value of μ corresponding to the deployment area.

Identifying the beneficial effect of Frame_#1, a preliminary optimization process on Frame_#0 has been carried out. A frame equipped with some guide vanes and a simple vortex generator has been obtained; but, due to the manufacturability effort necessary to build and equip such frame, this has been not selected as the final optimized frame.

The results of this preliminary optimization have been used for designing a brand new frame. Initially, the effect of a different frame base shape has been evaluated, along with the possibility of having some clearance underneath: the rectangular base shape has been chosen and it has been noticed that, if the frame has a completely closed bottom, the aerodynamic efficiency of such frame is improved. The chosen rectangular shape has a different side angle, changed from 48° of the Frame_#0 to the 45° of the Frame_#2, as the latter assures the best possible downforce-to-drag ratio (aerodynamic efficiency value). It has been seen that, in the same flow and seabed friction condition, the Frame_#2 requires slightly less ballast than Frame_#1.

To further improve the aerodynamic performance of Frame_#2, the Frame_#3 has been designed, considering that a reduction of the frame frontal area reduces the frame drag and improves the frame efficiency. Moreover, due to the reduced frontal area, the frame height is reduced as well, with a beneficial effect on aerodynamic forces: indeed, the reduced frame height causes that the frame is at a lower flow velocity, being closer to the seabed. So, lowering the frame height places the frame into an area of the water boundary layer where there are lower velocity values. Moreover, the Frame_#3 has been equipped with a linear vortex generator, which has shown to improve frame holding capability when the flow speed increases. Hence, the Frame_#3 resulted to not need any ballast for deployment, even if the use of a proper safety margin is recommended.

Finally, the Frame_#4 has been investigated. Such frame has small modification as compared with Frame_#3. For CFD simulation on Frame_#4, the real frame configuration has been considered, along with the presence of a possible ADCP sensor. The aim of that analysis has been to evaluate the aerodynamic force on the frame and to compare the sensor movements with some data from a real deployment. In terms of forces, due to the clearance underneath the sensor frame, the Frame_#4 has shown a performance deterioration. The downforce reduction is mostly due to the flow possibility of going underneath and inside the frame, with a velocity value higher than the one expected during deployment: in fact, when the frame is on very rough seabed, the flow velocity underneath the sensor frame is without doubt reduced and, also, some of the frame bottom could resulted closed by the seabed roughness (i.e., rocks, peaks). In any case, the amount of ballast needed for deployment resulted reduced as compared with the Frame_#0 and Frame_#1. Using a velocity profile adapted to one measured in Westray firth, Orkney Island (Scotland, UK), the Frame_#4 has shown the capability of holding itself on the seabed without any ballast, as its height causes to work with a flow velocity value well below the one at which the previous frame specifications have been tested.

Finally, the Frame_#4 specific has been delivered for manufacturing purposes. When the Frame_#4 has been completely assembled and fitted with the RDI Teledyne V50 ADCP sensor, it has been deployed in the Pentland Firth area at 34m depth. The deployment has been 4 weeks long and the Frame_#4 has been successfully recovered without any particular issue. Data acquired from the sensor has been analysed and it has been noticed that the Frame_#4 has allowed to measure velocity magnitude up to 4.6 m/s, with very small

flow induced angular movements of the ADCP sensor. Thus, a high quality set measured data has been acquired using the Frame_#4 equipped with the vortex generator. A second deployment of the Frame_#4 prototype is planned and, possibly, in the vicinity of the Frame_#1, in order to compare data acquired using two different sensor frames in similar locations and further validate the Frame_#4 design. Moreover, a plan for retrofitting the Frame_#1 with a vortex generator is also under consideration.

References

- [1] CD-adapco™, User Guide STAR-CCM+® version 9.06, 2014.
- [2] G. H. Y. a. C. L. Jiyuan Tu, «Practical Guidelines for CFD Simulation and Analysis,» in *Computational Fluid Dynamics: A Practical Approach*, II, Elsevier Ltd., 2013, pp. 219-273.
- [3] E. J. Shaughnessy, I. M. Katz e J. P. Schaffer, «Bluff bodies,» in *Introduction to Fluid Mechanics*, Oxford University Press, 2005, pp. 915-926.
- [4] A. H. Techet, MIT - Massachusetts Institute of Technology , March 2014. [Online]. Available: web.mit.edu/13.42/VIV_2004.ppt.
- [5] A. Al-Jawadi, «Some Useful Numbers on the Engineering Properties of Materials (Geologic and Otherwise),» [Online]. Available: http://www.academia.edu/4156626/Some_Useful_Numbers_on_the_Engineering_Properties_of_Materials_Geologic_and_Otherwise_Angle_of_internal_friction.
- [6] V. Anchors, Anchor Manual 2015 - The guide to anchoring, Vryhof Anchors, 2015.
- [7] E. S. Gaffney, «Measurements of Dynamic Friction between Rock and Steel (DNA 4161 F),» Defence Nuclear Agency, Washington, DC, 1976.
- [8] M. G. Seibert, *Determining Anchoring Systems for Marine Renewable Energy Devices Moored in a Western Boundary Current*, Boca Raton, Florida: Florida Atlantic University, 2011.
- [9] R. J. Taylor, «Interaction of Anchors with Soil and Anchor design (N - 1627),» Naval Civil Engineering Laboratory, Port Hueneme, California, 1982.
- [10] R. Taylor e P. Valent, «Design Guide for Drag Embedment Anchors,» Naval Civil Engineering Laboratory, Port Hueneme, California, 1986.
- [11] LEAP Australia, «Selection of wall functions and Y+ to best capture the Turbulent Boundary Layer,» Leading Engineering Application Providers, [Online]. Available: <https://www.computationalfluidynamics.com.au/turbulence-part-3-selection-of-wall-functions-and-y-to-best-capture-the-turbulent-boundary-layer/>.
- [12] J. Holmes, E. English e C. Letchford, «Aerodynamic forces and moments on cubes and flat plates, with applications to wind-borne debris,» in *Fifth International Colloquium on Bluff-Body Aerodynamics and Applications*, Ottawa, Canada, 2004.
- [13] D. Ting, «Examples of Engineering Problems Involving Flow Turbulence,» in *Basics of Engineering Turbulence*, Elsevier Inc., 2016, pp. 187-202.
- [14] A. Priyanto, A. Maimun, S. Noverdo, J. Saeed, A. Faizal e M. Waqiyuddin, «A Study on Estimation of Propulsive Power for Wing in Ground Effect (WIG) Craft to Take-off,» *Jurnal Teknologi*, September 2012.
- [15] E. Cui e X. Zhang, «Ground Effect Aerodynamics,» in *Encyclopedia of Aerospace Engineering*, Richard Blocklei and Wei Shyy, 2010, pp. 245-256.
- [16] «Angle of Friction,» 14 12 2013. [Online]. Available: <http://www.geotechdata.info/parameter/angle-of-friction.html>.